Wireless Engineering and Technology, 2010, 1, 47-95
Published Online October 2010 in SciRes (http://www.SciRP.org/journal/wet/)

TABLE OF CONTENTS

Volume 1 Number 2 October 2010

Wireless Engineering and Technology (WET)

Journal Information

SUBSCRIPTIONS

The *Wireless Engineering and Technology* (Online at Scientific Research Publishing, www.SciRP.org) is published quarterly by Scientific Research Publishing, Inc., USA.

Subscription rates:

Print: $50 per issue.
To subscribe, please contact Journals Subscriptions Department, E-mail: sub@scirp.org

SERVICES

Advertisements
Advertisement Sales Department, E-mail: service@scirp.org

Reprints (minimum quantity 100 copies)
Reprints Co-ordinator, Scientific Research Publishing, Inc., USA.
E-mail: sub@scirp.org

COPYRIGHT

PRODUCTION INFORMATION

For manuscripts that have been accepted for publication, please contact:
E-mail: wet@scirp.org

Wireless Engineering and Technology, **2010, 1, 47-54**
doi:10.4236/wet.2010.12008 Published Online October 2010 (http://www.scirp.org/journal/wet)

Performance of Double-Pole Four-Throw Double-Gate RF CMOS Switch in 45-nm Technology

Viranjay M. Srivastava[1], K. S. Yadav[2], G. Singh[1]

[1]Electronics and Communication Engineering Department, Jaypee University of Information Technology, Solan, India; [2]VLSI Design Group, Central Electronics Engineering Research Institute (CEERI), Pilani, India.
Email: viranjay@ieee.org

Received September 7th, 2010; revised September 13th, 2010; accepted September 19th, 2010.

ABSTRACT

In this paper, we have investigated the design parameters of RF CMOS switch, which will be used for the wireless telecommunication systems. A double-pole four-throw double-gate radio-frequency complementary-metal-oxide-semiconductor (DP4T DG RF CMOS) switch for operating at the 1 GHz is implemented with 45-nm CMOS process technology. This proposed RF switch is capable to select the data streams from the two antennas for both the transmitting and receiving processes. For the development of this DP4T DG RF CMOS switch we have explored the basic concept of the proposed switch circuit elements required for the radio frequency systems such as drain current, threshold voltage, resonant frequency, return loss, transmission loss, VSWR, resistances, capacitances, and switching speed.

***Keywords*:** *45-nm Technology, Capacitance of Double-Gate MOSFET, DG MOSFET, DP4T Switch, Radio Frequency, RF Switch, Resistance of Double-Gate MOSFET, VLSI*

1. Introduction

In the radio transceiver the switches, traditional n-MOS switch has better performance compare to PIN diodes (use of PIN diodes consumes more power), but only for a single operating frequency [1,2]. For multiple operating frequencies, high signal distortions are easily observed, which results in an unrecognizable information signal at the receiver end which would be measured by using the curve of capacitance and voltage with VEE Pro software [3,4]. A continuous scaling of CMOS technology has a better performance of both frequency and noise, where it is becoming a rigorous part for RF applications in the GHz frequency regime of the spectrum. The aggressive scaling of metal-oxide-semiconductor field effect transistors (MOSFET) has led to the fabrication of high performance MOSFETs with a cut-off frequency (f_T) of more than 150 GHz [5]. As a result of this development, the CMOS is a strong candidate for the RF wireless communications in this frequency regime of the specrum.

For the Multiple-Input, Multiple Output systems, it is essential to design a new RF switch that is capable of operating with multiple antennas and frequencies as well as minimizing signal distortion and power consumption [6-8]. The excellent improvement in the frequency response of Si-CMOS devices has aggravated their use in the millimeter-wave regime such as high capacity wireless local area network, short range high data rate wireless personal area networks, and collision avoidance radar for automobiles. Using Si-CMOS for these applications allows for higher levels of integration and lower cost with improving the efficiency. Since for 65-nm technology has application of 60 GHz power amplifier designs [9,10], but recently few research group has demonstrated 60 GHz power amplifiers in 45-nm technologies.

For radio-frequency applications, generally, the common drive requirements for off-chip loads are of 50 Ω impedances. This impedance is a good compromise between lowest loss and highest power handling for a given cable size. Also this impedance caught on for RF transmission sooner than the well established 75 Ω that had been used for video transmission. The nodal capacitance, drain and source sidewall capacitances are the factors which controls the bandwidth of RF switches [11,12]. Since these switches are to be used with digital and baseband analog systems, control by on-chip digital and analog signals is another factor in the design [13].

In the design of DP4T DG RF CMOS switch structures with 45-nm technology for digital and analog, a transaction between speed and frequency response and

circuit complexity is always encountered. The properties for RF CMOS switch design for the application in communication and designed results are presented and have been designed to optimize for the particular application [14]. A DP4T DG RF CMOS switch has the properties as fixed tuned matching networks, low quality factor matching networks, high power output, mounting flange packages, and silicon grease. Some bipolar RF CMOS transistors are suitable for automotive, commercial or general industrial applications.

In this paper, we present a comprehensive study of the RF switch performance of 45-nm low-power, high-speed double-pole four-throw double-gate radio-frequency complementary-metal-oxide-semiconductor (DP4T DG RF CMOS) switch. The DP4T DG RF CMOS switch structures with different aspect ratios for 45-nm technology and their layouts are studied to understand the effect of device geometry on working of switching properties. In this design transistor width increases for double-gate MOSFET such that peak power-added efficiency (PAE) and output power P_{out} decrease as these parameters decreases with increasing device width because of a reduction in f_{max} [15]. In a RF power amplifier, PAE is defined as the ratio of the difference of the output and input signal power to the DC power consumed. The RF power performance of 45-nm devices is shown to be very comparable to that of 65-nm devices.

An application for a CMOS switch covers the areas of micro power circuits and other wireless applications at frequencies from as low as 0.1 GHz for low earth orbiting satellite system to thousand of GHz [16]. Various circuit parameters have been discussed in this paper for better performance.

Each of the parameters will be discussed separately for the purpose of clarity of presentation and understanding the operation of DP4T DG RF CMOS switch structures for 45-nm technology. The organization of the paper is as follows; DP4T DG RF CMOS switch model is presented in Section 2, Characteristics of DP4T DG RF CMOS switch for layout are discussed in Section 3. The capacitances, Inductances and other parameters present in DG MOSFET for high speed RF switches are discussed in Section 4. The effective resistance of DP4T DG RF CMOS present in switch is discussed in Section 5. Finally, conclusion of the work is in Section 6.

2. DP4T DG RF CMOS Switch Model

The selections of RF CMOS switch require an analysis of performance specifications. Since drain-source breakdown voltage is the maximum drain-source voltage before breakdown with the gate grounded [17], also specifications for RF CMOS transistors includes the maximum drain saturation, common-source forward transconductance, operating frequency, and output power. Devices that operate in depletion mode can increase or decrease their channels by an appropriate gate voltage. By distinction, devices that operate in enhancement mode can only increase their channels by an appropriate gate voltage. RF MOSFET transistors vary in terms of operating mode, packaging, and packing methods.

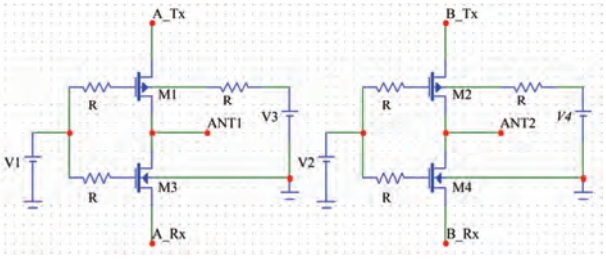

Figure 1. DP4T RF CMOS switch with inverter property [14].

This paper proposes a design of DP4T DG RF CMOS switch structures at 45-nm technology for low power consumption and low distortion application of RF switch in communication that operates at 0.1 GHz to 60 GHz. The n-channel devices were used in the HF portion of the circuits with p-channel devices used as current sources. The switches which were designed to drive 50 Ω resistive loads and utilized multiple gate fingers to reduce parasitic capacitance in an effort to improve the operating frequency [13].

The objective of proposed design of a switch is to operate at 0.1 GHz to few GHz frequency range for MIMO systems. This switch must mitigate attenuation of passing signals and exhibit high isolation to avoid corruption of simultaneously received signals [14]. According to the previous work, DP4T switch is a fundamental switch for MIMO applications because parallel data streams can be transmitted or received simultaneously using the multiple antennas. For instance, the transmitted signal from Power Amplifier (PA) is sent transmitter 'A' which is shown in **Figure 1** with named as 'A_Tx' port and travel to the ANT1 node while the received signal will travel from the ANT2 node to the receiver 'B' with a named as 'B_Rx' port and pass onto the Low Noise Amplifier or any other application.

The proposed switch contains CMOS in its architecture and needs only two control lines (V_1, V_2) of 1.2 V to control the signal traffic between two antennas and four ports as shown in **Figure 1**, Hence, improving port isolation performance two times, compared to the DPDT switch and reducing signal distortion. In addition, signal fading effects can be reduced because sending identical signals through multiple antennas will most likely result in a high quality combined signal at the receiver end. For the design of DP4T DG RF CMOS switch, we design a

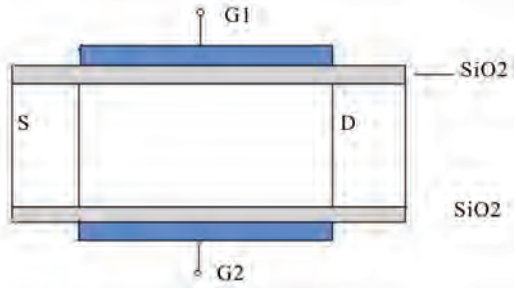

Figure 2. Basic double-gate n-MOSFET.

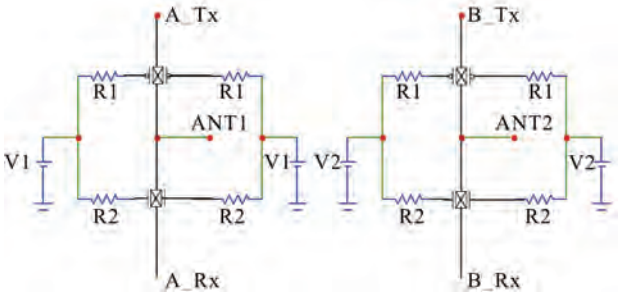

Figure 3. Proposed DP4T DG RF CMOS switch.

double-gate as shown in **Figure 2**. This shows the double-gate n-MOSFET. Similarly, we can design double-gate p-MOSFET. Now, we convert the **Figure 1**, DP4T switch using the basic double-gate transistor as shown in **Figure 2**, for DP4T DG RF CMOS switch as shown in **Figure 3**.

Since in the **Figure 1**, four transistors are used for two antennas. In this antenna using the CMOS functionality, at a time any one of transistor M1 or M3 will operate and in the same fashion any one of transistor M2 or M4 will operate. Same function is measured in the proposed DP4T DG RF CMOS switch as in **Figure 3**. This circuit is designed with a Micro-Cap Evaluation 6.0 tool. We can find easily that CMOS based RF switches allow longer battery life than PIN diodes, because current consumption is significantly reduced and also about 60 percent smaller than the smallest GaAs RF switch on the market. Furthermore, our switch also experiences minimal distortion, negligible voltage fluctuation, and low power supply of only 1.2 V. In this switch with compare to **Figure 1**, for A_Tx and B_Tx, two p-MOS are designed for parallel combination and for A_Rx and B_Rx, two n-MOS are designed for parallel combination which is better selection.

3. Characteristics of DP4T DG RF CMOS Switch for Layout

Figure 4 shows the layout of DP4T DG RF CMOS switch with two input voltages (Vin_1 and Vin_2) and output through antennas (ANT_1 and ANT_2) with two transmitters (Tx_A and Tx_B) and two receivers (Rx_A and Rx_B). This layout is drawn with Microwind 3.0 version tool. Here color code has their usual meanings [18,19]. **Figure 5** shows the antenna voltages ANT_1 and ANT_2 with input voltages Vin_1 and Vin_2 for this transceiver switch. Drain current for this transceiver switch with output voltage is shown in **Figure 6**, which gives the grain current $I_{dd\ (max)}$ 0.387 mA, $I_{dd\ (avg)}$ 0.02 mA, also raise time 36 ps at 1 GHz operating frequency.

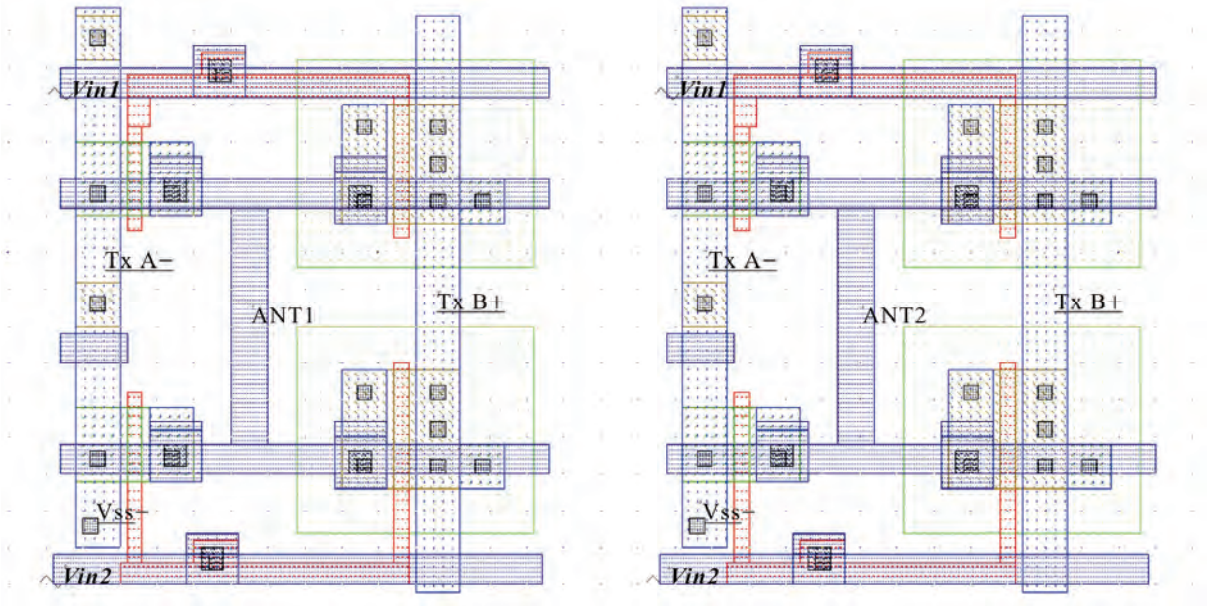

Figure 4. DP4T DG RF CMOS switch layout with antennas.

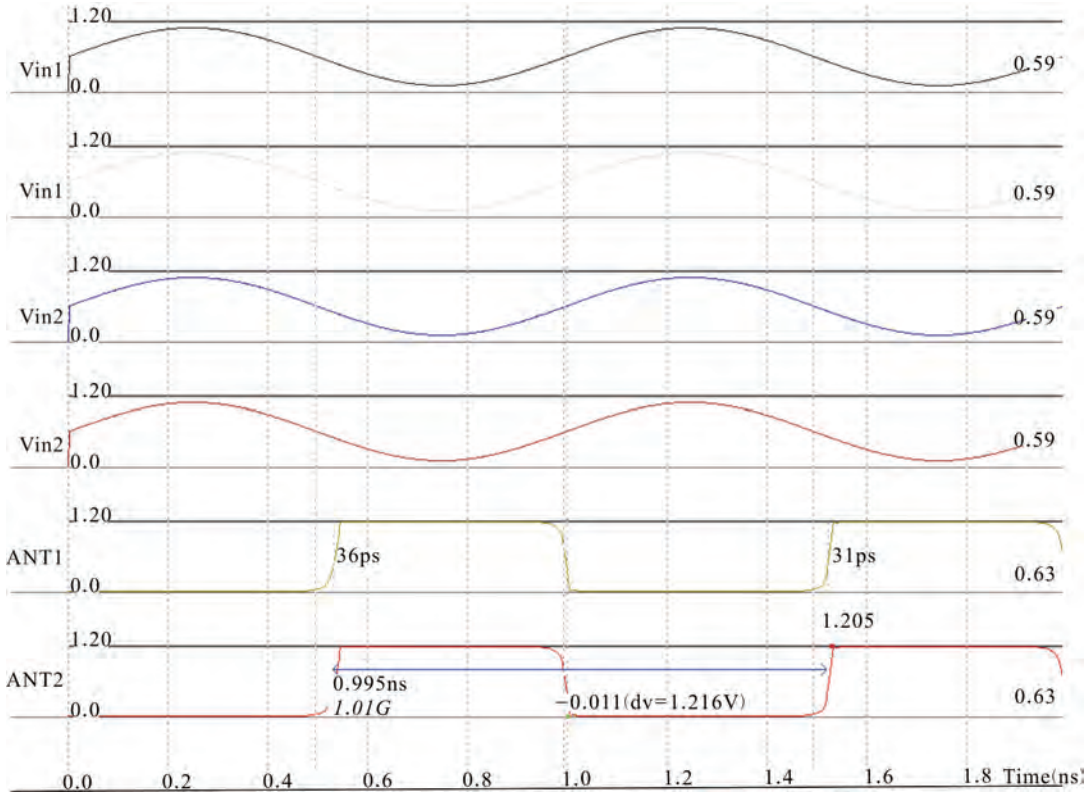

Figure 5. Antenna voltage with input voltages for DP4T DG RF CMOS transceiver switch.

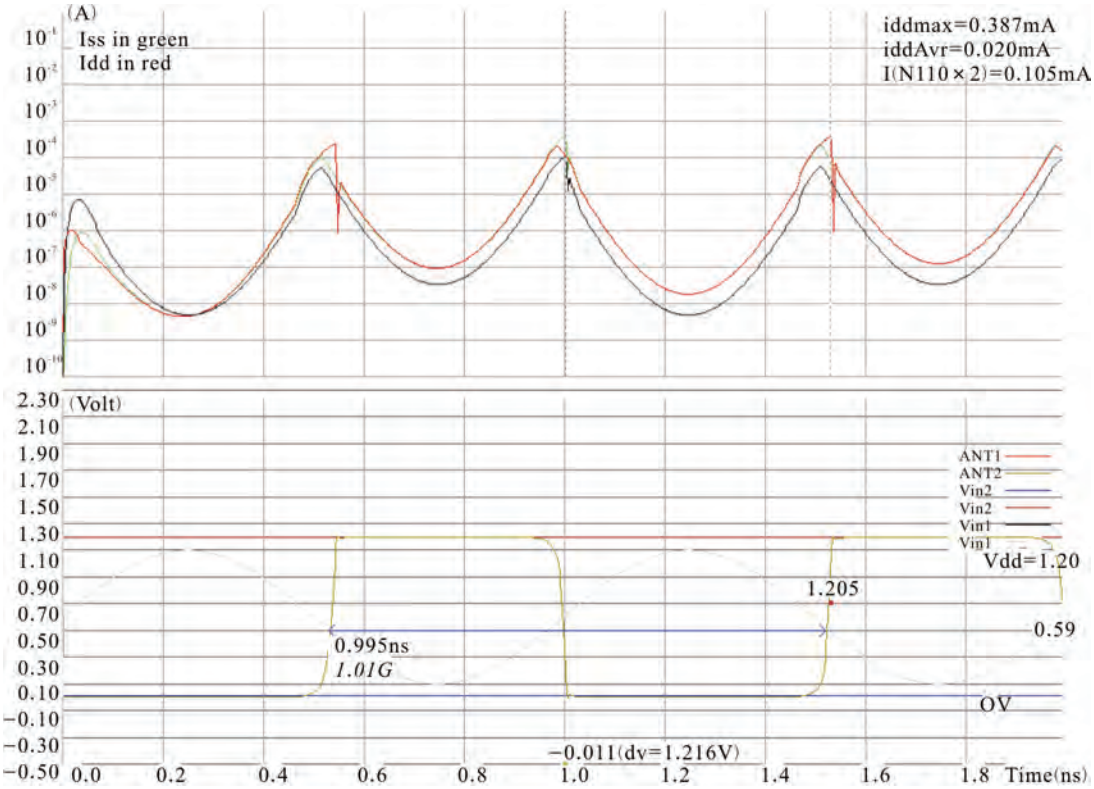

Figure 6. Drain current for DP4T DG RF CMOS transceiver switch with output voltage.

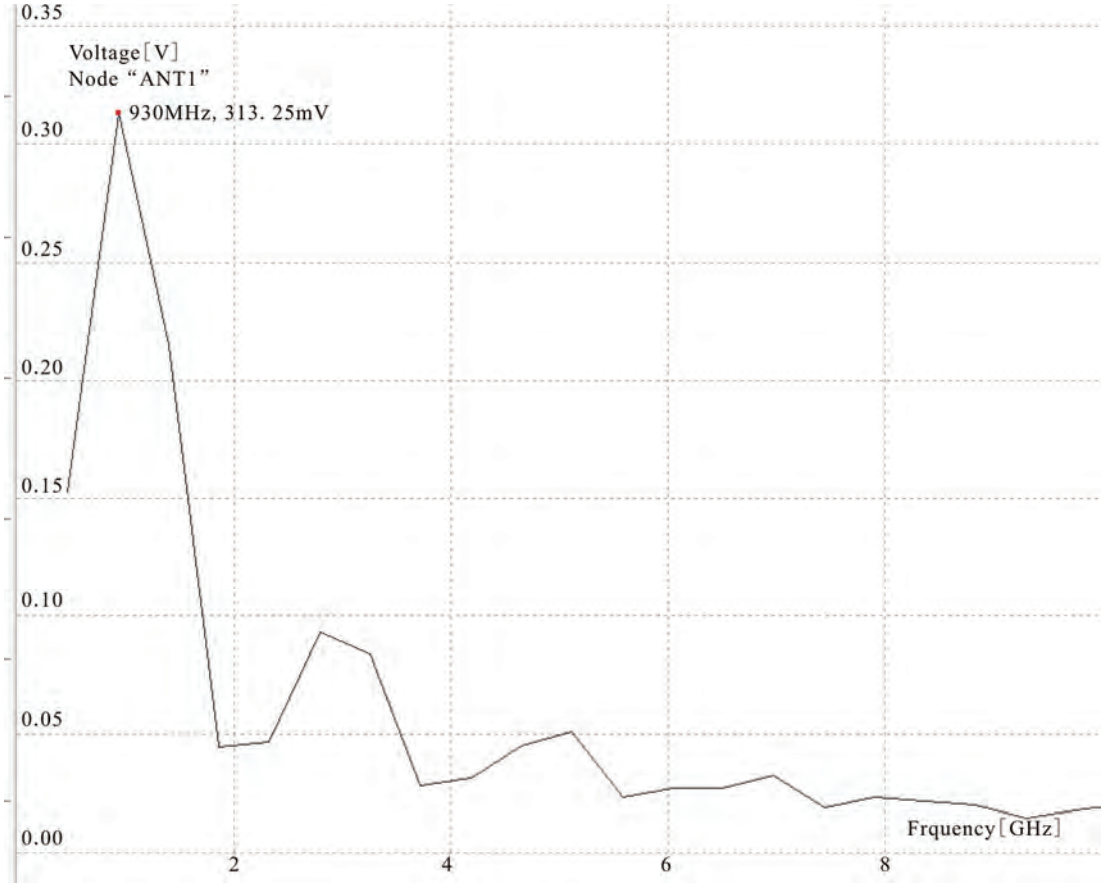

Figure 7. Antenna (ANT1) output with different frequencies for DP4T DG RF CMOS transceiver switch.

In terms of antenna, we draw the first antenna (ANT_1) voltage at different frequencies from 0.1 GHz to 8 GHz, in which highest voltage on antenna is achieved at 1 GHz frequency and that is decreases with the increasing frequencies as shown in **Figure 7**. Also this result is same for second antenna (ANT_2).

4. Measurement of Parameters for Double-Gate MOSFET

With the use of Microwind 3.0 version tool for double-gate MOSFET length of 0.045 μm (45 nm) and width of 22.5 μm, we calculate the capacitance of 5.72 fF, inductance of 30 pH, and resistance of 3.12 kΩ. After that we design a DP4T DG RF CMOS switch with help of these values of capacitance, inductance and resistance. A small-signal performance from few MHz to 100 GHz was measured using RF-99 tool freely available software. Equivalent switch circuit with respect to the capacitance is shown in **Figure 8** and the results are shown in **Figure 9** and in **Table 1**.

In detail **Figure 9** represents the frequency band, noise power, delay, phase shift, return loss at Tx port, return loss at antenna port, insertion loss measured between Tx port and antenna port, VSWR, transmission loss, reflec tion coefficient. Additional losses associated with cables and connectors, which are quite high at 60 GHz, must be taken into account in the system implementation.

5. Effective Resistance of DP4T RF CMOS Due to Double-Gate

Models of a MOS transistor biased in deep triode region, corresponding to the ON state of the switch, and cut-off region, corresponding to the OFF state of the switch, are shown in **Figure 10(a)** and **Figure 10(b)** respectively. The insertion loss of a MOS transistor switch under the ON state is dominated by its ON-resistance (R_{on}) and substrate resistance (R_b) [20-22]. Isolation of the switch under the OFF state is finite due to signal coupling

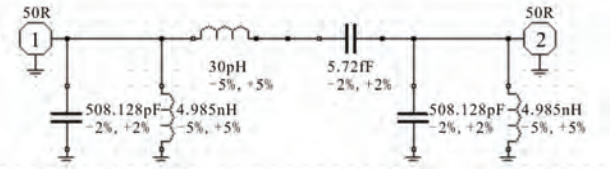

Figure 8. Equivalent switch circuit of capacitance.

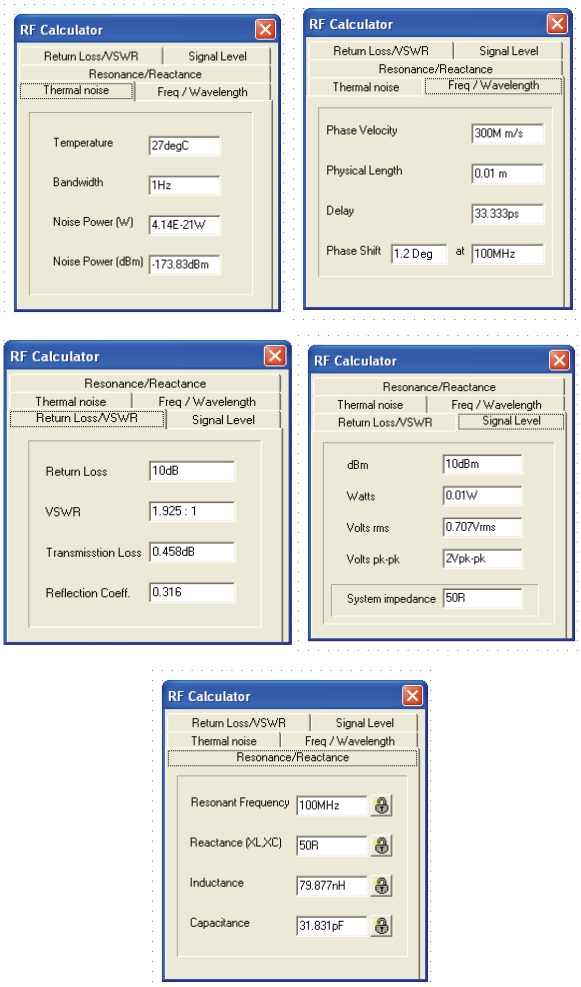

Figure 9. Measurements of parameters for DP4T DG RF CMOS switch.

Table 1. Summary of the performance of the double-gate MOSFET T/R switch.

Parameter	Value and Range
Frequency band	0.1 GHz to 1 GHz
Temperature	27 degree C
Noise power	$4.4*10^{-21}$ W,
Phase velocity	300 M m/s
Delay	33.33 ps
Phase shift	1.2 degree at 0.1 GHz
Return Loss	10 dB
Transmission loss	0.46 dB
VSWR	1.93:1
Reflection coefficient	0.316
RMS volts	0.707 V
Control voltages	1.2 V/0 V
I_{dd} max	0.387 mA
I_{dd} avg	0.020 mA
System impedance	50 ohm
Capacitance	31.83 pF
Inductance	79.88 nH
Reluctance	50 mho
t_{rise}	36 ps
t_{fall}	31 ps

through the parasitic capacitances, C_{ds}, C_{gs}, and C_{gd}, and through the junction capacitances, C_{sb} and C_{db}.

Since the interface contact resistance is inversely proportional to the total gate area as in term of length and width of a gate. The reduction of resistance should lead to improved RF properties in MOSFETs [5,23-28]. In **Figure 10** these diodes are represented by their junction capacitances, C_{sb} and C_{db}. The ON-resistance is given by;

$$R_{on} = \frac{1}{\mu C_{ox} \frac{W}{L}(V_{gs} - V_{th})} \quad (1)$$

for proper working of a switch and to reduce the insertion loss, we have to reduce this ON-resistance. So to keep this R_{on} small, we have to following steps;

5.1. Making Parallel Combination of R

In double-gate switch there are two resistors between drain to source due to gate1 and gate2. Both of these resistors are in parallel so making the R_{on} half, which keeps R_{on} small compare to single gate MOS.

5.2. Choosing Transistor with Large μ

This criterion of reducing R_{on} can be achieved by using n-MOSFET transistors in place of p-MOSFET transistors in the design [22].

5.3. Increasing Aspect Ratio

To increase the ratio of W/L, we have to widening a transistor width (W) and using transistors of minimum allowable channel length (L). Since the minimum value of length is limited by the technology which is 45 nm in this paper that is for transistor length of 0.045 μm and width of 22.5 μm. However, when we increase the width of a transistor, its junction capacitances and parasitic capacitances increases with same ratio. For single gate MOSFET, at ON condition of a transistor, increasing C_{sb} and C_{db} tends to more signal being coupled with the substrate and dissipated in the substrate resistance R_b. At OFF condition of the transistor, increasing C_{ds}, C_{gd}, and C_{gs} tends to lower isolation between the sources and drain due to capacitive coupling between these terminals

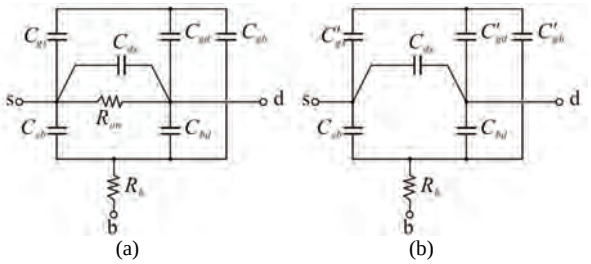

Figure 10. Models of a single gate n-MOS transistor operating as a switch in (a) ON state and (b) OFF state [22].

[22]. Whereas for double-gate MOSFET when both the transistors are ON, increasing C_{sb} and C_{db} leads to less signal being coupled to the substrate as substrate is not present in this structure, so no dissipation in the substrate resistance R_b. When the transistor is OFF, increasing C_{ds}, C_{gd}, and C_{gs} leads to higher isolation between the source and drain due to no capacitive coupling between these terminals.

For low frequency, sufficient isolation can be achieved, so it is not an optimizing parameter for frequencies of order 1 GHz designs. Thus, in these designs, only insertion loss needs to be minimized. No trade-off between insertion loss and isolation is required. On the other hand, at higher frequencies as 60 GHz, isolation is smaller due to several low impedance paths caused by parasitic capacitances. This necessitates a trade-off between insertion loss and isolation during sizing the transistors.

In this designed transistor, width increases for double-gate MOSFET, so peak power-added efficiency and output power decrease as these parameters decreases with increasing device width because of a reduction in f_{max} [15].

5.4. Keeping $V_{gs} - V_{th}$ Large

This criterion can be achieved by increasing the V_{gs} and decreasing the V_{th}, so that the difference of these can be large. Threshold voltage has following equation;

$$V_{th} = V_{th_0} + \gamma.(\sqrt{|2\varphi_f + V_{sb}|} - \sqrt{|2\varphi_f|}) \quad (2)$$

where γ is the body effect coefficient and φ_f is the Fermi level in the substrate. Since in double-gate MOSFET no bulk or substrate is available so γ equals to zero and this decreases the V_{th} which participate into increasing of the $V_{gs} - V_{th}$. This leads to higher R_{on} according to (1). In conclusion, by increasing the source-drain voltage, we sacrifice insertion loss for power handling capability.

After designing of DP4T DG RF CMOS switch with designed double-gate MOSFET for 45-nm technology, we draw the layout and measured the parameters available in this switch. It includes the basics of the circuit elements parameter required for the radio frequency sub-systems of the integrated circuits such as drain current, threshold voltage, resonant frequency, return loss, transmission loss, VSWR, resistances, capacitances, and switching speed.

6. Conclusions

For the purpose of RF switch, we achieve the process to minimize control voltage and minimization of the resistance, for the switch ON condition with DP4T DG RF CMOS switch. Since the operating frequencies of the RF switches are in the order of GHz, therefore, it is useful for data link transmitter, radio transceiver switch, wireless local area network and other IEEE 802.11 industrial applications including Wi-Fi system.

REFERENCES

[1] Skyworks Solutions Inc., "Application Note, APN1002, Design with PIN Diodes," Woburn, July 2005.

[2] J. Park and Z. Q. Ma, "A 15 GHz CMOS RF Switch Employing Large Signal Impedance Matching," *Proceeding of Topical Meeting on Silicon Monolithic Integrated Circuits in RF Systems*, San Diego, 2006, pp. 1-4.

[3] V. M. Srivastava, K. S. Yadav and G. Singh, "Application of VEE Pro Software for Measurement of MOS Device Parameter Using C-V Curve," *International Journal of Computer Applications*, Vol. 1, No. 7, March 2010, pp. 43-46.

[4] V. M. Srivastava, "Capacitance-Voltage Measurement for Characterization of a Metal Gate MOS Process," *International Journal of Recent Trends in Engineering*, Vol. 1, No. 4, May 2009, pp. 4-7.

[5] L. E. Microelectron and A. B. Stockholm, "Overlooked Interfacial Silicide-Polysilicon Gate Resistance in MOS Transistors," *IEEE Transactions on Electron Devices*, Vol. 48, No. 9, September 2001, pp. 2179-2181.

[6] J. P. Carmo, P. M. Mendes, C. Couto and J. H. Correia "A 2.4-GHz RF CMOS Transceiver for Wireless Sensor Applications," *Proceeding of International Conference on Electrical Engineering*, Coimbra, 2005, pp. 902-905.

[7] P. Mekanand and D. Eungdamorang, "DP4T CMOS Switch in a Transceiver of MIMO System," *Proceeding of* 11*th IEEE International Conference of Advanced Communication Technology*, Korea, 2009, pp. 472-474.

[8] P. H. Woerlee, *et al*, "RF CMOS performance trends," *IEEE Transaction on Electron Devices*, Vol. 48, No. 8, August 2001, pp. 1776-1782.

[9] W. L. Chan *et al*, "A 60 GHz-Band 1 V, 11.5 dBm Power Amplifier with 11% PAE in 65-nm CMOS," *International Solid State Circuits Conference*, San Francisco, 2009, pp. 380-381.

[10] A. Valdes-Garcia, *et al*, "60 GHz Transmitter Circuits in 65-nm CMOS," *Radio Frequency Integrated Circuits Symposium*, 2008, Atlanta, pp. 641-644.

[11] Y. Cheng and M. Matloubian, "Frequency Dependent Resistive and Capacitive Components in RF MOSFETs," *IEEE Electron Device Letters*, Vol. 22, No. 7, July 2001, pp. 333-335.

[12] T. H. Lee, "The Design of CMOS Radio-Frequency Integrated Circuits," 2nd Edition, Cambrige Univrsity Press, New York, 2004.

[13] R. H. Caverly, S. Smith and J. G. Hu, "RF CMOS Cells for Wireless Applications," *Journal of Analog Integrated Circuits and Signal Processing*, Vol. 25, No. 1, 2001, pp. 5-15.

[14] V. M. Srivastava, K. S. Yadav and G. Singh, "Double Pole Four Throw Switch Design with CMOS Inverter," *Proceeding of* 5*th IEEE International Conference on*

Wireless Communication and Sensor Network, 15-19 December 2009, pp. 1-4.

[15] U. Gogineni, J. Alamo and C. Putnam, "RF Power Potential of 45 nm CMOS Technology," *Proceeding of Topical Meeting on Silicon Monolithic Integrated Circuits in RF Systems*, New Orleans, 2010, pp. 204-207.

[16] T. Manku, "Microwave CMOS Device Physics and Design," *IEEE Journal of Solid State Circuits*, Vol. 34, No. 3, March 1999, pp. 277-285.

[17] S. H. Lee, C. S. Kim and H. K. Yu, "A Small Signal RF Model and its Parameter Extraction for Substrate Effects in RF MOSFETs," *IEEE Transaction on Electron Devices*, Vol. 48, No. 7, July 2001, pp. 1374-1379.

[18] S. Kang and Y. Leblebici, "CMOS Digital Integrated Circuits Analysis and Design," 3rd Edition, 2002, McGraw-Hill, New York, NY, USA.

[19] R. Baker, H. Li and D. Boyce, "CMOS Circuit Design, Layout, and Simulation" 3rd Edition, *IEEE Press Series on Microelectronic Systems*, 2010.

[20] U. Gogineni, *et al*, "Effect of Substrate Contact Shape and Placement on RF Characteristics of 45-nm Low-Power CMOS Devices," *IEEE Radio Frequency Integrated Circuits Symposium*, Massachusetts, 2009, pp. 163-166.

[21] F. J. Huang, "A 0.5-μm CMOS T/R Switch For 900 MHz Wireless Applications," *IEEE Journal of Solid-State Circuits*, Vol. 36, No. 3, 2001, pp. 486-492.

[22] C. Ta, E. Skafidas and R. Evans, "A 60-GHz CMOS Transmit/Receive Switch," *IEEE Radio Frequency Integrated Circuits Symposium*, Hawaii, 2007, pp. 725-728.

[23] V. M. Srivastava, K. S. Yadav and G. Singh, "Measurement of Oxide Thickness for MOS Devices, Using Simulation of SUPREM Simulator," *International Journal of Computer Applications*, Vol. 1, No. 6, March 2010, pp. 66-70.

[24] Y. Cheng and M. Matloubian, "Parameter Extraction of Accurate and Scalable Substrate Resistance Components in RF MOSFETs," *IEEE Electron Device Letters*, Vol. 23, No. 4, April 2002, pp. 221-223.

[25] V. M. Srivastava, "Relevance of VEE Programming for Measurement of MOS Device Parameters," *Proceedings of IEEE International Advance Computing Conference*, Patiala, March 2009, pp. 205-209.

[26] S. M. Sze, "Semiconductor Devices: Physics and Technology," 2nd Edition, Tata McGraw Hill, New Delhi, 2004.

[27] V. M. Srivastava, K. S. Yadav and G. Singh, "Designing Parameters for RF CMOS Cells," *International Journal of Circuits and Systems*, Vol. 1, No. 2, October 2010.

[28] V. M. Srivastava, K. S. Yadav and G. Singh, "Analysis of Attenuation, Isolation and Switching Speed of DP4T Double Gate RF CMOS Switch Design," *Proceeding of IEEE International Conference on Industrial Electronics, Control & Robotics*, NIT Rourkela, India, 27-29 December 2010.

Wireless Engineering and Technology, **2010, 1, 55-63**
doi:10.4236/wet.2010.12009 Published Online October 2010 (http://www.scirp.org/journal/wet)

Scientific Research

Resonant Length Formulations for Dual Band Slot Cut Equilateral Triangular Microstrip Antennas

Amit A. Deshmukh[1], K. P. Ray[2]

[1]DJSCOE, Vile – Parle (W), Mumbai, India; [2]SAMEER, Mumbai, India.
Email: amitdeshmukh76@yahoo.com, kpray@rediffmail.com

Received August 2nd, 2010; revised September 22nd, 2010; accepted September 28th, 2010.

ABSTRACT

The dual band equilateral triangular microstrip antennas are realized by cutting the slots of either quarter wave or half wave in length, inside the patch. In this design, however these simpler approximations of slot length against the frequency do not give closer results for different slot lengths and there positions inside the patch. In this paper, the modal variations of slot cut patch antennas over wide frequency range are studied. It is observed that the slot does not introduce any mode but reduces the higher order mode resonance frequency of the patch and along with the fundamental mode realizes dual band response. The formulations of the resonant length for the mode introduce by the slots in these antennas are proposed. The resonance frequencies calculated using proposed formulations agree well with the simulated results with an error of less than 5%.

Keywords*: *Equilateral Triangular Microstrip Antenna, Dual Band Microstrip Antenna, U-Slot, Pair of Rectangular Slots

1. Introduction

The dual band microstrip antenna (MSA) is realized by cutting a slot at an appropriate position inside the patch [1-3]. Since the slots are cut inside the patch, they neither increase the patch size nor largely affect the radiation pattern of the patch. These slots can take different shapes like, rectangular or square slot, step slot, tooth-brush shaped slot, V-slot, U-slot, etc [4-8]. The slot adds another resonant mode near the fundamental mode of the patch and realizes dual frequency response. The dual band equilateral triangular MSA (ETMSA) have also been realized by cutting the pair of rectangular or U-slot inside the patch [4-9]. While designing these slotted MSAs for the required frequency, depending upon where they are cut in the patch, the slot length is taken equal to nearly half wave or quarter wave in length. Towards the shorted end of the slot, the surface currents encircles over a finite length, which stores magnetic energy towards the shorted slot end [10]. To account for this an additional length is added to this half or quarter wavelength. This additional length is reported to be 10% of the slot length at the required frequency [10]. However it was observed that these simpler approximations of slot length against the frequency do not give closer results for varying slot lengths and their positions inside the patch. Therefore an in-depth analysis for the slot cut MSA is required over a wide frequency range so as to accurately model the slot length at the required frequency.

In this paper, the slot frequencies for U-slot or rectangular slots cut dual band ETMSAs, calculated by using their half wave or quarter wave length approximations are compared with the simulated values obtained using IE3D software [11]. It was observed that the above approximations give larger error for wide range of slot lengths and their positions inside the patch. Therefore a detail modal analysis for these slots cut ETMSAs was carried out over a wide frequency range using the surface current distributions obtained using IE3D software. It was observed that the U and rectangular slots alters the resonance frequency of higher order TM_{11} mode of ETMSA and along with its fundamental TM_{10} mode realizes dual band response. The radiation pattern at the TM_{10} mode for ETMSA is in the broadside direction whereas at TM_{11} mode it is in the conical direction. Since the slot affects the current distribution on the patch at TM_{11} mode, with the increasing slot length the radiation pattern at the modified TM_{11} frequency becomes in the broadside direction. The cross-polarization levels decreases with the increase in slot length. The surface current distributions for slot cut ETMSAs were studied for different slot lengths and the resonant length formulation

for the slot (modified higher order) mode and patch mode is proposed. The resonant frequencies calculated using the proposed formulations agrees well with the simulated results with an error of less than 5% over the entire slot length range. The formulations are first proposed on glass epoxy substrate (ε_r = 4.3, h = 0.16 cm, and tan δ = 0.02) and further they are validated on RT-Duroid substrate (ε_r = 2.33, h = 0.16 cm, and tan δ = 0.001).

2. Dual Band Slot Cut ETMSAs

In most of the reported slotted antennas the slot length is taken to be equal to half or quarter wave in length. In dual band pair of rectangular slots cut ETMSA as shown lengths (l) from 0.5 to 4.0 cm, the equivalent slot resonant length is calculated by adding the correction length as given in Equation (1). The slot frequency is calculated by using Equation (2). Since the surface currents circulate around the slot, the effective dielectric constant (ε_{re}) is calculated by using the average of the widths on the two sides of the slot [1]. For different values of Y, the frequencies calculated using Equations (1) and (2) are plotted against the simulated frequencies obtained using IE3D in **Figure 1(b-d)**. The % error (E) with respect to the simulated value is calculated by using Equation (3) and it is also plotted in the same figure.

$$l_e = l + \frac{0.4l}{\sqrt{\varepsilon_{re}}} \tag{1}$$

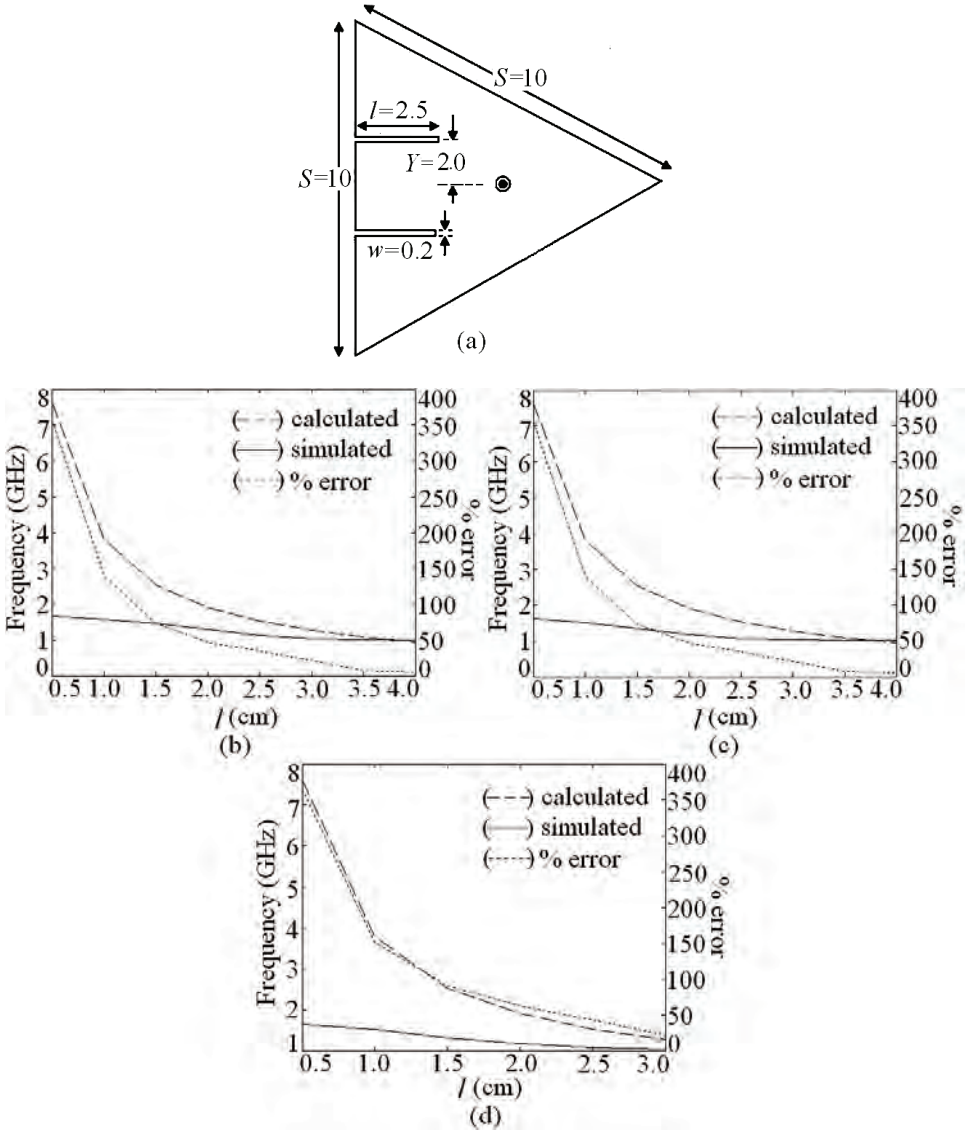

Figure 1. (a) ETMSA with pair of slots and its resonance frequency and % error plots for (b) *Y* = 1; (c) *Y* = 2 and (d) *Y* = 3.

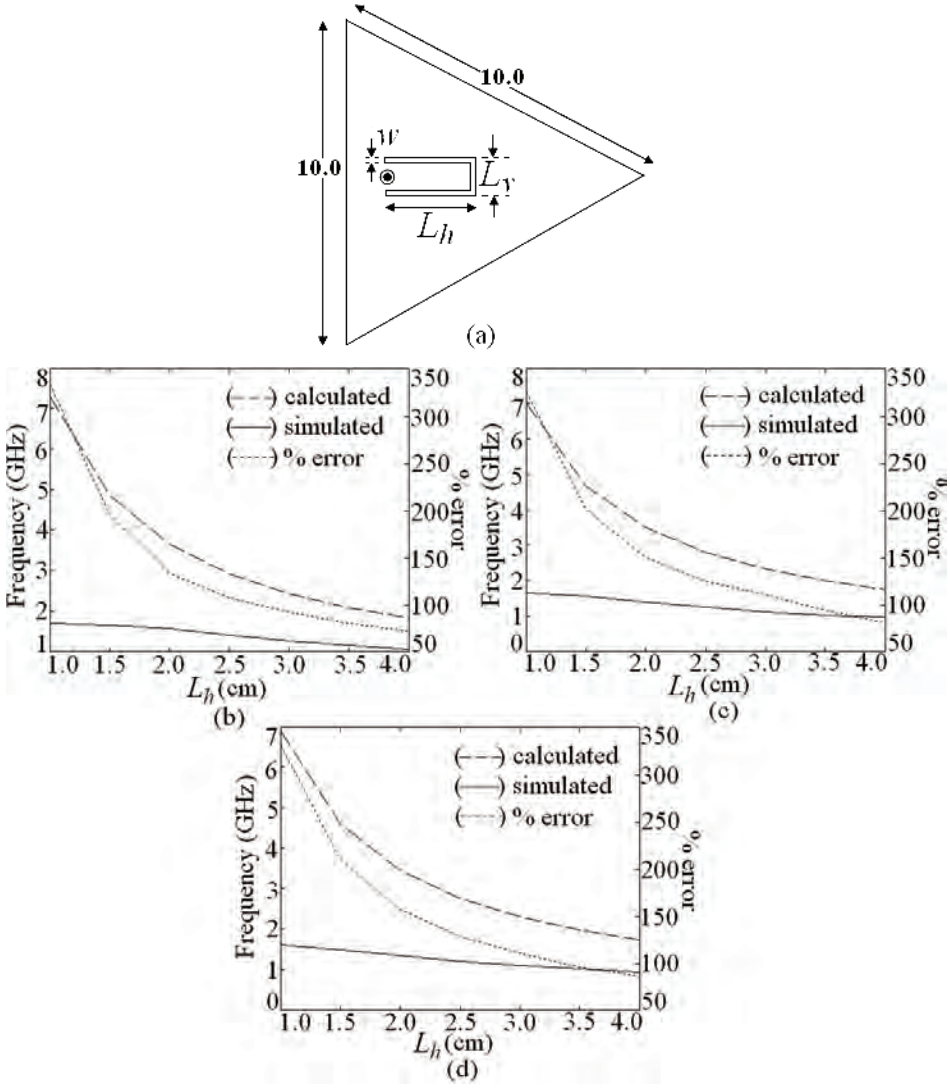

Figure 2. (a) U-slot cut ETMSA and its resonance frequency and % error plots for (b) L_v = 1; (c) L_v = 2 and (d) L_v = 3.

$$f_r = \frac{c}{4l_e\sqrt{\varepsilon_{re}}} \tag{2}$$

$$E = \frac{f_{ie3d} - f_r}{f_{ie3d}} \times 100 \tag{3}$$

Using this approach for some values of Y and only for larger l, a smaller E is obtained. The dual band U-slot cut ETMSA is shown in **Figure 2(a)**. The inner U-slot length equals half the wave length. The ε_{re} is calculated by using the inner U-slot width (L_v – 2w). The resonant length and frequency is calculated by using Equations (4) to (6). For different values of L_v and L_h, the slot frequency calculated by using the following equations and that obtained using IE3D are shown in **Figures 2(b-d)**. For all the values of U-slot dimension, a larger E as calculated by using Equation (3), is observed.

$$l_u = 2(L_h - w) + L_v \tag{4}$$

$$l_e = l_u + \frac{0.2l}{\sqrt{\varepsilon_{re}}} \tag{5}$$

$$f_r = \frac{c}{2l_e\sqrt{\varepsilon_{re}}} \tag{6}$$

Thus the quarter wave or half wave length approximations of the slot length against the frequency do not give closer results. Hence in-depth analysis of slot cut MSAs is required to understand the slot mode. The ETMSA in above configurations, on glass epoxy substrate has, TM_{10} and TM_{11} mode resonance frequencies of 958 and 1690 MHz as shown in its resonance curve plot in **Figure 3(a)**. The surface current distributions at these two modes are shown in **Figures 3(b, c)**. At TM_{10} mode the currents

show half wavelength variation along side length (S) whereas at TM_{11} mode the currents show half wave length variations along S as well as along base of the ETMSA [1]. In the dual band ETMSA as shown in **Figure 1(a)**, the slot length l is increased in steps of 0.5 cm from 0.5 to 4.0 cm and the surface current distributions for each value of l and for different slot position (Y) were studied. For slot dimensions of l = 2.5 cm, w = 0.2 cm and Y = 2.0 cm, the dual frequencies are f_1 = 940 MHz and f_2 = 1176 MHz, as shown in the resonance curve plot in **Figure 3(a)**. The current distributions at these two frequencies are shown in **Figures 3(d, e)**. As seen from the current distributions for ETMSA and ETMSA with pair of slots and the resonance curve plot that the pair of rectangular slots perturbs the surface currents and reduces the TM_{11} mode resonance frequency from 1690 to 1176 MHz as shown in **Figure 3(a)**. Here the slots do not introduce any mode but reduces the higher order mode resonance frequency and f_2 is governed by this modified (due to the slots) TM_{11} resonance frequency. The f_1 is governed by TM_{10} mode of ETMSA, as half wavelength variation in surface currents is present along S. This frequency is also marginally affected by slots as shown in **Figure 3(a)**. The radiation pattern for ETMSA at TM_{11} mode and for slot cut ETMSA for two different slot lengths are shown in **Figures 4(a-c)**. At TM_{11} mode, the pattern is in the conical direction. However since the slots affects the current distributions on the patch, with the increasing slot length the radiation pattern becomes in the broadside direction. Also as observed from the patterns, the cross polarization levels decreases with the slot length.

Similar study is carried out for U-slot cut ETMSA. The resonance curve plot for ETMSA and for U-slot cut ETMSA (U-slot dimension: L_h = 3.0, L_v = 1.0, w = 0.2 cm) are shown in **Figure 5(a)**. The surface current distributions at the dual frequencies for U-slot cut ETMSA is shown in **Figures 5(b, c)**. As seen from the current distributions and resonance curve plots, the horizontal slot of the U-slot reduces the TM_{11} mode resonance frequency and f_2 is governed by this modified TM_{11} mode. This frequency has reduced from 1690 to 1324 MHz. The f_1 is governed by TM_{10} mode. This frequency is also reduced since the vertical U-slot length is orthogonal to surface currents at TM_{10} mode and it increases the surface currents length. The radiation patterns at f_2 for two different U-slot lengths are shown in **Figures 5(d, e)**. Similar to the above dual band ETMSA, the U-slot affects the current distributions on patch at f_2 and gives broadside radiation pattern. The cross polar level decreases with increasing U-slot length. In the following section by studying current distributions at dual frequencies the formulation of resonant length at dual frequencies for the above slot cut ETMSAs are proposed.

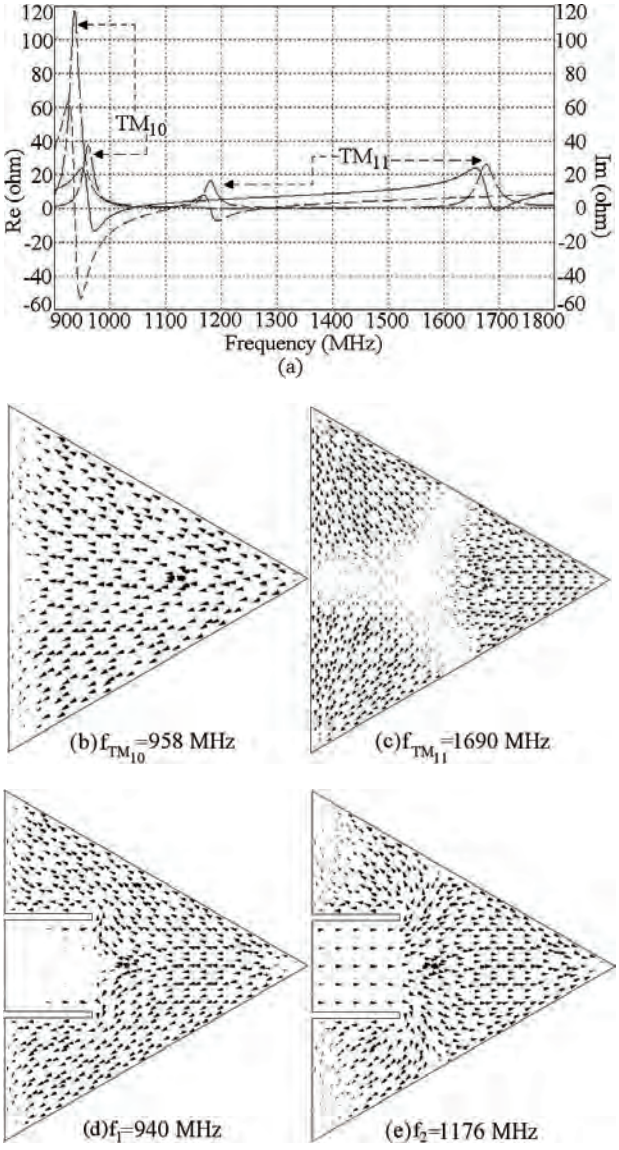

Figure 3. (a) Resonance curve plot for ETMSA (— — —) Re, (——) Im, and ETMSA with pair of slots (——-——) Re, (- - - -) Im, its (b, c) surface current distributions at TM_{10} and TM_{11} modes and surface current distributions for dual slot cut ETMSA at (d) f_1 and (e) f_2.

3. Formulation of Resonant Length for Slot Cut ETMSA

The modal variations for ETMSA in voltage and currents are with respect to the centroid of the patch [1]. For S = 10 cm, the centroid point lies at nearly 3 cm from the base of ETMSA. For TM_{10} mode the current maxima is present at the centroid point whereas at TM_{11} mode the voltage maximum is present at the centroid point [1]. Due to these different variations in current and voltage distributions at two modes, for pair of rectangular slots

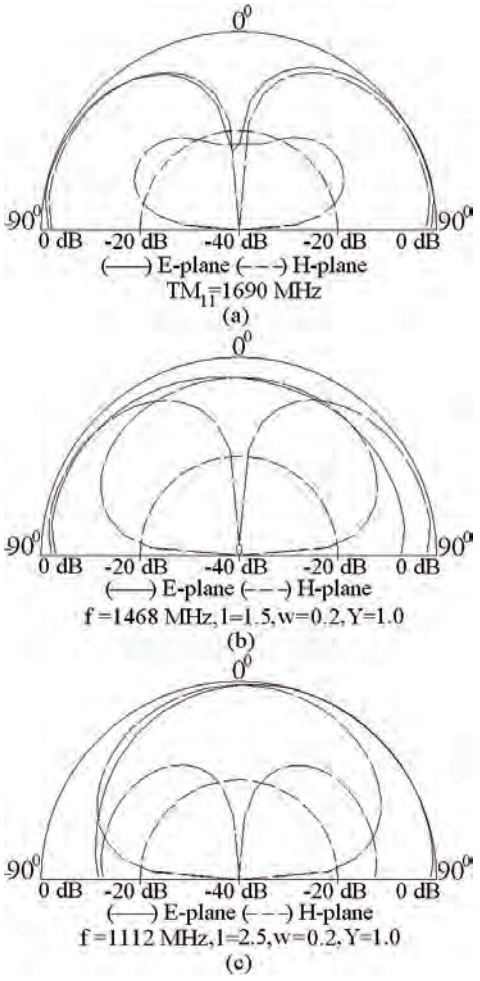

Figure 4. Radiation pattern for ETMSA at (a) TM_{11} mode and at f_2 for (b,c) different lengths of pair of slots.

cut ETMSA as shown in **Figure 1(a)**, for $l \geq 3$ cm, the decrease in f_2 is smaller whereas decrease in f_1 is larger.

The resonance frequency of ETMSA depends upon the effective side length (S_e) [1]. To formulate f_1 (modified TM_{10} mode) for pair of slots cut ETMSA, S_e is modified with respect to the l and the resonance frequency is calculated by using Equations (7) to (12).

$$W_e = \frac{S}{2} \tag{7}$$

$$\varepsilon_{re} = \frac{\varepsilon_r + 1}{2} + \frac{\varepsilon_r - 1}{2\sqrt{1 + \frac{12h}{W_e}}} \tag{8}$$

$$S_e = S + Al\sin\left(\frac{2\pi Y}{S}\right) + \frac{4h}{\sqrt{\varepsilon_{re}}} \tag{9}$$

$$A = \frac{2.8l}{S}\sqrt{\sin\left(\frac{1.2\pi l}{S}\right)} \tag{10}$$

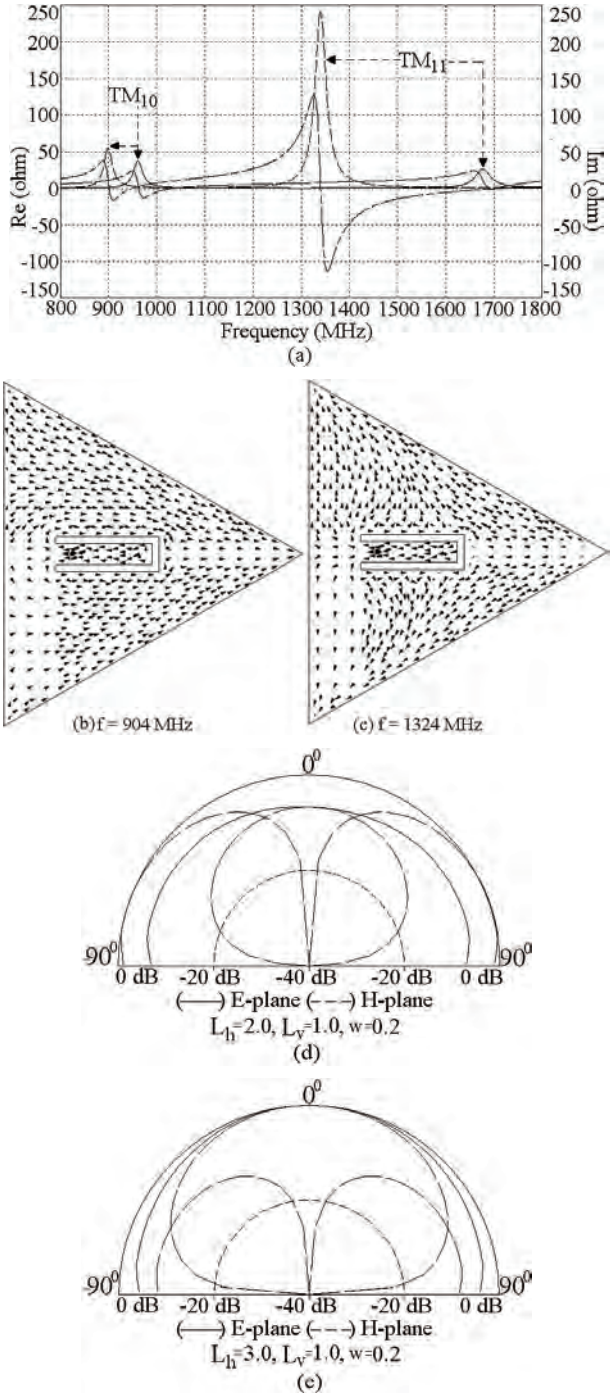

Figure 5. (a) Resonance curve plot for ETMSA (——) Re, (— — —) Im, and ETMSA with U-slot (– – –) Re, (—— – ——) Im, surface current distributions at (d) f_1 and (e) f_2 for U-slot cut ETMSA and its (d,e) radiation pattern for different U-slot lengths.

$f_1 = \frac{2c\sqrt{m^2 + mn + n^2}}{3S_e\sqrt{\varepsilon_{re}}}$, $m = 1$, $n = 0$ for TM_{10} (patch

mode) (11)

$$E = \frac{f_{ie3d} - f_1}{f_{ie3d}} \times 100 \quad (12)$$

The width as seen by the surface currents varies from base of ETMSA towards the vertex point. Towards the base, it is equal to S and towards the opposite vertex point it is nearly equal zero. Hence the effective width (W_e) is taken equal to be the average of the width along ETMSA length as given in Equation (7). The ε_{re} is calculated by using Equation (8). For smaller l, decrease in f_1 is smaller and for larger l, decrease in f_1 is larger. To account for this non-linear variation, a weighting function (A) in terms of l is used as given in Equation (10). The equation for A is derived based on the variation in frequency of TM_{10} mode against l. For a given l, with increase in Y, the perturbation in surface current length increases (or the frequency reduces) since the slots are placed towards the maximum current location. This variation is accounted by using the sinusoidal term, as given in Equation (9). The fringing field extension is accounted by the last term in the right hand side of Equation (9). The frequency is calculated by using Equation (11) and the % error (E) between the calculated and simulated values with respect to the simulated value, is calculated by using Equation (12) and they are plotted in **Figures 6(a-f)**. For the entire slot length range, an E of less than 5% is obtained. The resonant length at f_2 is formulated by modifying S_e with respect to l as given in Equations (13) to (16).

$$S_e = S + 2Al\sin\left(\frac{2\pi Y}{S}\right) + \frac{4h}{\sqrt{\varepsilon_{re}}} \quad (13)$$

$$A = \frac{5.3l}{S}\sqrt{\sin\left(\frac{2.4\pi l}{S}\right)} \quad (14)$$

$$f_2 = \frac{2c\sqrt{m^2 + mn + n^2}}{3S_e\sqrt{\varepsilon_{re}}}, \; m = 1, \; n = 1 \text{ for } TM_{11} \text{ (slot}$$

mode) (15)

$$E = \frac{f_{ie3d} - f_2}{f_{ie3d}} \times 100 \quad (16)$$

The factor '2' in Equation (13) is to account for the circulation of surface currents around the slot length. The perturbation in surface current length is modeled by using the weighting function A and the equation for the same is derived based on the frequency variation with respect to l at TM_{11} mode. The variation in the frequency with Y, for given l, is modeled by using sinusoidal function in Equation (13). The Y is varied from 1 to 3 cm and the l is varied from 0.5 to 4.0 cm. The frequency f_2 obtained

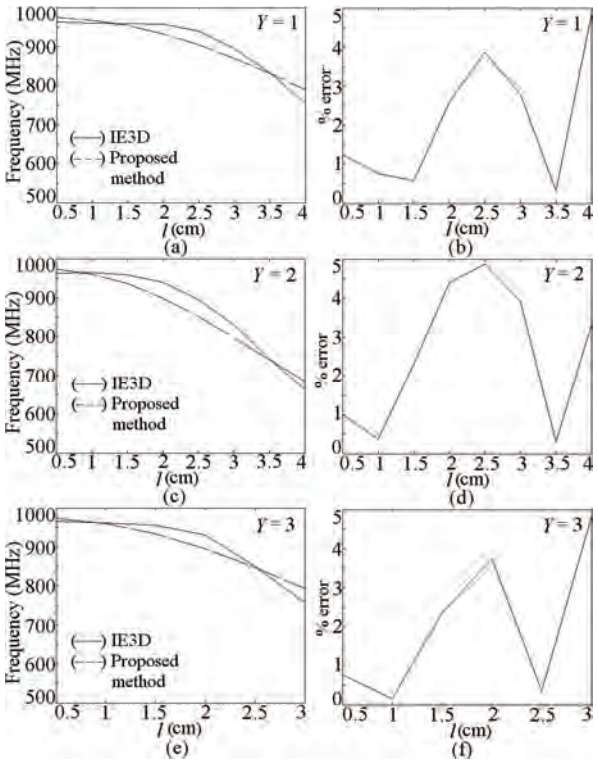

Figure 6. (a-f) Resonance frequency and % error plots for dual band pair of slots cut ETMSA at f_1.

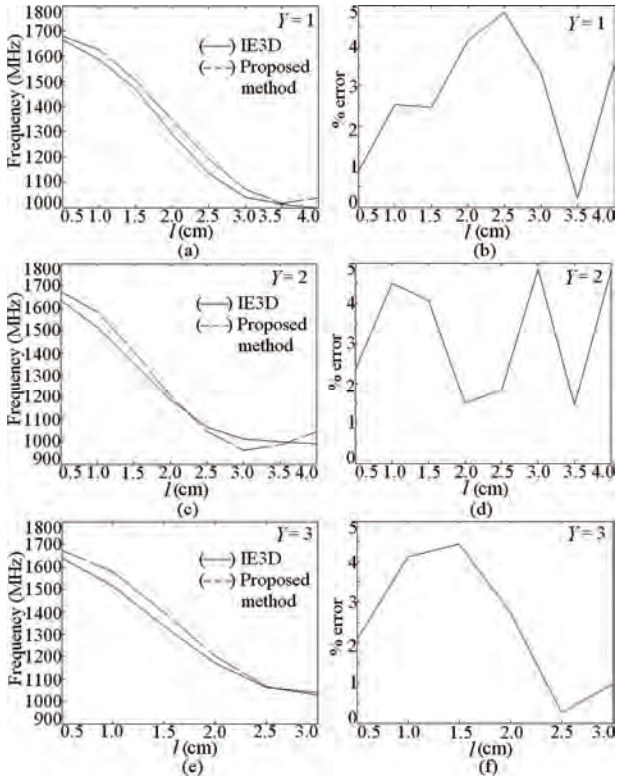

Figure 7. (a-f) Resonance frequency and % error plots for dual band pair of slots cut ETMSA at f_2.

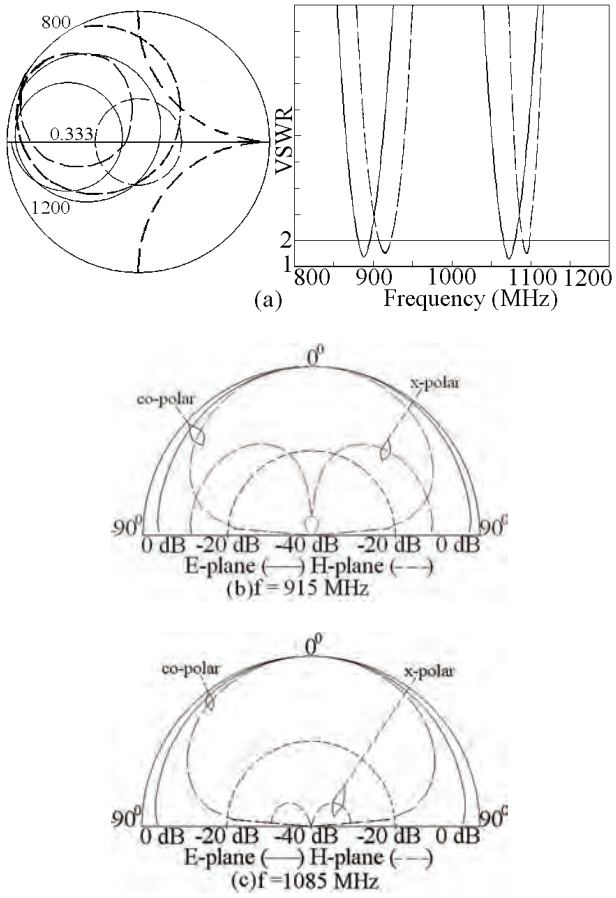

Figure 8. (a) Input impedance and VSWR plots, (——) simulated, (- - -) measured, and (b, c) measured radiation pattern for ETMSA with pair of slots.

using simulation, calculated by using Equation (15), and E calculated by using Equation (16) are plotted in **Figures 7(a-f)**. For all the values of Y, a close match is obtained between the simulated and calculated frequencies.

While designing the pair of rectangular slots cut ETMSA for the given two frequencies, the separation between the pair of slots is selected first as it affects the impedance matching at the two frequencies. Due to the ETMSA patch geometry, Y is taken to be less than S/4, so as to have larger variation in l and hence the frequency. Thus Y = 2 is selected. For the desired dual frequencies of 860 and 1060 MHz, the slot length obtained from **Figures 6** and **7** is = 2.5 cm. The slot width of 0.2 cm is selected. The slotted ETMSA is simulated and dual frequencies and BW's are 888, 1073 MHz and 15, 15 MHz, respectively as shown in **Figure 8(a)**. This response is experimentally verified and the measured frequencies and BW's are 910, 1089 MHz and 12, 13 MHz, respectively as shown in **Figure 8(a)**. The frequency values obtained using proposed equations are very close to the simulated and measured frequencies. The radiation pattern at dual frequencies is shown in **Figures 8(b, c)**. The E and H-planes at both the frequencies are aligned along $\Phi = 0^0$ and 90^0, respectively. The pattern is in the broadside direction at both the frequencies with the cross polar levels less than 12 dB as compared to the co-polar levels. Although the radiation pattern at TM_{11} mode of ETMSA is conical, but since the pair of slots affects the current distributions on the patch at f_2, the radiation pattern is in the broadside direction.

As seen from the current distributions for U-slot cut ETMSA, the U-slot affects the surface current distributions at TM_{10} as well as TM_{11} mode and realizes dual band response. At f_1, the TM_{10} mode is dominant as half wave length variation in surface currents is present along S. However due to the finite L_v, the surface current length is perturbed and the frequency is reduced. At f_2, the horizontal slots of the U-slot modify the TM_{11} mode resonance frequency and this frequency is governed by modified TM_{11} mode. The formulation of resonant length at f_1 is given by modifying S_e with respect to the U-slot dimensions as given in Equations (17) to (20).

For f_1,

$$W_e = \frac{S}{2} \tag{17}$$

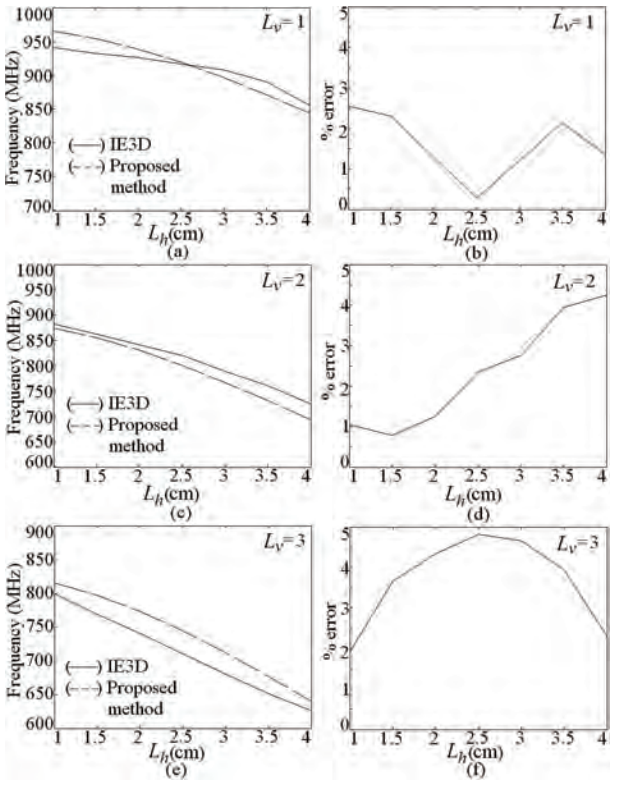

Figure 9. (a-f) Resonance frequency and % error plots for dual band U-slot cut ETMSA at f_1.

$$\varepsilon_{re} = \frac{\varepsilon_r + 1}{2} + \frac{\varepsilon_r - 1}{2\sqrt{1 + \frac{12h}{W_e}}} \quad (18)$$

$$S_e = S + BL_v + C\frac{L_h}{S} + \frac{4h}{\sqrt{\varepsilon_{re}}} \quad (19)$$

$$f_1 = \frac{2c\sqrt{m^2 + mn + n^2}}{3S_e\sqrt{\varepsilon_{re}}}, \; m = 1, \; n = 0 \text{ for } TM_{10} \text{ mode} \quad (20)$$

For narrow slots, (L_v < S/4), the perturbation in surface current length is lesser. In those cases, using B = 0 and A = 1, a closer prediction in resonant length is obtained. For L_v > S/4, the perturbation in surface current length increases and hence by using B = 0.6 and A = 2, a closer prediction in the length and the resonance frequency is obtained. The f_1 calculated by using Equation (20) and E calculated by using Equation (12) are plotted in **Figures 9(a-f)**. Using the proposed formulations, for all the slot dimensions, an E of less than 5% is obtained. At f_2, the formulation in resonant length is obtained by using Equations (21) to (23).

For f_2,

$$S_e = S + 2AL_h \sin\left(\frac{2\pi L_v}{S}\right) + \frac{4h}{\sqrt{\varepsilon_{re}}} \quad (21)$$

$$A = \frac{2.8L_h}{S} \quad (22)$$

$$f_2 = \frac{2c\sqrt{m^2 + mn + n^2}}{3S_e\sqrt{\varepsilon_{re}}}, \; m = 1, \; n = 1 \text{ for } TM_{11} \text{ mode} \quad (23)$$

Similar to pair of slots cut ETMSA, the factor '2' in Equation (21) is to account for the circulation of surface currents around the slot length. To account for the current variation in TM_{11} mode a sinusoidal function in L_v is used in Equation (21). The A is the weighting function and the relation for A is derived based on variation in frequency with respect to U-slot dimensions for TM_{11} mode. The frequency and E are calculated by using Equations (23) and (16), respectively and they are plotted in **Figures 10(a-f)**. For the entire range, frequencies calculated using the proposed formulations agrees closely with the simulated values. For designing the U-slot cut ETMSA, first the value of L_v is selected. For the dual frequencies of 900 and 1300 MHz, using L_v = 1.0 cm and w = 0.2 cm, the horizontal U-slot length obtained by using frequency plots in **Figures 9** and **10** is, L_h = 3.0. This ETMSA with U-slot is simulated using IE3D and the

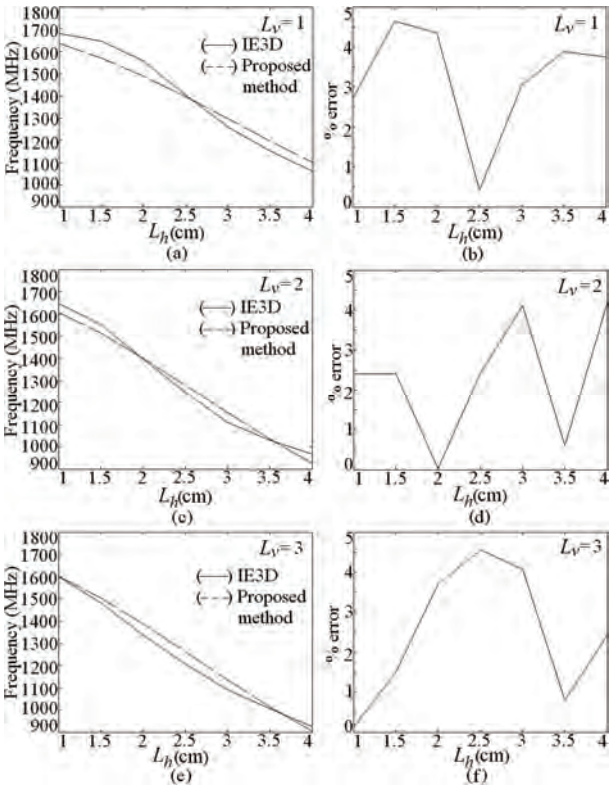

Figure 10. (a-f) Resonance frequency and % error plots for dual band U-slot cut ETMSA at f_2.

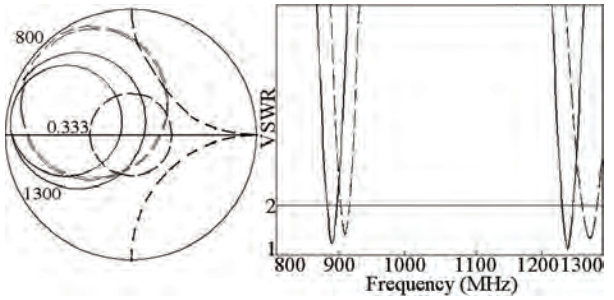

Figure 11. Input impedance and VSWR plots for ETMSA with U-slot, (—) simulated, (- - -) measured.

frequencies and BW's are 883, 1245 MHz and 15, 18 MHz, respectively as shown in **Figure 11**. The U-slot cut ETMSA is fabricated and the measured frequencies and BW's are 910, 1275 MHz and 15, 19 MHz, respectively as shown in **Figure 11**. The frequencies calculated using proposed equations agrees well with the simulated and measured results. The radiation pattern at the two frequencies is in the broadside direction. The E and H-planes are aligned at $\Phi = 0^0$ and 90^0, respectively. At f_2, a higher cross polarization is present. The cross polar level decreases with the increase in U-slot dimensions. These proposed formulations are also validated on RT-duroid substrate. Using duroid substrate, for to have

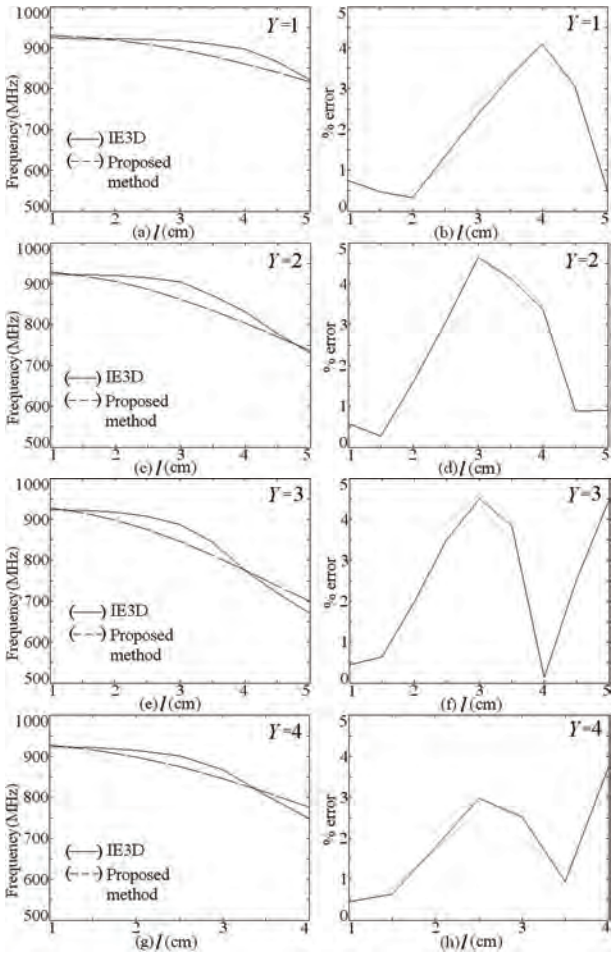

Figure 12. (a-h) Resonance frequency and % error plots for pair of slots cut ETMSA using RT-duroid substrate at f_1.

TM_{10} resonance frequency nearly equal to 950 MHz, the S equals 14 cm. For pair of rectangular slots cut ETMSA, the f_1 and f_2 obtained using IE3D and the proposed formulations and E between them are shown in **Figures 12** and **13**. For duroid substrate also a closer agreement between the two results is realized. Similar results are obtained for U-slot cut ETMSA.

4. Conclusions

The resonance frequency calculation for slot mode in pairs of rectangular slots and U-slot cut ETMSAs using quarter and half wavelength approximations are discussed. It was observed that they give closer match only for some values of slot lengths and their positions inside the patch. An in-depth modal analysis for pair of rectangular slots cut and U-slot cut ETMSA was carried out and it is observed that the slots does not introduce any mode but reduces the higher order TM_{11} resonance frequency of ETMSA and along with the fundamental TM_{10} mode realizes dual frequency response. The slots affects the current distribution on the patch at TM_{11} mode and thus with increasing slot length the radiation pattern at the frequency due to the slot becomes in the broadside direction. The cross polarization level reduces with the slot length. By studying the surface current distributions at the dual frequencies, the formulation in resonant length at dual frequencies is proposed for these slotted ETMSAs and the frequencies obtained using these formulations agree closely with the simulated as well as measured results.

REFERENCES

[1] G. Kumar and K. P. Ray, "Broadband Microstrip Antenna," Artech House, Norwood, 2003.

[2] R. Garg, P. Bhartia, I. Bahl and A. Ittipiboon, "Microstrip Antenna Design Handbook," Artech House, Norwood, 2001.

[3] K. P. Ray and D. D. Krishna, "Compact Dual Band Suspended Semicircular Microstrip Antenna with Half U-Slot," *Microwave & Optical Technology Letters*, Vol. 48, No. 10, 2006, pp. 2021-2024.

[4] K. L. Wong, "Compact and Broadband Microstrip Antennas," John Wiley & sons, Inc., New York, USA, 2002.

[5] A. E. Daniel and R. K. Shevgaonkar, "Slot-Loaded Rectangular Microstrip Antenna for Tunable Dual-Band Operation," *Microwave & Optical Technology Letters*, Vol. 44, No. 5, March 2005, pp. 441-444.

[6] J. H. Lu, "Single Feed Dual Frequency Rectangular Microstrip Antenna with Pair Step Slots," *Electronics Letters*, Vol. 35, No. 5, 1999, pp. 354-355.

[7] J. Y. Sze and K. L. Wong, "Broadband RMSA Using Tooth-Brush Shaped Slots," *Electronics Letters*, Vol. 34, No. 23, November 1998, pp. 2186-2187.

[8] A. A. Deshmukh and G. Kumar, "Even Mode Multi-Port Network Model for Slotted Dual Band Rectangular Microstrip Antennas," *Microwave & Optical Technology Letters*, Vol. 48, No. 4, 2006, pp. 798-804.

[9] A. A. Deshmukh and K. P. Ray, "Multi-Band Equilateral Triangular Microstrip Antennas," *Proceedings of Recent Advances in Microwave Theory and Applications*, Jaipur, 21-24 November 2008.

[10] J. B. Knorr and J. Saenz, "End Effect in a Shorted Slot," *IEEE Transactions on Microwave Theory & Techniques*, September 1973, pp. 579-580.

[11] IE3D 12.1, Zeland Software, Freemont, 2004.

Wireless Engineering and Technology, **2010, 1, 64-68**
doi:10.4236/wet.2010.12010 Published Online October 2010 (http://www.scirp.org/journal/wet)

Scientific Research

Design of Aperture Coupled Microstrip Antenna Using Radial Basis Function Networks

Tanushree Bose[1], Nisha Gupta[2]

[1]Department of Electronics and communication, Sikkim Manipal Institute of Technology, Majitar, India; [2]Department of Electronics and Communication Engineering, Birla Institute of Technology, Mesra, India.
Email: contact_tanushree@rediffmail.com, ngupta@bitmesra.ac.in

Received August 15th, 2010; revised September 6th, 2010; accepted September 19th, 2010.

ABSTRACT

This paper, two Artificial Neural Network (*ANN*) *models using radial basis function* (*RBF*) *nets are developed for the design of Aperture Coupled Microstrip Antennas* (*ACMSA*) *for different number of design parameters. The effect of increasing the number of design parameters on the ANN model is also discussed in this work. The performances of the models when compared are found that on decreasing the number of design parameters, accuracy of the model is increased. The results given by the prepared models are comparable with the results of the IE3D software. So, these models are accurate enough to measure the design parameters of ACMSAs. Thus the neural network approach eliminates the long time consuming process of finding various designing parameters using costly software packages.*

Keywords*: *Artificial Neural Network, RBF Nets, ACMSA

1. Introduction

The artificial neural network can be referred to as an artificial human brain which processes data after proper training. Three basic aspects of a neuronal model are [1-2]:

- It consists of a large number of processing elements like neurons and nodes
- Each nodes connect to a large number of other neurons and
- The functionality of the network is determined by modifying the strengths of the connection during the learning phase.

Ability, adaptive capability and ease of implementation have made ANN a popular tool for many design problems in today's communication world. These networks directly give almost accurate result eliminating the various time consuming complex computations required for different works. In the present scenario, the neural network models are used extensively for wireless communication engineering, which eliminates the complex and time consuming mathematical procedures of designing antennas, like Method of Moments (MOM) [4-6].

In recent years, Wide band and Ultra wide band (UWB) technology have experienced many significant developments. Printed antennas play a very important role in this area because of their simple structure, ease of construction, low cost, conformal to planar, low profile, reproducibility and ease of integration with solid state devices [3]. However, the analysis of printed antennas is complex and exhaustive. To optimize the antenna efficiency for transmitting and receiving modes, the patch impedance should match with the feed hence it becomes very necessary to optimize the feed position. Moreover, the dimensions of antenna along with its feed line and dielectric of the substrate are other parameters which are to be optimized for antenna to operate in a desired resonant frequency or frequency band in case wide band and UWB operation [7-11]. Determination of these parameters is tedious, cumbersome and time consuming process.

In this proposed work, due to the high demand of wide band antennas in wireless communication, ACMSA's design problems are taken under consideration. The error percentage in the first ANN model which is developed using RBF nets to give nine design parameters of the ACMSA is quite high while the time consumed by it is very low when it is compared with the one developed using Back propagation algorithm [12]. Since ACMSA is commonly used in wide band application, the relative error given by the ANN model developed using Radial Basis Function (RBF) is acceptable as the minimum frequency in the operating frequency band have a large

space to resonate within the band. Still a low error percentage from the ANN models is always desirable, hence the second RBF-ANN model is developed to give only two design parameters of an ACMSA keeping other parameters fixed at some predetermined value. Both the models can be used to design an ACMSA for a desired minimum frequency in the frequency band ranging from 1.5 GHz to 8.9 GHz.

2. Antenna Design

The geometry and the design parameters under consideration of an ACMSA are shown in **Figure 1** and **Figure 2**, respectively. It consists of two substrates separated by a ground plane. The top substrate (ε_r^a) contains the radiating element, and the bottom substrate (ε_r^b) contains the microstrip feed line. A small aperture is cut in the ground plane to allow coupling from open circuited microstrip feedline to the radiating patch. The parameters on which resonant frequency of the antenna depends upon are shape and dimensions of the radiating element, dimensions of the ground plane, shape and size of the aperture, dimensions of feedline, position of feedline and the dielectric constants of the two substrates [13-18].

An ACMSA can be designed for different frequencies using FR 4 sheet because of its easy availability. The shape of radiating element and aperture are chosen to be rectangular. The output parameters determined during the design of an antenna are:

(a) Dimensions of ground plane (L_g, W_g)
(b) Dimensions of aperture ($L_{ap,}$ W_{ap})
(c) Dimensions of radiating element (L_p, W_p)
(d) Dimensions of feed (L_f, W_f)
(e) Feed position (X, Y = 0)

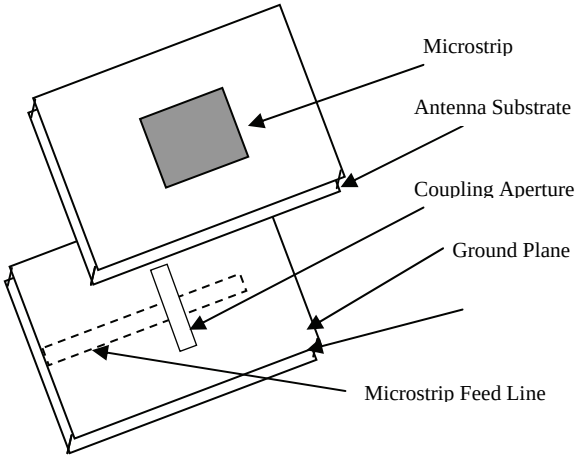

Figure 1. Geometry of an ACMSA.

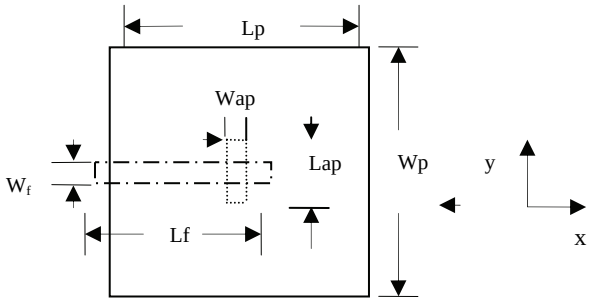

Figure 2. Design parameters in an ACMSA.

3. Development of ANN Model

The construction of RBF network, in its most basic form, involves three layers with entirely different roles. The input layer is made up of source nodes (sensory units) that connect the network to its environment. The second layer, the only hidden layer in the network applies a nonlinear transformation from the input space to the hidden space. In most applications the hidden space is of high dimensionality. The output layer is linear, supplying the response of the network to the activation pattern applied to the input layer. A RBF net architecture is given in **Figure 3**.

Radial Basis function networks are substantially faster than the methods used to train multi-layer perceptron networks. This follows from the interpretations which can be given to the internal representation formed by the hidden units, and leads to a two stage training procedure. In the first stage, the parameters governing the basis functions (corresponding to hidden units) are determined using relatively fast, unsupervised methods, in which it uses only input data and not the target data. The second stage of training then involves the determination of the final-layer weights, which requires the solution of a linear problem, and which is therefore also fast.

The trained neural network provides a special approximation where the exact results of the numerical

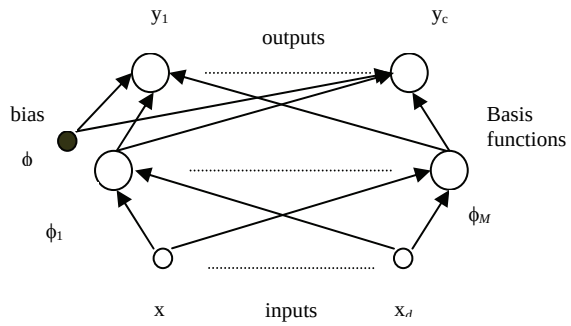

Figure 3. A RBF network architecture.

analysis, which are hidden in the training patterns, are used for neural computation and give us directly all the required designing parameter of an antenna for a desired frequency. That way, a computationally modest neural network model can replace a numerical analysis for parameters differing from training patterns.

4. Results and Discussions

In this proposed work, first an ANN model for aperture coupled microstrip antenna, considering nine design parameters is developed using RBF network. The simulated values which are trained for the model development and the antenna configurations are obtained from the IE3D software, which is a commercial simulator based on the moment of methods. The number of training data is increased by the method of interpolation which is quite reliable because interpolation technique is applied on the graph that is obtained from the simulated data. The network is trained with radial basis function network, whose performance goal was taken as 0.0001% and spread constant is 400. For 831 input/output training samples, the network requires only 4 minutes for training, and Relative error (percentage error) is found to lie within 20% to 60%. The time taken to develop the same model using RBF network is very less while error% is quite high than that found with the model which was prepared using BPA network [7]. Relative error is calculated using the formula as follows:

$$\textit{Relative Error} = [(\textit{Simulated Value} - \textit{ANN Value}) / \textit{Simulated value}] \ *100 \quad (1)$$

The network is tested for 10 random frequencies. Those input frequencies are compared with the resonant frequencies obtained from IE3D software for the corresponding output parameters given by the network. The results are tabulated in **Table 1** for all the parameters, which also compare the simulated value with the one obtained from the ANN model.

From **Table 1** one can estimate that the prepared network or model is good enough for determining the various design parameters of an ACMSA operating between 1.5 GHz and 8.9 GHz. The above mentioned characteristics of the ACMSA obtained from the ANN model are found to have high errors but due to the wide band property of ACMSA, the errors are still acceptable. The reason behind this high error is cumulative error caused by large number of design parameters taken under consideration. To reduce this, next an ANN model is developed considering only two design parameters.

Now, a RBF – ANN model for two design parameters is developed keeping the configuration of RBF net same as that developed for the design of ACMSA for nine design parameters. The developed RBF – ANN model for two design parameters of ACMSA is checked for 10 random frequencies. The design parameters given by this model when simulated using IE3D software gives the expected results and it is found that error % is reduced highly. Comparison of the minimum frequency in the frequency band obtained by simulated and the RBF-ANN model for two design parameters for ACMSA is tabulated in **Table 2**. The error % is found to lie between 0.2% and 10% and time taken to develop this model is just 10 seconds.

The time taken for the development of the ANN model using RBF nets is very less and this learning method is good for the development of such ANN model which is used to obtain less number of design parameters. If the design parameters are increased, error % increases which in turn affects the efficiency of the ANN model. For large number of design parameters, training should be

Table 1. Error measurement for the simulated f_r from IE3D and the NN model using radial basis network for the design of ACMSA for nine design parameters.

S.N.	Input Parameters									Output Parameters		
	L_g (mm)	W_g (mm)	L_{ap} (mm)	W_{ap} (mm)	L_p (mm)	W_p (mm)	L_f (mm)	W_f (mm)	X	f_r (GHz) (IE3D)	f_r (GHz) (NN)	% Error
1.	65.6130	67.5983	4.0165	4.0165	60.9313	62.9464	38.3829	8.4919	−158256	1.302	1.5	23.98
2.	57.0427	57.8659	3.5287	3.5287	51.6755	51.8765	34.3563	7.3930	−13.6118	2.31	1.8	22.08
3.	43.1930	41.6296	2.7400	2.7400	36.4645	34.1344	26.7684	5.5737	−10.0244	1.52667	2.44	−57.20
4.	41.2692	39.3054	2.6301	2.6301	34.3180	31.6929	25.6668	5.3156	−95239	1.60333	2.5	55.9
5.	36.0778	32.9440	2.3340	2.3340	28.4860	25.1383	22.6161	4.6115	−8.1762	1.81	2.8	54.7
6.	30.6364	26.0827	2.0237	2.0237	22.2907	18.3922	19.2635	3.8603	−6.7665	2.112	3.18	−50.57
7.	26.9157	21.2448	1.8121	1.8121	18.0016	13.8922	16.8436	3.3383	−5.8076	2.365	3.5	−47.99
8.	21.0075	13.2507	1.4789	1.4789	11.1090	7.1695	12.6600	2.4978	−4.3115	2.995	4.2	−40.23
9.	16.3552	6.6940	1.2278	1.2278	5.7907	3.0094	8.7977	1.8630	−3.2333	3.76	5.2	−38.3
10.	14.1618	4.0632	1.1306	1.1306	3.9040	2.6344	6.6903	1.6809	−2.9008	4.27	6.2	−45.2

Table 2. Error measurement for the simulated f_r from IE3D and the NN model using RBF network for the design of ACMSA for 2design parameters.

S.N.	Input Parameters		Output Parameters		
	L_g	W_g	f_r (GHz) IE3D	f_r (GHz)NN	Error%
1.	28.1095	28.1095	2.21	2.2	0.45
2.	25.9323	25.9323	2.39	2.4	−0.42
3.	18.5848	18.5848	3.18	3.2	−0.63
4.	17.0883	17.0883	3.37	3.4	−0.89
5.	14.5039	14.5039	3.85	3.8	1.299
6.	12.4640	12.4640	4.39	4.2	4.328
7.	11.6484	11.6484	4.64	4.4	5.172
8.	10.4255	10.4255	5.06	4.8	5.138
9.	9.7474	9.7474	5.31	5.2	2.072
10.	9.7513	9.7513	5.32	5.8	−9.023

Table 3. Comparison of mean error % and time taken by different ANN models, for the design of ACMSA.

S.N.	Number of Design Parameters	Time taken to develop BPA-ANN model	Mean Error % given by BPA-ANN model	Time taken to develop RBF-ANN model	Mean Error % given by RBF-ANN model
1.	9	1 hr	1.39657	4 min	43.615
2.	2	5 min	0.59	10 sec	2.94

Table 4. Comparison showing minimum frequency obtained from different methods.

S. N	Frequency Obtained From ANN Model (GHz)	Frequency Obtained From IE3D (GHz)	Frequency Obtained From Prototype Model Fabricated (GHz)
1.	2.44	1.52667	2.46

done using back propagation algorithm. **Table 3** shows the comparison of mean error % and time taken for the development of the different ANN models. Mean error % is calculated as given in Equation (2) and a comparison of the resonant frequencies obtained by ANN model, IE3D software and the prototype model when measured in vector network analyzer is shown in **Table 4**.

$$Mean = \Sigma\ |RelativeError|/10 \quad (2)$$

5. Conclusions

The trained networks are very useful as they give all the design parameters of the ACMSA for any desired resonant frequency. A distinct advantage of neural computation is that, after proper training, a neural network completely bypasses repeated use of complex iterative processes for new design presented to it. This work can be extended for various dielectric constants for different radiating patch.

REFERENCES

[1] S. Haykin, "Neural Networks A Comprehensive Foundation," Pearson Educartion Pte. Ltd., Singapore, 2004.

[2] S. N. Sivanandam, S. Sumathi and S. N. Deepa, "Introduction to Neural Networks using Matlab 6.0," Tata McGraw-Hill, New Delhi, 2006.

[3] C. A. Balanis, "Antenna Theory Analysis and Design," John Wiley & Sons, Inc., New York, 2005.

[4] R. K. Mishra and A. Patnaik, "Neural Network-Based CAD Model for the Design of Square Patch Antennas," *IEEE Ttransactions on Antennas and Propagation*, Vol. 46, No. 12, December 1998, pp. 1890-1891.

[5] R. K. Mishra and A. Patnaik, "Neorospectral Computation for Complex Resonant Frequency of Microstrip Resonators," *IEEE Microwave and Guided Wave Letters*, Vol. 9, No. 9, September 1999, pp 351-353.

[6] A. Patnaik and R. K. Mishra, "ANN Techniques in Microwave Engineering," *IEEE Microwave Magazine*, Vol. 4, No. 1, March 2003, pp. 55-60.

[7] Z. Wang, "Design of Low-SAR Antennas for Mobile Communications Devices," Ph.D. Thesis, 2001.

[8] D. K. Cheng, "Field and Wave Electromagnetics," 2nd Edition, Addison Wesley, Reading, 1989.

[9] E. Antonino-Daviu, M. Cabedo-Fabre´s, M. Ferrando-Bataller and A. Valero-Nogueira, "Wideband Double-Fed Planar Monopole Antennas," *Electronics Letters*, Vol. 39 No. 23, November 2003, pp. 1635-1636

[10] K.-L. Wong, C.-H. Wu and S.-W. (Stephen) Su, "Ultrawide-Band Square Planar Metal-Plate Monopole Antenna with a Trident - Shaped Feeding Strip," *IEEE Transactions on Antennas and Propagation*, Vol. 53, No. 4, April 2005, pp. 1254-1261

[11] J. Jung, W. Choi and J. Choi, "A Small Wideband Micro-

strip Fed Monopole Antenna," *IEEE Microwave and Wireless Components Letters*, Vol. 15, No. 10, October 2005, p. 630.

[12] T. Bose and N. Gupta, "Neural Network Model for Aperture Coupled Microstrip Antennas," *Microwave Review*, September 2008.

[13] T. K. Lo, C. O. Ho, Y. Hwang, E. K. W. Lam and B. Lee, "Miniature Aperture-Coupled Microstrip Antenna of Very High Permittivity," *Electronics Letters*, Vol. 33, No. 17, January 1997, pp. 9-10.

[14] R. B. Waterhouse, S. D. Targonski and D. M. Kokotoff, "Design and Performance of Small Printed Antennas," *IEEE Transactions on Antennas and Propagation*, Vol. 46, No. 12, 1998, pp. 1629-1633.

[15] M. A. Saed, "Efficient Method for Analysis and Design of Aperture Coupled Rectangular Microstrip Antenna," *IEEE Transactions on Antenna Propagation*, Vol. AP-41, 1993, pp. 986-988.

[16] P. L. Sullivian and D. H. Schaubert, "Analysis of an Aperture Coupled Microstrip Antenna," *IEEE Transactions on Antenna propagation*, Vol. AP-34, 1986, pp. 977-984.

[17] A. Ittipibbon, *et al*., "A Modal Expansion Method of Analysis and Measurement on Aperture-Coupled Microstrip Antennas," *IEEE Transactions on Antenna Propagation*, Vol. Ap-39, 1991, pp. 1567-1574.

[18] V. Rathi, G. Kumar and K. P. Ray, "Improved Coupling for Aperture Coupled Microstrip Antennas," *IEEE Transactions on Antenna Propagation*, Vol. AP-44, No. 8, 1996, pp. 1196-1198.

Wireless Engineering and Technology, **2010, 1, 69-80**
doi:10.4236/wet.2010.12011 Published Online October 2010 (http://www.scirp.org/journal/wet)

Scientific Research

Ad Hoc Network Hybrid Management Protocol Based on Genetic Classifiers

Fabio Garzia, Cristina Perna, Roberto Cusani

Information, Electronics and Telecommunication Engineering Department, SAPIENZA – University of Rome, Rome, Italy.
Email: fabio.garzia@uniroma1.it

Received August 24th, 2010; revised September 8th, 2010; accepted September 27th, 2010.

ABSTRACT

The purpose of this paper is to solve the problem of Ad Hoc network routing protocol using a Genetic Algorithm based approach. In particular, the greater reliability and efficiency, in term of duration of communication paths, due to the introduction of Genetic Classifier is demonstrated.

Keywords*: *Ad Hoc Networks, Genetic Algorithms, Genetic Classifier Systems, Routing protocols, Rule-Based Processing

1. Introduction

Ad Hoc networks differ from the traditional networks due to the absence of a fixed infrastructure, to the mobility of hosts, to channel sharing capabilities and to limited available band. These differences make the protocol for wired net not useful for Ad Hoc net.

A lot of studies were made to try to adapt the robust wired net protocol to Ad Hoc net protocol [1].

In particular Ad Hoc networks need routing protocols that are capable of adapting to the variation of topology of the net, guaranteeing an acceptable throughput even in the presence of a high number of terminals. The mentioned protocols must therefore guarantee a high reliability of the net together with an energy waste reduction.

A plenty of solutions was proposed for this purpose [2-7] even if their performances are not very satisfying for Ad Hoc networks.

More exactly, the proactive protocols tend to show a particular stability for the net even if they suffer by band waste due to need of updating the topological data net even in the absence of real and effective changes.

On the other hand, reactive protocols operate in a different way, facing more rapidly the topological change of the net, even if they suffer by packet lost when the changes become too fast [2].

An attempt of overcoming the mentioned protocols is represented by the hybrid protocols that try to use the better features of both proactive and reactive protocols [8,9].

The study of a proper hybrid protocol is the purpose of the present paper. In particular the problem is solved using a Genetic Algorithm (GA) approach showing very interesting results both from reliability and efficiency point of view in term of duration of communication paths.

The great advantage of the proposed technique is represented by the capabilities of Genetic Classifiers (GCs) of selecting, basing on the environmental information and on the experience acquired with time, the better path between different nodes, in term of duration of communication paths.

In the following, after illustrating the general principles of Ad Hoc network routing protocols (Section 2), the principles of GC are shown (Section 3); after that the proposed protocol (Section 4) the related obtained results (Section 5) and the generalization (Section 6) are shown, followed by conclusions (Section 7).

2. Ad Hoc Networks Routing Protocols

To understand the purpose of the present work it is necessary to make an overview of the actual Ad Hoc routine protocols.

It is evident that the goodness of a protocol routine depends on the amount of information available about the net. In an Ad Hoc network, due to the mobility of the nodes, it is necessary to exchange a high amount of information to keep the nodes updated. This implies a band consumption due to the need of exchanging signalling information and consequentially energy consumption.

An efficient routing protocol must guarantee the reliability of the net, reducing at the same time band and energy waste.

Actually two main routing protocol are available, that are proactive and reactive [10-13] each of them characterized by positive and negative features.

Proactive protocols try to keep the knowledge of all the nodes, exchanging routing information without taking care if the path is really used for communications. Every node stores the necessary routing information and it is responsible for the propagation of topological change of the net.

These features contribute to reduce the delay related to the research of paths but at the same time produce a band and energy waste.

Reactive protocols reduce the above mentioned problems since they avoid of making periodical broadcast transmission, seeking a route only when it is strictly necessary.

On the other side, they generate a high traffic volume when a route is researched, generating delay. Further the lack of a global view of the net decrease the reliability of the net itself.

The partial inefficiency of the above mentioned protocol has led to the development of a third typology that tries to take the better features of the other two classes.

Hybrid protocols try to realize an on-demand protocol with a limited research cost. The most common is the ZRP protocol [14-17] that uses the advantage of proactive route discovery in a limited area and the advantage of reactive protocol to transmit this information between the different local areas.

Since in an Ad Hoc network the most of communications take place between adjacent nodes, the topological variations are more relevant near the node more distant, where the adding or the subtraction of another node have a certain impact.

The separation in local areas allows the applications of different algorithms, improving the general performances of the net.

For this reason the present work is aimed at studying a new kind of hybrid protocol adding a proper genetic algorithm (GA) based core that allows the system to learn directly from the environment, ensuring reliability and flexibility.

Before starting with the explication of the studied protocol, it is necessary an overview of GA and Genetic Classifiers.

3. Genetic Classifiers

A genetic classifier is essentially a classifier system endowed by proper Genetic Algorithms that manage its activities.

GCs have revealed to be extremely useful in a plenty of applications [18-21].

3.1. Structure

A classifier system is an automatic knowledge machine that is capable of learning simple rules, called classifiers, to finalize its behaviour in an arbitrary environment according to determined needs.

It's structure can be described using a methodology similar to the one used for dynamic systems, that is:

1) a group of fixed length strings (classifiers), which represents the behavioural rules, based on a ternary alphabet, composed by a condition and an action. Every classifier is labelled with a value that represents its strength (fitness) as a function of the results obtained operating according to the action suggested by the classifier itself;

2) a series of inputs that receive the information from the external environment and determine which classifier must be activated;

3) an auction mechanism that determines which of the activated classifier is effectively acting;

4) an accountability system that updates the values of each classifier basing on the premium received according to the decision acted;

5) a genetic algorithm that is capable of introducing new set of rules substituting the older ones. The algorithm is generally activated when an input message does not correspond to any classifier already present inside the system.

3.2. Principles

The system can be reduced to 3 fundamental points that are shown in **Figure 1**.

The system of rules and messages present in the classifier system is a special kind of operative system. It represents a computational scheme that uses properly rules to reach the desired goal. It has been demonstrated [22,23] that these systems are computationally complete and efficient. Although different syntaxes are available as a function of the working scheme chosen, generally the

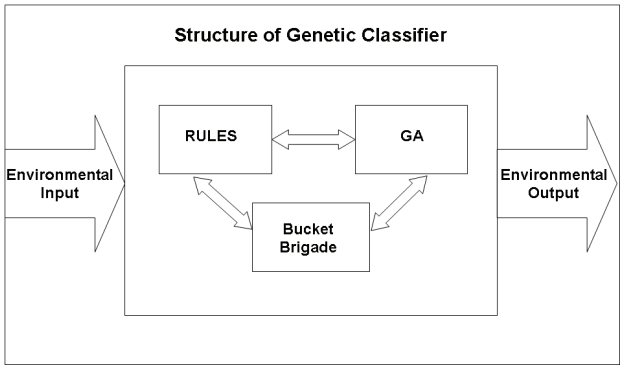

Figure 1. Scheme of a genetic classifier.

rules can be represented as:

if <*condition*> *then* <*action*> (1)

The above rules means that the action is immediately executed if the condition is satisfied.

The classifier systems adopt a fixed length representation for the rules and allow the activation and the use of parallel rules.

The system of rules and messages constitutes the computational core of the classifier. The information propagate from the environment, through the inputs, and they are decoded into one or more than one fixed length messages. These messages can activate the related rules that are inserted in a proper list of messages.

Once a classifier is activated, it sends its message to the list above mentioned. These messages can, in a second time, activate other messages or generate an action through the actuator towards the external environment using proper effectors. In this way the classifiers combine their suggestions and the environmental suggestions to determine the future behaviour of the whole system.

To understand this mechanism, it is better analyse into details how the messages and the classifiers are used inside the system.

A message inside the system is simply a finite length string, composed using a finite alphabet. Since we limit, in our case, at using a binary alphabet, its precise definitions is:

<*message*>::={0,1} (2)

A message is therefore defined as a sequence of 1 and 0 and it represents the fundamental instrument for information exchange inside the whole system.

Messages inside the list can be coupled with one or more than one rules. A classifier is therefore a working rule defined as:

<*classifier*>::=<*condition*>:<*message*> (3)

where the condition is defined as:

<*condition*>::={0,1,#} (4)

It is immediate to note that the definition of a condition differs from the definition of message exclusively for the introduction of a special character (#) that implies a "don't care" situation. A condition is therefore coupled with a message if, in any position of its string, a 0 couple with a 0, a 1 couple with a 1, or a "don't care" # couple with a 0 or a 1.

Once a condition of the classifier is coupled, the related classifier becomes a candidate to send its message to the list of messages in the following step. The possibility of sending its message to the list is defined basing on the strength of the message itself through a proper auction involving all the activated rules.

For this reason it is necessary to introduce a credit assignment algorithm that allows each classifier to be labelled with a proper strength value.

The most used algorithm for this kind of functionality is the so called bucket brigade [24]. To better understand its behaviour, a metaphor has been used using two main components that are an auction and a clearing house.

When the classifiers are coupled, they do not send immediately their message to the list but they participate to an auction. Each message can participate to the auction thanks to its strength that represents a concept similar to the fitness in the genetic algorithm that is the goodness of its property in solving the defined problem. Every classifier makes a bid B proportional to its strength, that is:

$$Bi=Cbid*Si \quad (5)$$

where *Bi* is the bid, *Si* is the strength of the classifier and *Cbid* is a proper proportionality constant.

In this way, the rules characterized by greater fitness values are classifiers to be selected to send its message. The auction allows a particular rule that has been selected through the auction to delete its bid by means of the clearing house in the case of a remainder coupling with the remaining messages.

The payment of the bid is divided between the classifiers that couple in different ways; this payoff division helps the whole system to guarantee the formation of a correctly dimensioned messages subpopulation.

Genetic algorithm is the third and fundamental point of a classifier system [25].

The GA used inside the proposed genetic classifier system is operative according the following steps:

1) code of the problem;

2) creation of the initial population of potential solutions;

3) creation of a fitness function that allows each solution to be assigned with a value that estimates its suitability;

4) formalization of genetic operators (crossover, mutation, etc.) that alters the next generation chromosomes;

5) assignment of values to the different parameters that regulate the evolution (population dimension, probability of application of genetic operators);

6) definition of stop condition.

In our case the genetic algorithm try to evolve, learning new rules of the kind "if <condition> then <action>" that allows the genetic classifier to operate in the better way inside the considered system.

The fitness of the rules is evaluated considering their performances in term of correctness of time duration predictions of desired paths. In this way the genetic algorithm introduces new sets of rules inside the system, deleting the older one, allowing the classifier of reaching in

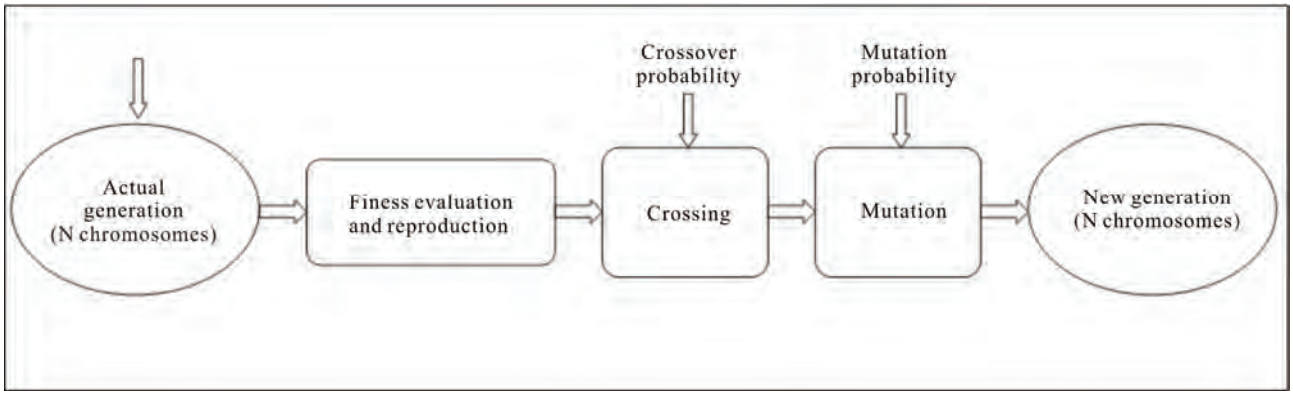

Figure 2. Operative scheme of genetic algorithms.

the better way its regime condition. The used fitness function is illustrated in the next paragraph. The algorithm stops according to the chosen stopping conditions. Even in this case, it does not exist predefined conditions, and a stop condition related to the degree of fitness reached has been chosen.

The selection process is implemented by means of the so-called roulette wheel selection where the value of the strength S of every classifier represents its fitness score.

4. Proposed Hybrid Protocol

We already said in the previous section that a proper hybrid protocol based on genetic classifier has been developed to increase the reliability of Ad Hoc network.

In the following the features of the considered protocol are illustrated.

The whole net is composed by the union of coverage areas of the different nodes.

Each node of the network samples, at regular time intervals, the signal level of the nodes located in its coverage area, normalizing them in percentage, and uses them as rules to estimate future lasting of the paths between the node itself and the measured nodes.

The structure of the rules is:

If <$sample_0$, $sample_{-1Ts0}$,……; $sample_{-(N-2)Ts0}$, $sample_{-(N-1)Ts0}$> *then* <*estimated duration of path*> (6)

where T_{s0} is the sampling time, <$sample_{-iTs0}$> is the signal sample of the node measured at –i T_{s0} time and N in the number of samples used by the rules.

The information coming from the net are stored as environmental messages that determine which classifier must be activated basing on the result of matching operation between strings of bits.

At the same time different rules can match their condition with the description of information coming from the environment: in this case a proper auction mechanism is activated to select the most fitting classifier.

The selected rules pays a certain fee proportional to its patrimony, that is divided between the classifier that have activated it, increasing their values.

The strength of a group of rules is evaluated considering the performance of the net in term of prediction of duration of time of paths. In this way the GA introduces new set of rules inside the system, substituting the older one, allowing the GC to reach its better performance in a quite short time.

The result of this working principle is a numerical value that represents the estimated temporal lasting of each path, allowing the choice of the more correct one for any particular purpose.

After a certain time, depending on the variability of the net, the GC starts to work correctly, giving to the net a high reliability, that is the purpose of the present work.

Each node keeps the operative information of the other nodes into two separated tables:

1) signal level samples table;

2) routes table.

The signal level samples table stores the information related to the nodes that are currently into the coverage area of each node. The structure of the data is:

<$node_j$> <$sample_{j,0}$, $sample_{j,-1Ts0}$, ……; $sample_{j,-(N-2)Ts0}$, $sample_{j,-(N-1)Ts0}$ > (7)

where <$node_j$> is the measured node j and <$sample_{j,-iTs0}$> is the signal samples of the node j measured at –i T_{s0} time.

The routes table stores the information related to the available paths of the considered node. The structure of the data is:

<*destination node*> <*source node*> <*estimated duration of path*> <*time of evaluation*> (8)

where <destination node> is the node that must be reached which can be in the coverage area of the considered node or in the coverage area of another node, <source node> is the starting node that can be the considered the node itself (in this case the destination node is a node located in the coverage area of the considered node) or a

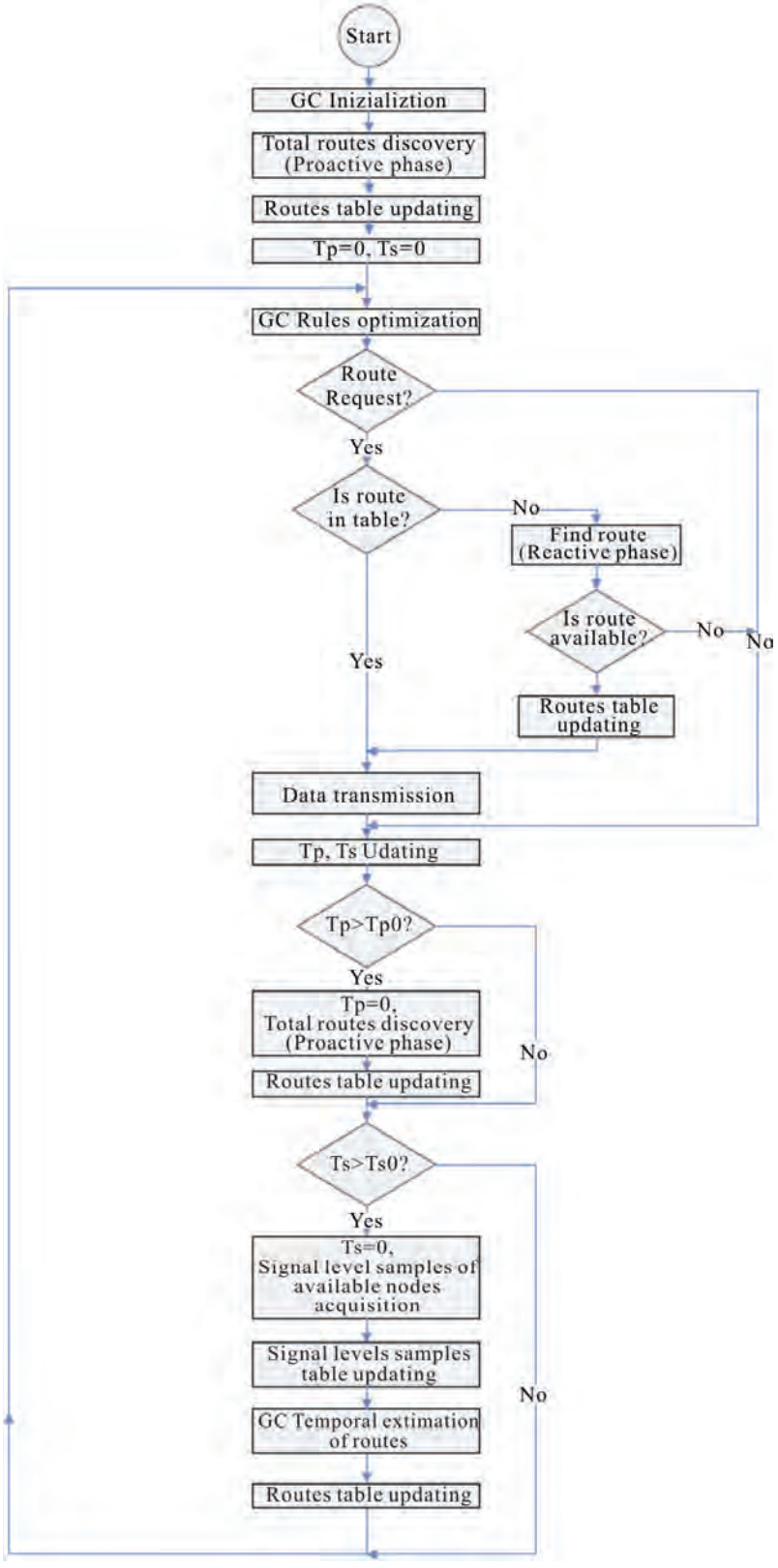

Figure 3. State diagram of the proposed algorithm.

node located in the coverage area of the node (in this case the source node owns the information to route the data to be transmitted towards the destination node), <estimated duration of path> is the value of duration of path estimated by the genetic controller using the relative data samples stored into the signal level samples table, <time of evaluation> is the time at which the duration of path evaluation was made, allowing to know, when a route request is made, if the route is still valid or how long it will be valid.

Every node is endowed by a genetic classifier that, starting from the environmental information constituted by the signal level samples of nearby nodes, is capable of choosing correctly the route where to send the data packets. This choice is made basing not on the mean strength of the links but on the more reliable and lasting link, using the information acquired from the net.

The state diagram of the used algorithm is shown in **Figure 3**.

At the begin the genetic controller is initialized with the desired number of rules, composed by N temporal signal samples, in a random way, since the algorithm doesn't know anything about the environment to be controlled. For this reason the rules are initialized with random values that are correctly updated with time.

Since the node has just been activated, it doesn't know anything about the available routes and a total route discovery routine is activated, so that it immediately knows the available routes, without being able to estimate their duration, since signal samples (to be evaluated) are not yet available. This step is a typical proactive action.

After the total routes discovery step, the received information are stored into the routes table and are available for the node itself or for the other nodes.

Then, the timer variables T_p for regular proactive action and T_s for regular signal level sampling of nodes located into the coverage area of the considered node are set to zero, to start the main cycle of the algorithm.

At this point the main cycle of the algorithm starts.

The first procedure is the rules optimization executed by the genetic controller. In this procedure the estimated duration of paths by means of rules containing signal level samples are compared with the real observed durations and are properly updated to become more and more precise in their estimation. At the same time new rules are generated by the genetic algorithm contained in the genetic controller. These new rules can be useful for duration estimation (and in this case they are conserved) but they can also be not useful (in this case there are deleted and substituted with more performing rules).

At this point a route request control is made. If there is a request, the algorithm checks if the requested route is stored into the routes table and if it is not expired. If the route is present in table and still valid, it starts the data transmission, according to the estimated duration of route. If the route is not present into the routes table, a find route procedure is executed, that is a typical reactive action. If the route is not found, nothing can be made by the node and the algorithm continues its regular flow. If one or more routes are found, the routes table is updated and the data are transmitted.

If after the genetic controller optimization any route request is made, the algorithm continues its regular flow.

At this point the timer variables T_p and T_s, are updated and temporal checks are made: if $T_p > T_{p0}$ (where T_{p0} is a design constant that forces the system to execute the proactive procedure), T_p is set to zero and a total routes discovery routine is executed, that is a typical proactive action, and the results are stored into the routes table. The continuous update of the routes causes a considerable use of the net resources. For this reason it is updated at regular intervals T_{p0} more than continuously, realizing a compromise between efficiency of the net and reduction of energy and band consumption.

If $T_p < T_{p0}$ no action is made.

If $T_s > T_{s0}$ (where T_{s0} is a design constant that forces the system to execute the signal samples procedure), T_s is set to zero and a signal level samples routine is executed and the results are stored into the signal level samples table. After this step the genetic controller estimates the duration time of each found route and the results are stored into the relative table.

If $T_s < T_{s0}$ no action is made.

After this step the routine goes back to the genetic rules optimization procedure.

At this point it is necessary to give some more information about the data transmission procedure (DTP).

The DTP is able to do two kinds of choices as a function of the temporal availability of the link. In fact, if the temporal need is already known when the link is created, the DTP forwards the communication on the proper link from the temporal point of view that is not necessarily the longer one to avoid of wasting network resources. If the transmission length is not known a priori, the DTP chooses the more lasting path, giving a high stability to the net.

These performances ensure a higher quality of communication, ensuring a significant reduction of band and energy waste.

The stability is also increased because the DTP checks continuously the strength of the signal: if this last one decreases below a minimum level between two nodes, the DTP seeks immediately a new path where to continue to route data, avoiding abrupt interruption of transmission.

We want now to describe the used fitness function. During the auction process, one or more rules can par-

ticipate to it. Each time a rule participates to a specific process of time estimation of a path, it is properly labelled with the number of process: one rule can participate to different processes and these information are stored in a proper label field of the rule. Once a temporal estimation of a path is requested to the system, the node check is continuously the real duration of the path, to use this information, in a second time during the GA phase, to select the most precise rules. When the GA phase is activated, every rules is properly assigned to a portion of the roulette wheel according to its precision in time duration estimation of the path it participated, to be eventually selected for the next generation population: the more precise the forecast of the rules and the higher the occupation space in the roulette wheel and consequently the higher the possibility to be selected for the next generation of population. The fitness of each rule is calculated in the following way: for every rule a proper check about the estimation processes it participated is made and the most precise forecast is selected, that is the rule is associated to the estimation process that differs, as less as possible from the temporal point of view, from the rules forecast. The fitness values of the rules are chosen to be variable between 10 (exact forecast) and 1 (totally wrong forecast). The value 1 has been chosen to allow also the wrong rules to evolve towards more fitting rules. This choice is very useful in the initial phase of the node, when only a few rules are used in the auction mechanism while are the other are momentarily in stand-by: since these last rules can be useful in the following phases, they must be characterized by a certain probability to pass to the next generation population of rules. If T_{pi} is the real duration time of the path i (in seconds) verified by the node and T_{rj} is the estimated time (in seconds) of the rule j (remembering that each rule is associated to different paths whose auction process it participated but it is associated, for the fitness evaluation, with the only path it better forecasted in term of duration of time), the fitness value F_j of the rules j is calculated as:

$$F_j=10 - ((abs\ (T_{pi} - T_{rj}))/T_{pi})*10 \quad (9)$$

It is evident that if the forecasted duration of time of rule j for the fitness is equal to the exact duration of path i T_{pi} , the fitness value F_j of the rules j is equal to 10. If F_j is lesser than 1, it is set by default equal to 1, to ensure a certain residual probability to the rule j to evolve in the next generation population of rules.

If a certain rule didn't participate any auction process, it is automatically rated with value 1. If a certain rule participated to one or more different auction processes but it is rated with a value lesser than 1, the fitness value is set to 1.

Once all the rules are properly rated, they are assigned a space proportional to their fitness value on a proper roulette wheel and the next population selection mechanism takes place.

Let's consider a practical numerical example whose parameters choice is generalized in Section 6.

In this case each node is considered to measure the mentioned signal every 30 second, as explained inSection 6.

A rule is based on 60 samples of signal taken every 30 seconds that is each rules express the history of 1800 seconds of the signal strength of the nodes.

The higher the number of samples of the rules and the higher the precision of the forecasted duration time of the link, as explained in Section 6.

The number of samples represents a compromise between precision and computation time of GC.

In the same way the shorter is the time between samples and the higher is the precision of the forecasted duration time of the link, as explained in Section 6.

The time interval between samples represent a compromise between precision and computation time of GC. The structure of the rule implemented on GC is shown in **Figure 4**.

The choice of the number of rules is quite critical since a reduced number (100 for example) ensures a rapid learning but a higher percentage of error while a great number (1500 for example) ensures a reduced percentage of error but a long learning time. The optimal number of classifiers in our case has resulted to be 800, as explained in Section 6.

In the next section the results obtained from the implementation of the considered protocol are illustrated while more general results are illustrated in Section 6.

5. Performances and Results

Before presenting the results obtained by the simulations, it is necessary to illustrate the condition under which they have been obtained.

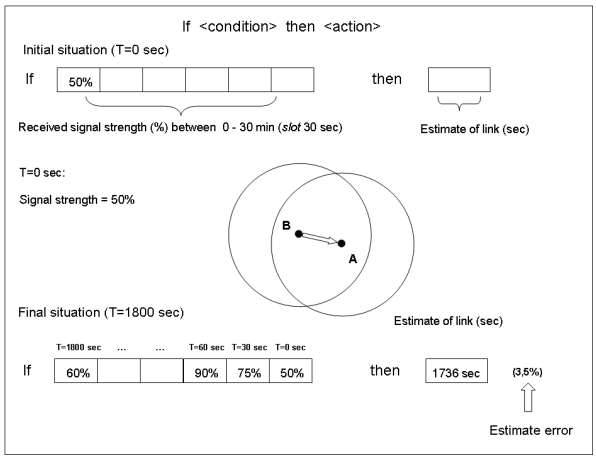

Figure 4. Structure of the rules.

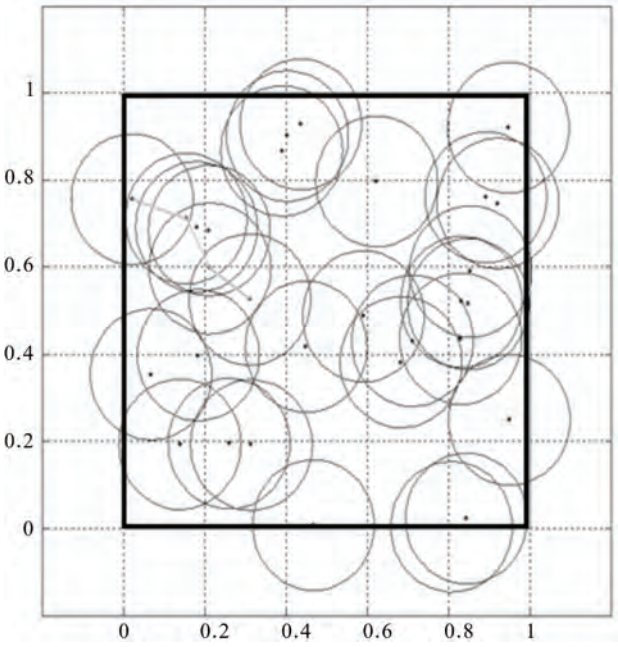

Figure 5. Example of network structure at the initial phase. distance are expressed in kilometers.

Simulations were made considering a 1000 m × 1000 m area with 40 moving nodes. Their movement is characterized by a velocity that varies instantaneously in modulus and phase, in a uniform way, between 0 - 10 [m/s] and 0 - 2 π (with step equal π/4 rad) respectively. Each node is characterized by a circle coverage ray equal to 150 m (**Figure 5**).

Two kinds of check were made: the first one aimed at verifying the robustness while the second one aimed at verifying the performances improvement with respect to a deterministic protocol.

5.1. Temporal Analysis of the Performances

In the first kind of check, 40 route discovery requests were made each time and the net is observed for almost 60 minutes. 6 particular check moments, corresponding to 10, 20, 30, 40, 50, 60 minutes are considered to verify the correctness of the choices made by the GC at 5, 10 15, 20, 25, 30 minutes from its activation

Since it is impossible to illustrate all the results, in the following only a restricted significant group of them is illustrated. In particular the better, the worst and the mean value of performances are illustrated.

A fundamental parameter is represented by the error between the estimated time of the link calculated the GC algorithm and the effective time of the link.

The first results are shown in **Figure 6**.

We can immediately see that the GC shows the expected behaviour. In particular the performances strictly improve with time, that is, the GC is capable of learning from the environment.

In fact at the first times, when the observation time is quite reduced, the GC makes not quite precise forecast that penalizes the choice of the correct path, as a deterministic protocol should do.

After a proper learning time, the GC is capable of making correct choices that strongly reduce the error.

It is possible to see that the difference between the better performance and the worst performance decreases with the time, due to the fact that each GC on the nodes has properly learned from the environment.

The proposed result do not consider the GCs that work correctly from the first time, since these results are considered as lucky circumstances not useful for our statistic.

In **Figure 7** the mean percentage error on all the simulations is shown. It is possible to see that the performance trend is lesser with respect to the mean between the worst performances and the better performances, showing that their distribution tend to be optimal since the mean error is lesser than 3.5%.

It is possible to see that the GC based algorithm is capable of selecting with a high precision and reduced error

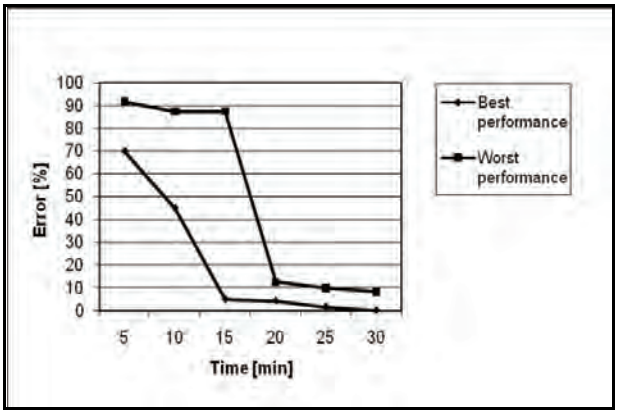

Figure 6. Mean error [%] – best and worst performance.

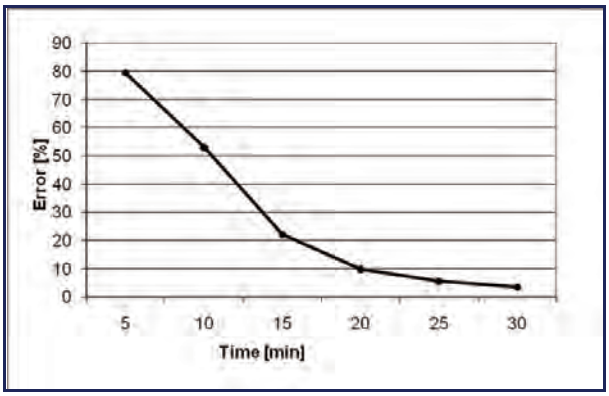

Figure 7. Mean error [%] – all simulations.

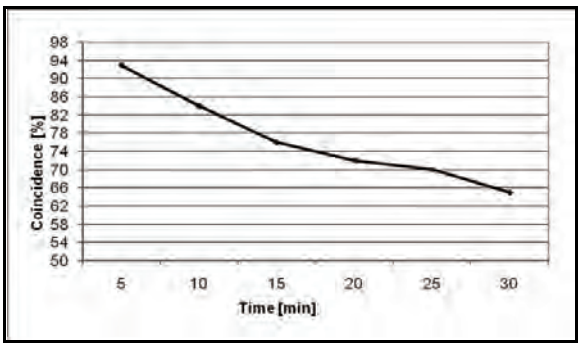

Figure 8. Comparison between ZRP and genetic based routing protocols.

the most reliable paths.

This growing precision about estimation of path durability influences strongly the performances of routing protocol in term of packet loss, overhead, per-packet energy and delay but the related results are not shown here for brevity.

In fact, the improvement with the time on estimation allows the choice of a reliable path, which increases with the experience acquisition of the Genetic Classifier, in reducing the losses caused by coverage loss.

5.2. Performance Comparison between Genetic- Based Routing Protocol and ZRP

The second kind of verify tends to evaluate the performances of the proposed protocol with respect to a deterministic protocol.

In order to achieve significant results we have compared our protocol with another hybrid protocol, the ZRP [14]: the two protocols have worked together on the same nodes, giving the possibility of comparing the results in the same situations.

The most important remark concerns the type of routing choice taken by protocols.

In **Figure 8** it is possible to see how the decision between the two protocols differs when the time increases.

In fact, at the beginning, their choice is in coincidence in the 93% of situations, to decrease, at the end, at only 65%.

This demonstrates the superiority of the proposed protocol after a certain working time since it is capable of reducing the prediction error to values lesser than 3.5%, making different choices with respect to the ZRP after a proper working time.

In particular, while the behaviour of the ZRP is obviously almost constant with the time, the performances of the genetic protocol improve with the time, overcoming those ones of the ZRP.

6. Generalization of the Proposed System

To demonstrate the high performances of the proposed

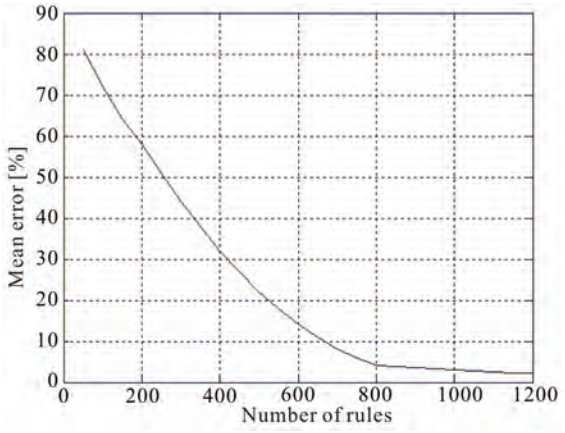

Figure 9. Mean error [%] as a function of the number of rules.

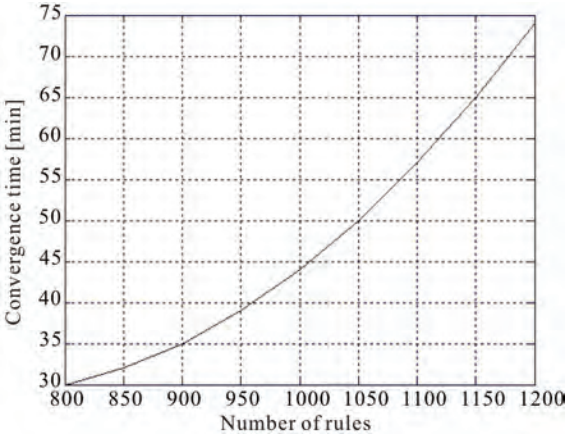

Figure 10. Convergence time [min] as a function of the number of rules.

system it is now necessary to generalize the obtained results. In this way it is also possible to understand the reason of the choice of the parameters used in the above simulation.

The first studied parameter is the number of rules. For this reason different simulations were made varying the number of rules and waiting for the final convergence, whose time increases with the number of rules, observing the mean error (in percentage), that is a significant parameter. The results are shown in **Figure 9**, where it is possible to see that the mean error decreases with the number of rules, reaching values lesser than 3.5% when the number of rules is greater than 800. When the number of rules is greater than 800, the reduction of mean error is less significant, assuming an asymptotic behaviour, while the converge time and the memory occupation increase as it is shown in the following. For this reason a number of rules of 800 has been chosen for the previous simulation.

Another important parameter is the convergence timeas a function of the number of rules. Results are shown in

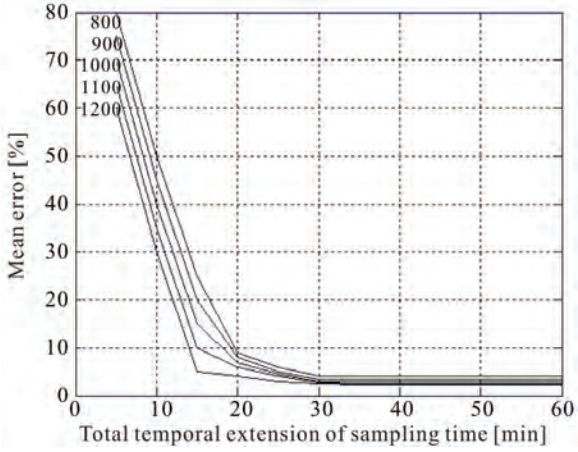

Figure 11. Mean error [%] as a function of the total temporal extension of sampling time [min], for different number of rules.

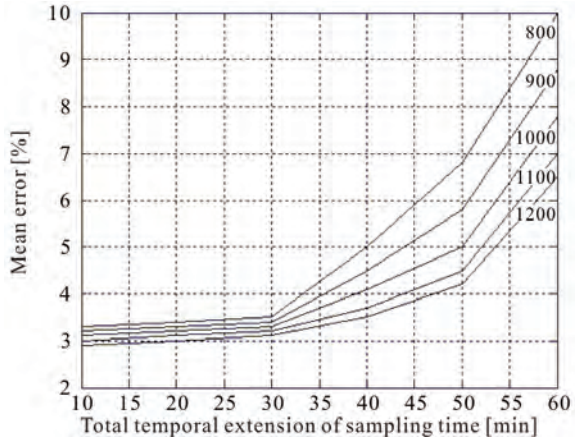

Figure 12. Mean error [%] as a function of the time interval between samples [sec], for different number of rules.

Figure 10, where it is possible to see that the convergence time increases with the number of rules, making the sys tem able to work correctly, with a non-significant mean error reduction, after a considerable learning time For this reason a number of rules of 800 has been chosen for the previous simulation, since it represents a good compromise between precision and convergence time.

To check the validity of the proposed system also the number of mobile nodes in the considered spatial grid has been increased (spatial density of nodes), controlling at the same time the possible variation of mean error as a function of rules. The obtained results (that are not shown here for brevity) are that the number of rules remains constant for each chosen mean error and spatial density of nodes, showing that it does not depend of this last parameter.

Another important parameter is the mean error (in percentage) as a function of the total temporal extension

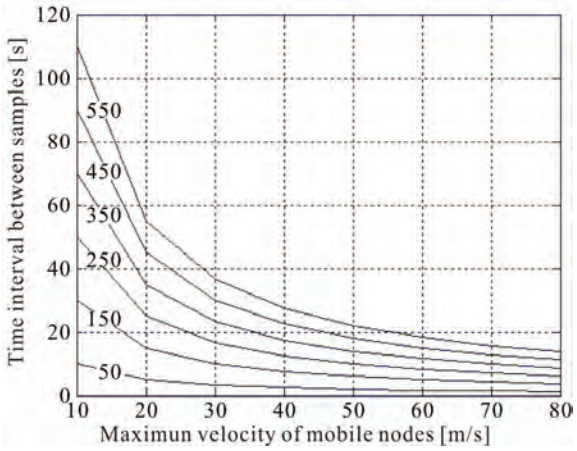

Figure 13. Time interval between samples [sec] as a function of the maximum velocity of mobile nodes [m/s], for different values of radius of coverage area [m].

of the sampling time (that in the previous simulation was 30 minutes). Results are shown in **Figure 11**, for different values of number of rules, where it is possible to see that the mean error decreases with the total temporal extension of the sampling time, making the system able to work correctly, with a mean error below 3.5%, after a learning time of 30 minutes.

For this reason a total temporal extension of the sampling time of 30 minutes for the previous simulation has been chosen, since it represents a good compromise between precision, memory occupation and convergence time.

Another important parameter is the mean error (in percentage) as a function of the time interval between samples (that in the previous simulation was 30 seconds).

Results are shown in **Figure 12**, for different values of number of rules, where it is possible to see that the mean error increases with the time interval between samples, making the system able to work correctly, with a mean error below 3.5%, if the time interval is lesser than 30 seconds for any number of rules. For this reason a total temporal extension of the sampling time of 30 seconds for the previous simulation has been chosen, since it represents a good compromise between precision, memory occupation and computation time.

It is now important to understand what happens when the maximum velocity of the mobile nodes increases (in the previous simulation it was of 10 m/s) or when the coverage area of the nodes varies (in the previous simulation the radius of the circular coverage area was of 150 m). Results are shown in **Figure 13**, for different value of coverage areas, for 800 rules and a mean error lesser than 3.5%, where it is possible to see that the more the maximum velocity increases and the more frequently the nodes

must be sampled. It is also possible to see that the larger the coverage area and the longer the time interval between samples, since the nodes are sampled in a more continuous way without leaving the wider coverage area. Since in previous simulation 800 rules are used, a coverage area of 150 meters is assumed and a maximum velocity of nodes of 10 m/s is considered, a time interval between samples equal to 30 seconds has been chosen.

All the results illustrated in this section allow to design, according to the specific needs, any kind of configuration that uses the proposed algorithm, as it was made in the simulation illustrated previously.

7. Conclusions

In the present work a high performance hybrid protocol based on genetic classifier was presented.

The obtained results, even if related to a quite simplified context, have shown a high robustness and a high improvement of reliability of the whole net, from the path temporal duration point of view, where the GC based protocol is operating.

REFERENCES

[1] K. Sundaresan, V. Anantharaman, H. Y. Hsieh and R. Sivakumar "ATP: A Reliable Transport Protocol for Ad Hoc Networks," *IEEE Transactions On Mobile Computing*, Vol. 4, No. 6, November/December 2005, pp. 588-603.

[2] D. Johnson, D. A. Maltz and J. Broch, "The Dynamic Source Routing Protocol for Mobile Ad Hoc Networks," MANET Working Group, IETF, Internet Draft, February 2002.

[3] C. E. Perkins and E. M. Royer, "Ad Hoc on-Demand Distance Vector (AODV) Routing," MANET Working Group. IETF, Internet Draft, November 2002.

[4] S. J. Lee and M. Gerla, "Split Multipath Routing with Maximally Disjoint Paths in Ad Hoc Networks," Proceedings of IEEE International Conference Communications, Helsinki, 2001, pp. 3201-3205.

[5] S. Corson and J. Macker, "Mobile Ad hoc Networking (MANET): Routing Protocol Performance Issues and Evaluation Considerations," Network Working Group, January 1999.

[6] Y. Yi, S. J. Lee, W. Su and M. Gerla, "On-Demand Multicast Routing Protocol (ODMRP) for Ad-Hoc Networks," IETF Internet Draft, http://www.ietf.org/internet-drafts/draft-ietf-manet-odmrp-04. txt.

[7] M. Gerla, X. Hong and G. Pei, "Landmark Routing Protocol (LANMAR) for Large Scale Ad Hoc Networks," IETF Internet Draft, http://www.ietf.org/internet-drafts/draft-ietf-manet-lanmar-05. txt

[8] A. Nasipuri, R. Burleson, B. Hughes and J .Roberts, "Performance of a Hybrid Routing Protocol for Mobile Ad Hoc Networks," *IEEE International Conference on Computer Communication and Networks*, (*ICCCN*2001), Phoenix, October 2001, pp. 432-439.

[9] N. Navid, W. Shiyi and C. Bonnet, "Hybrid Ad Hoc Routing Protocol (HARP)," *International Symposium on Telecommunications*, 2001.

[10] M. Abolhasan, T. Wysocki and E. Dutkiewicz, "A Review of Routing Protocols for Mobile Ad Hoc Networks," *Ad Hoc Networks Journal*, Vol. 2, No. 1, 2004, pp. 1-22.

[11] S. R. Das, R. Castaneda, J. Yan and R. Sengupta, "Comparative Performance Evaluation of Routing Protocols for Mobile Ad Hoc Networks" *Proceedings of IEEE* 7*th International Conference on Computer Communication and Networks*, Lafayette, October 1998, pp. 153-161.

[12] S. R. Das, C. E. Perkins and E. Royer, "Performance Comparison of Two On-Demand Routing Protocols for Ad Hoc Networks," *Proceedings of* 19*th Annual Joint Conference of IEEE Computer and Communications Societies* (*INFOCOM* 2000), Tel Aviv, March 2000, pp. 3-12.

[13] F. Mc Sherry, G. Miklau, D. Patterson and S. Swanson, "The Performance of Ad Hoc Networking Protocols in Highly Mobile Environments," Washington, Spring, 2000.

[14] Z. J. Haas, M. R. Pearlman and P. Samar, "The Zone Routing Protocol (ZRP) for Ad Hoc Networks," IETF Internet Draft, July 2002.

[15] Z. J. Haas, M. R. Pearlman and P. Samar, "Interzone Routing Protocol (IERP)," IETF Internet Draft, July 2002.

[16] L. Barolli, Y. Honma, A. Koyama, A. Durresi and J. Arai, "A Selective Bord-Casting Zone Routing Protocol for Ad Hoc Networks," *Proceedings of the* 15*th International Workshop on Database and Expert Systems Applications*, *IEEE*, 2004.

[17] Z. J. Haas and M. R. Pearlman, "The Performance of Query Control Schemes for the Zone Routing Protocol," *IEEE /ACM Transactions on Networking*, Vol. 9, No. 4, 2001, pp. 427-438.

[18] A. D. Mc Aulay and J. Chan Oh, "Improving Learning of Genetic Rule-Based Classifier System," *IEEE Transactions On Systems, Man, And Cybernetics*, Vol. 24. No. 1, January 1994, pp. 152-159.

[19] A. R. Pozo and M. Hasse, "A Genetic Classifier Tool," *Computer Science Society*, (*SCCC*'00), *Proceedings. XX International Conference of the Chilean*, 16-18 November 2000, pp. 14-23.

[20] C. Castillo, M. Lurgi and I. Martinez, "Chimps: An Evolutionary Reinforcement Learning Approach for Soccer Agents," *IEEE International Conference on Systems, Man and Cybernetics*, Vol. 1, 5-8 October 2003, pp. 60-65.

[21] B. Liu; B. McKay and H. A. Abbass, "Improving Genetic Classifiers with a Boosting Algorithm," *The Congress on Evolutionary Computation*, (*CEC*'03), Vol. 4, 8-12 December 2003, pp. 2596-2602.

[22] M. Minsky, "Computation: Finite and Infinite Machines," Prentice-Hall, New Jersey, 1967.

[23] E. L. Post, "Formal Reductions of the General Combinatorial Decision Problem," *American Journal of Mathematics*, Vol. 65, 1943, pp. 197-215.

[24] J. Holland, "Adaptation in Natural and Artificial System," University of Michigan Press, Michigan, 1975.

[25] D. E. Goldberg, "Genetic Algorithms in Search, Optimization & Machine Learning," John Holland, 1979.

[26] J. S. Pegon and M. W. Subbarao, "Simulation Framework for a Mobile Ad-Hoc Network," Wireless Communication Technology Group, 2004.

Wireless Engineering and Technology, **2010, 1, 81-87**
doi:10.4236/wet.2010.12012 Published Online October 2010 (http://www.scirp.org/journal/wet)

On the Design of Circular Fractal Antenna with U-Shape Slot in CPW-Feed

Raj Kumar, K. K. Sawant

Microwave and Millimeterwave Antenna Lab., Department of Electronics Engineering, Defence Institute of Advanced Technology (DU), Girinagar, India.
Email: omnamhshivay2010@gmail.com

Received July13th, 2010; revised August 4th, 2010; accepted August 24th, 2010.

ABSTRACT

A new ultawideband circular fractal antenna with notched-band characteristics is presented. A notched-band characteristic is achieved by employing a U-shape slot in 50 Ω *feed lines. The ultra-wideband impedance matching and compact size have been obtained by using CPW-feed technique and the fractal concept. The measured result of proposed fractal antenna exhibits the ultra wideband characteristics from* 3.0 *to* 18.0 *GHz at VSWR* 2:1 *except notched-band frequency. The proposed antenna has been analyzed theoretically and experimentally with respect to design parameters. The measured radiation pattern of fractal antenna is nearly omnidirectional in azimuth plane throughout the operating frequency. This antenna is useful for UBW communication system.*

Keywords*: *Monopole Antenna, Wideband Antenna, Resonant Frequency, Fractal Antennas, Multib, Antenna

1. Introduction

Ultra-wideband (UWB: 3.1-10.6 GHz) communication system has become more and more popular because of its advantages such as small size, high transmission rate, and low power consumption comparing with current wireless communication system [1]. Because of these advantages of an UWB system, significant research in the UWB antennas has been aroused in academic and industrial fields recently. However, over this allocated band, there are some existing narrow band services, such as IEEE 802.16 WiMAX system operating at GHz, and C-band satellite communication systems, which may cause electromagnetic interference to the UWB system. Thus, the UWB antenna with notched-band performance is required. The several UWB antennas with the notched frequency function have been reported [2-4], such as, attaching U-shaped slot, inverted U-slot, arc-shaped slot, C shaped slot, or small strip bar to the antenna. The UWB fractal antennas with notch have been reported for UWB applications [5-8]. In [5], Crown - Sierpinski microstrip antenna is proposed to reduce the size of a Crown square fractal. The frequency notched ultra-wideband microstrip slot antenna with a fractal tuning stub is proposed to achieve frequency notched function [6-7]. Raj Kumar *et al*. [8-9] have proposed a new UWB fractal antenna by adopting the fractal concept on the CPW-fed circular UWB antenna. This work proposed the UWB fractal antenna band-notched characteristics with detail study.

In this paper, a new circular fractal antenna with band-notched is proposed for the UWB system applications. The notched band is easy to tune by changing the length and width of the slot. The antenna has advantages of compact size, low manufacturing cost, easy fabrication, low profile, and very small ground plane suitable for integration with compact UWB systems. The performance of the proposed antenna is characterized in term of impedance bandwidth, band-notched and radiation pattern.

2. Antenna Geometry and U-Shape Slot

The iteration wise fractal antenna was constructed from simple conventional monopole antenna as shown in **Figure 1**. The solid circular monopole antenna has been designed on FR4 substrate ε_r = 4.3, h = 1.53 mm, with radius 9.1 mm. This is called the initiator or zeroth iteration shown in **Figure 1(a)**. The first iteration of fractal antenna has been constructed by inscribing the square patch of dimension 12.8 × 12.8 mm inside the circle and subtracted it from circle. This is called 1st iterative inscribed square circular fractal antenna as shown in **Fig-**

ure 1(b). The 2nd iteration has been achieved by making the circle of diameter 12.8 mm and an inscribed square of dimension 9.05 × 9.05 mm has been subtracted from this inner one circle as shown in **Figure 1(c)**. The 3rd iteration is constructed by making the metallic circle of 9.05 mm diameter inside the square touching the metallic part of its and subtracting an inscribed square of dimension 6.4 × 6.4 mm as shown in **Figure 1(d)**. In the fourth iteration, a circle of diameter 6.4 mm is made and an inscribed square of dimension 4.525 mm × 4.525 mm is subtracted as shown in **Figure 1(e)**. This process can be repeated up to infinite iteration. Practically infinite iterative structure is not possible because of fabrication constraints. The fourth iterative fractal antenna has been finalized to design on the same substrate dielectric constant and thickness as conventional microstrip monopole antenna as shown in **Figure 1**. This antenna has been fed with the coplanar feed. The CPW-Fed and radiating elements both are printed on the top side of a low-cost FR-4 substrate with dielectric constant ε_r = 4.3, h = 1.53 mm and loss tangent tan δ = 0.02.

Figure 1 shows the geometry of the proposed fractal antenna. It is composed of inscribed square circular fractal radiating elements, fed by a U-shape slotted CPW-feed with a very small ground plane. There is no ground plane at the bottom of the substrate. It is known that CPW-feed is advantageous for less dispersion at higher frequency, broader matching, easy fabrication and integration with MIC/MMIC. The CPW-fed antenna not only performs better in respect of bandwidth and but radiation pattern is also good [8]. In coplanar feed, the feed of antenna and radiating elements are printed on the same side of the substrate. A slot is inserted of U-shape in 50 Ω feed line of coplanar waveguide to create the notched frequency band. The resonant frequency of the notched band is defined by the effective length of the slot and band-notched frequencies by width of the slot. It can be seen by changing the L and W, notched-band frequencies can be controlled. The notched frequency bandwidth is controlled by varying the width of slot, while notched-band resonant frequency can be controlled by changing the length of slot. To validate the design the band-notched at frequency from 3.635 to 3.935 GHz, the slot length of 10 mm and width 0.4 mm have been taken which can be redesign according to the requirement. A parameter studies with respect to slot width and length have been done.

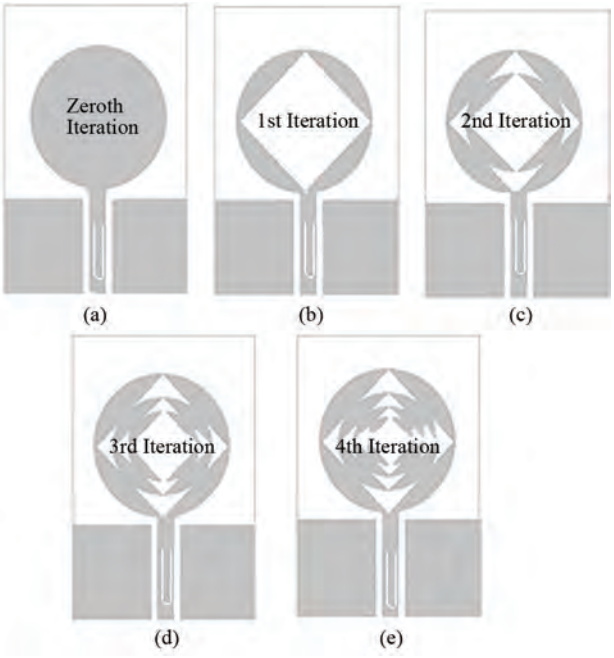

Figure 1. Inscribed square circular fractal antenna with various iteration.

3. Fractal Geometry for Compact Size and UWB

A simple circular disc monopole antenna with slotted CPW-fed is shown in **Figure 1(a)**. It is understood that current distribution of the proposed antenna is mainly along the circumference of the circular disc. The current density is low in the middle area of the solid circular disc monopole antenna as shown in **Figure 2**. Therefore, the current will not be affected if the middle area of the solid circular disc monopole antenna is removed. In this way, the effective path of the surface current will become longer. In this antenna, the effective length of current path is increased by inscribing square in solid circular disc. This resulted, the first resonance frequency will be decreased and the size of the antenna will be reduced.

To achieve the UWB characteristic, the fractal structure can be added to increase the resonance frequency in

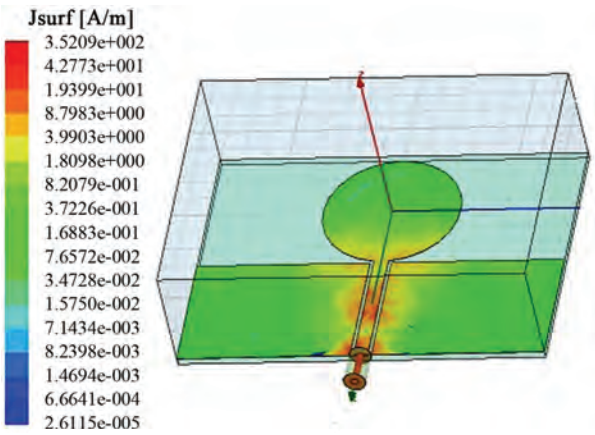

Figure 2. Current distribution on the circular disc monopole Antenna.

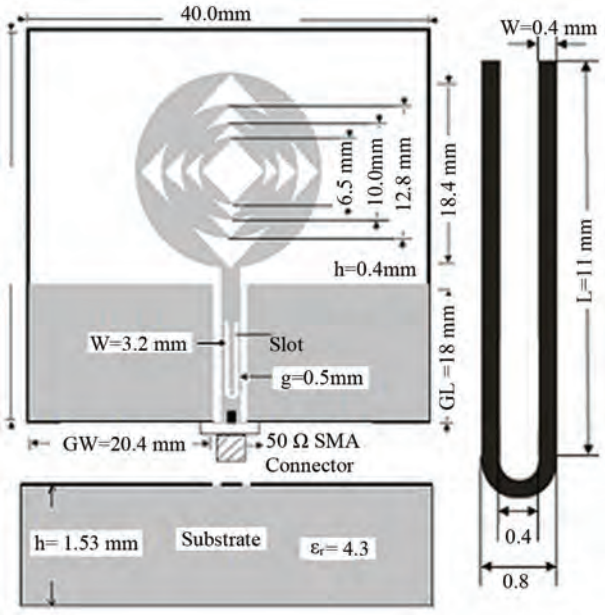

Figure 3. Proposed circular fractal antenna with slot dimension.

high frequencies by adding resonance elements in solid circular disc antenna. In this paper, resonance elements have been added by inscribing square in various concentric circles as shown in **Figure 1**. The proposed fractal antenna structure has been shown in **Figure 3** with slotted CPW-fed. The 50 Ω impedance is achieved by adjusting the width W = 3.2 mm of the inner conductor and the gap between the ground plane and feed width is g = 0.5 mm. To achieve the UWB characteristic, the gap between patch and ground has been optimized to h = 0.4 mm. The length of ground plane GL = 18 mm and width of the ground plane 20.4 mm have been optimized.

4. Simulated Results

It is noticed in simulation that the operating bandwidth of the proposed antenna is heavily dependent on the gap between patch and ground, iteration number and notched-band depends on length of slot and width of slot. The UWB characteristic depends upon the parameters gap between patch and ground, and iteration number. But notched-band characteristic depends upon the length and witch of the slot. First the parameters for maximum bandwidth have been optimized with fixed slot dimension. The antenna has been simulated for each iteration. The simulated result of each iteration is shown in **Figure 4**.

It is clear from the **Figure 4**, as the iteration increase the first resonant frequency shifted towards lower frequency side. This shift indicates the size reduction of the antenna. It is also found that as the number of iteration increases, the lower-edge of the impedance bandwidth is

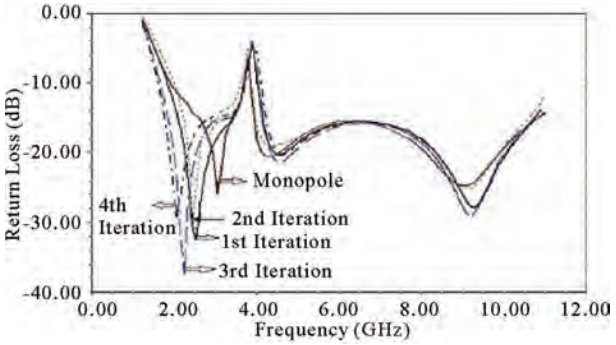

Figure 4. Simulated result of fourth iterative fractal antenna with respect to various iteration.

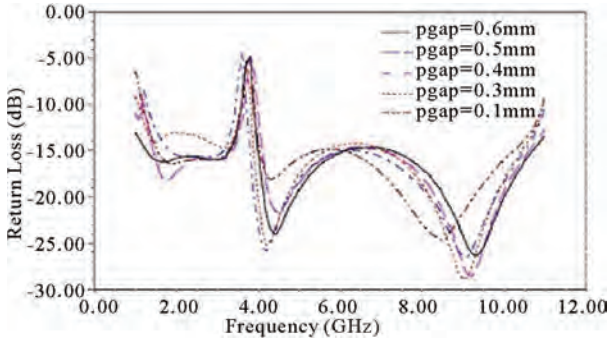

Figure 5. Simulated result of fourth iterative fractal antenna for various value of gap between patch and ground.

moved to the low frequency and the level of the impedance matching over the operating frequency band is improved. The fourth iterative fractal antenna gives the impedance matching in UWB characteristic.

From **Figure 2**, it can be seen that current is mainly distributed on the upper edge of ground plane and along the edge of antenna disc, which explains why the performance of the antenna is critically dependent on the gap h between ground and patch. The parameter h is very critical parameter for proper coupling from feed line to patch which effect the UWB characteristic. The proposed fractal monopole antenna has been simulated for various values of gap. The simulated results have been shown in **Figure 5**. It has been observed from graph that gap (h) between ground and patch effects the lower end frequency and bandwidth. The fourth iterative proposed fractal antenna has been fabricated with gap h = 0.4 mm, 50 Ω feed with W = 3.2 mm and g = 0.5 mm.

5. Notched-Band Characteristic

The effect of these design parameters on UWB characteristics and band-notched characteristics are because of current distribution over radiating elements, ground plane, feed line and U-type slot. **Figure 6** shows the current distributions at 3.2 GHz and 3.8 GHz frequency for

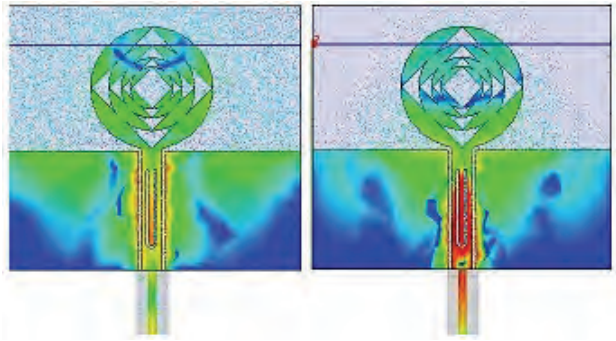

3.2 GHz (a) 3.8 GHz (b)

Figure 6. Current distribution over slot at notched and without notched frequency.

the optimal design parameters. In **Figure 6(a)**, where the antenna operates at pass band frequencies 3.2 GHz, there is more current distributions near the feeding point (*i.e.*, slot does not resonate and has little effect). At notch frequency, 3.8 GHz, as shown in **Figure 6(b)**, current is concentrated around the edge of the slot while there is almost no current at the feeding point.

It reveals that the currents mainly concentrate around the slots at the notched frequency, which indicates the width/length/position of slots can actually play significant roles in the performance of the band-notched characteristics of proposed antenna. This leads to the desired high attenuation and impedance mismatching around the notch frequency. This demonstrates the notch-band function of the antenna and therefore elimination of interfering signals within the UWB spectrum.

As it can be seen the proposed antenna provides UWB characteristics with band-notched frequencies. The band-notched frequency happens at 3.635 to 3.935 GHz for filtering the interfering signal. It can be seen by changing the length (L) and Width (W), resonant frequency and band-notched can be tuned. The resonant frequency of the notched-band depends on the length of the slot and notched bandwidth depends upon width of the slot. It is clear as length of slot increases, the band-notched resonant frequency shifts to the lower side. As the length of slot increases from 3 mm to 13 mm, the resonant frequency of band-notched shifts to lower frequency side is shown in **Figure 7**.

The width of band-notched can be tuned by varying the slot width. As the slot width increases from 0.2 mm to 0.8 mm, the notched bandwidth increases as shown in **Figure 8**. It is observed from the simulated result as the slot width (for fix length) increase from 0.2 mm to 0.8 mm the notched bandwidth increases more the double with the better notched characteristic. To validate the design, the prototype fractal antenna has been fabricated

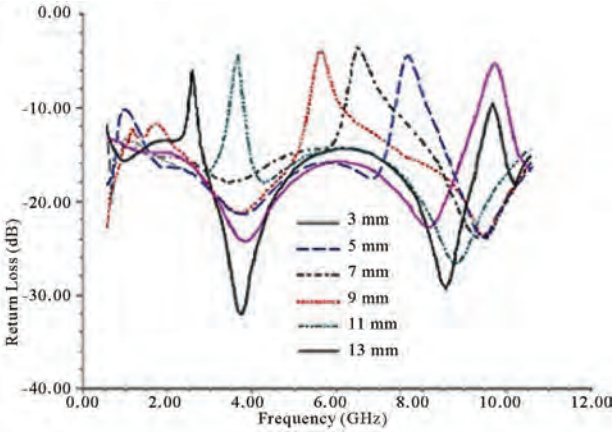

Figure 7. Simulated result of fourth iterative fractal antenna notch for various length of slot.

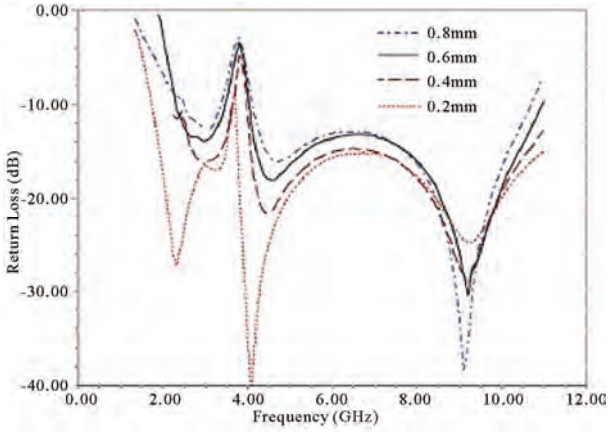

Figure 8. Simulated result of fourth iterative fractal antenna notch for various width of slot.

with slot length of 10 mm and width 0.4 mm.

6. Experimental Results

The proposed fractal antenna with U-type slot has been fabricated with optimized dimension 9.1 mm radius on substrate $\varepsilon_r = 4.3$, thickness 1.53 mm, GL = 18 mm, GW = 20.4 mm h = 0.4 mm, g = 0.5 mm, slot width = 0.4 mm and slot length 11 mm. The photograph of the proposed fractal antenna is shown in **Figure 9**. The simulated results of proposed fractal antenna with and without slot are shown in **Figure 10**. The antennas have been tested using vector network analyzer R&S ZVA 40. The experimental results of proposed fractal antenna without slot acquired from the Vector Network Analyzer exhibits the excellent ultra wide impedance bandwidth of 11.99 GHz (from 3.01 GHz to 15 GHz) corresponds to 132.49% impedance bandwidth for VSWR 2:1. The measured return loss versus frequency of this fractal antenna has been shown in **Figure 11**.

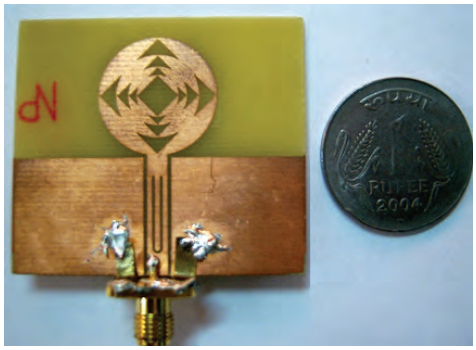

Figure 9. Photograph of the proposed antenna.

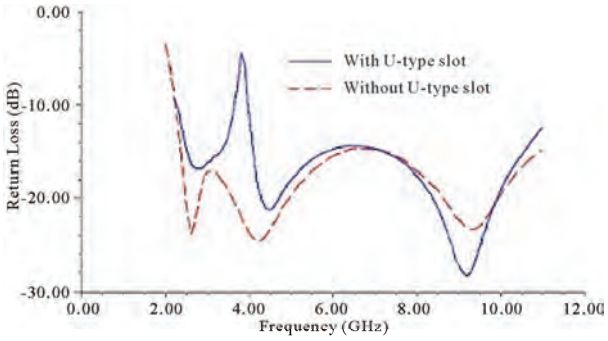

Figure 10. Simulated result with and without U-type slot.

The experimental result of circular fractal antenna with slot exhibits the UWB characteristic from 3.01 to 15 GHz except band-notched frequencies from 3.635 to 3.935 GHz. The return loss and VSWR versus frequency of this fractal antenna with band-notched have been shown in **Figure 12** and **Figure 13** respectively. It is observed that return loss is better at higher frequency in comparison to the return loss without notched-band. It is observed that simulated and measured results are slightly varies. This may be due to the tolerance in manufacturing, uncertainty of the thickness and/or the dielectric constant and lower quality of SMA connector (VSWR = 1.3). The differences between simulated and experimental value may also be caused by the soldering effects of an SMA connector, which have been neglected in our simulations.

7. Experimental Radiation Patterns

Radiation characteristics of the circular fractal antenna at operating frequency within the impedance bandwidth have also been studied. The measured radiation pattern in azimuth plane (H-plane) have been calculated at selective frequencies 4.2 GHz, 5.1 GHz, 6.0 GHz, 6.0 GHz and 7.2 GHz as shown in **Figure 14**. The radiation pattern in E-plane has also been measured at various selective frequencies 4.11 GHz, 5,025 GHz, 6.0 GHz and 7.05 GHz as shown in **Figure 15**. The H-plane radiation

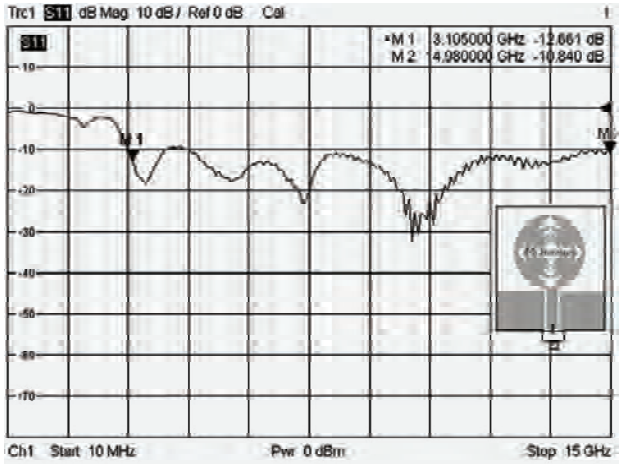

Figure 11. Experimental results proposed fractal antenna without U-type slot.

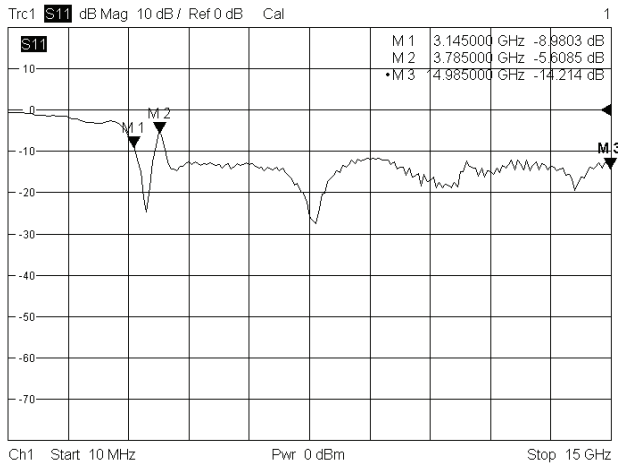

Figure 12. Experimental return loss versus frequency of fractal antenna with U-type slot.

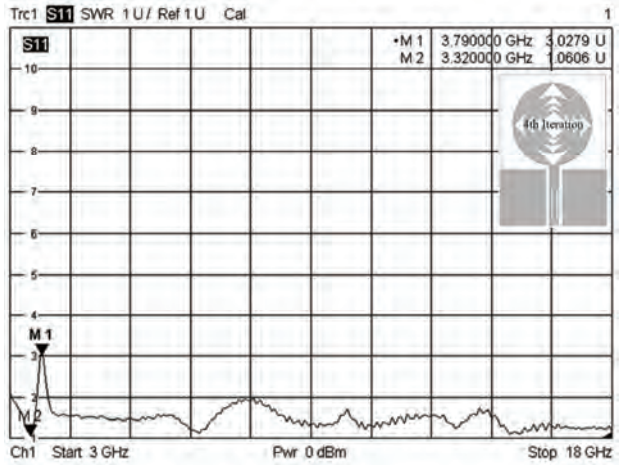

Figure 13. Experimental VSWR of circular fractal antenna with U-type slot.

patterns are almost omnidirectional, and the E-plane radiation patterns are like monopole radiation. It can be seen that the patterns of the proposed antenna are stable over the operating frequency range.

The proposed antenna gain in operating band meets the requirement for FCC defined UWB frequency band from 3.1 GHz to 10.6 GHz. It has been observed cross to copolarization ratio reduces at higher frequency. It has been observed that antenna gain is less than 5dBi in frequency range 3.1 GHz to 10.6 GHz. The gain drops significantly around −4.01 dBi at the band-notched resonant frequency as shown in **Table 1**. Such type of antenna is very useful for UWB communication system.

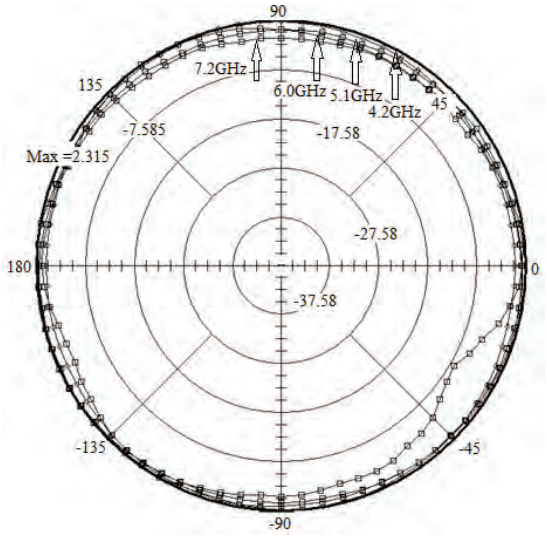

Figure 14. H-Plane Radiation Pattern of proposed fractal antenna at frequencies 4.2, 5.1, 6.0 and 7.2 GHz.

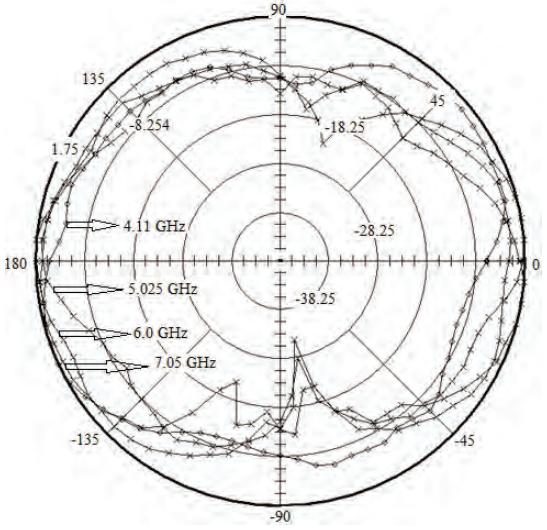

Figure 15. E-Plane Radiation Pattern of proposed fractal antenna at frequencies 4.11, 5.025, 6.0 and 7.05 GHz.

Table 1. Frequency versus gain (dBi).

Frequency (GHz)	Gain (dBi)
3.1	1.02
3.8	−4.01
4.0	1.75
8.078	3.78

8. Conclusions

In this paper, a new CPW-Fed circular fractal antenna has been proposed with band-notched frequencies. Notched band is achieved to minimize the potential interference from external signals by introducing an U-shaped slot in 50 Ω feed line. The proposed monopole antenna has a wide operating frequency band of 3.01 GHz to over 15 GHz (VSWR < 2). It is observed that the radiation patterns of antenna in H-plane is omni-directional and E-plane is dipole-like radiation pattern over the entire operating bandwidth The proposed fractal antenna design is compact, low profile, and offers very large impedance bandwidth required for next generation UWB system. The use of coplanar ground plane makes the design conformal and more suitable for the miniaturized applications. Parametric studies are also presented to show the effects of different parameters on the antenna design. The measurement results have shown a good agreement with the simulation ones. Such type of antenna can be useful for UWB system as well as suitable for various military and commercial wideband applications.

9. Acknowledgements

The authors sincerely thanks to Vice Chancellor, Pro-Vice Chancellor, Dean, DIAT, Pune and for constant encouragement and support. Authors are thankful to all the research scholar of Microwave and Millimeter wave Antenna Lab and staff of for their support directly or indirectly.

REFERENCES

[1] G. R. Aiello and G. D. Rogerson, "Ultra-Wideband Wireless Systems," *IEEE Microwave Magazine*, Vol. 4, No. 10, June 2003, pp. 36-47.

[2] H. J. Zhou, B. H. Sun, Q. Z. Liu, and J. Y. Deng, "Implementation and Investigation of U-Shaped Aperture UWB Antenna with Dual Band Notched Characteristics," *Electronics Letters*, Vol. 44, No. 24, 2008, pp. 1387-1388.

[3] T.-P. Vuong, A. Ghiotto and Y. Duroc, "Design and Characteristics of a Small U-Slotted Planar Antenna for IR-UWB," *Microwave and Optical Technology Letters*, Vol. 49, No. 7, 2007, pp. 1727-1731.

[4] R. Zaker, C. Ghobadi and J. Nourinia, "Novel Modified UWB Planar Monopole Antenna with Variable Frequency Band-Notch Function," *IEEE Antennas and Wire-*

less Propagation Letters, Vol. 7, 2008, pp. 112-114.

[5] P. Dehkhod and A. Tavakoli, "A Crown Square Microstrip Fractal Antenna," *IEEE Antennas and Propagation Society International Symposium*, Vol. 3, 2004, pp. 2396-2399.

[6] V. J. Lui, C. H. Cheng, Y. Cheng and H. Zhu, "Frequency Notched Ultra-Wideband Microstrip Slot Antenna with Fractal Tuning Stub," *Electronics Letters*, Vol. 41, No. 24, 2005, pp. 294-296.

[7] W. J. Lui, C. H. Cheng and H. B. Zhu, "Compact Frequency Notched Ultra-Wideband Fractal Printed Slot Antenna," *IEEE Microwave and Wireless Components Letters*, Vol. 16, No. 4, 2006, pp. 224-226.

[8] R. Kumar and P. Malathi, "On the Design of CPW-Fed Ultra Wideband Triangular Wheel Shape Fractal Antenna," *International Journal of Microwave and Optical Technology*, Vol. 5, No. 2, March 2010, pp. 89-93.

[9] R. Kumar and P. Malathi, "Design of CPW-Fed Ultra Wideband Fractal Antenna and Backscattering Reduction," *Journal of Microwaves, Optoelectronics and Electromagnetics Applications*, Vol. 9, No. 1, June 2010, pp. 10-19.

Wireless Engineering and Technology, **2010, 1, 88-91**
doi:10.4236/wet.2010.12013 Published Online October 2010 (http://www.scirp.org/journal/wet)

Scientific Research

Interference Mitigation in Satellite Personal Communication Networks Using Adaptive Antenna Arrays and Filtering Technique

Sunday E. Iwasokun[1], Michael O. Kolawole[2]

[1]Department of Electrical and Electronics Engineering, School of Engineering and Engineering Technology, Federal University of Technology, Akure, Nigeria.
Email: {wasokunday, kolawolm}@yahoo.com

Received April 27th, 2010; revised August 3rd, 2010; accepted August 4th, 2010.

ABSTRACT

We address the problem of interference as related to Satellite Personal Communication Networks (*S-PCNs*). *Basic low Earth orbit* (*LEO*) *constellation is considered. The paper uses combined adaptive antenna arrays and adaptive filtering technique. This hybrid linear adaptive technique provides improved performance eliminating interference, particularly uncorrelated signals residing in the antenna sidelobes.*

Keywords*: *S-PCN, LEO, Adaptive Array Antennas, Adaptive Filtering, Interference Elimination

1. Introduction

A Satellite personal communication network (S-PCN) provides universal access to a wide range of services and across transnational boundaries. It faces multitude of challenges particularly those related to user terminals, the space segment, regulatory challenges, [1], as well as technical issues including link diversity, traffic allocation [2], quality of desired service (QoS) and the associated grade of service (GoS) [3], etc. The interference encroachment into the signals received by systems terminals impacts on the QoS and GoS as well, and importantly the network congruous scope to deal with the motion of the satellite as well as that of the mobile user [4]. Most mobile stations' transceivers signals are ideally circularly polarized and isotropic in nature, with a single low gain antenna element. However, these single element units are particularly more susceptible to noise interference because they receive signals from all directions. Mounting adaptive antenna arrays on the mobile unit is an approach suitable to combating interference problem as communication satellite traverses the sky, which this study attempts to investigate. Of particular concern is the interference on voice channels causing crosstalk; e.g. where the subscriber hears interference in the background. **Figure 1** demonstrates an S-PCN user affected by random, multidimensional interferences.

2. Array Geometry

An adaptive array antenna unit is designed, as in **Figure 2**, bringing all the signals received by the various elements from a particular source into phase for further processing, as well as achieving some desired performance, such as maximizing the received signal-to-noise ratio (SNR). Drawing from [5] and [6], we analyse the antenna array assuming that 1) there is a direct path for the signal from the satellite and interfering signal is uncorrelated with the desired signal, 2) all the array elements are placed closely enough such that there is no significant amplitude

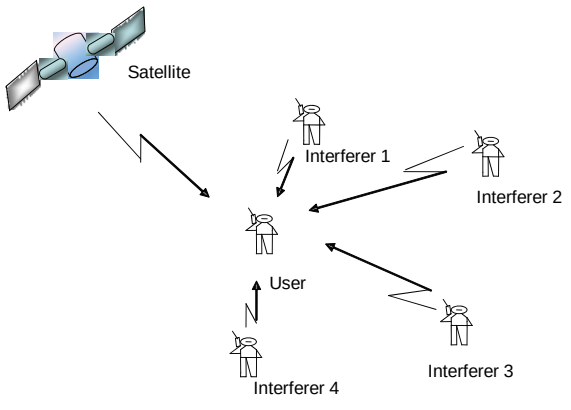

Figure 1. PCN mobile user affected by interference.

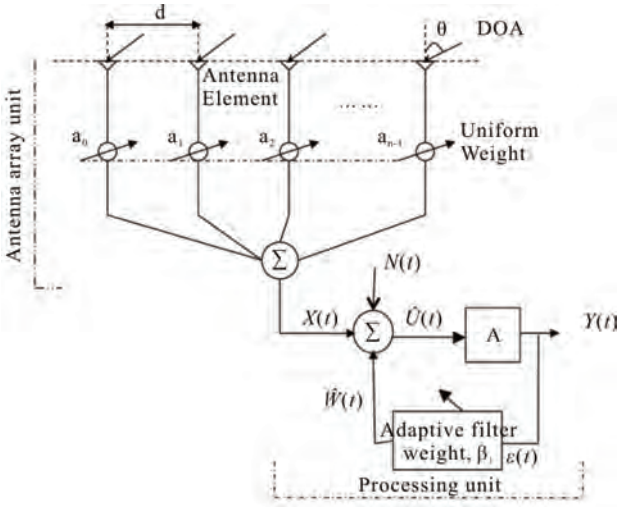

Figure 2. An adaptive antenna and adaptive filter for S-PCN mobile terminal.

variation due to the difference in propagation path length for any two elements, and 3) there is no significant difference in θ - the direction-of-arrival (DOA) - of a particular plane wave at any two elements.

For N elements array of identical characteristics, the first pulse is taken as the phase centre, $f(\tau)$. The second pulse is advanced by τ and denoted by $f(t-\tau)$, the third pulse is advanced by 2τ and denoted by $f(t-2\tau)$, and so on. For convenience, five elements are used, so

$$f_T(t) = a_o f(t) + a_1 f(t-\tau) + a_2 f(t-2\tau) + a_3 f(t-3\tau) + a_4 f(t-4\tau) \quad (1)$$

where $a_0, a_1 \ldots a_5$ are the weights/gains of each element of the array. In adaptive antenna array, the weights/gains of each element are taken to be the same (*i.e.*, $a_0 = a_1 = ... = a_4$), conforming to practical situation, and the elements to be equally spaced. Had the weights variable, there is possibility they may modulate the desired signal. Now, if the first pulse is Fourier transformed and is represented by $f_\Delta(\omega)$, then

$$f_T(\omega) = a_0 f_\Delta(\omega) + a_1 f_\Delta(\omega) e^{-j\omega\tau} + a_2 f_\Delta(\omega) e^{-j2\omega\tau} + a_3 f_\Delta(\omega) e^{-j3\omega\tau} + a_4 f_\Delta(\omega) e^{-j4\omega\tau} \quad (2)$$

By multiplying (2) by $e^{-j\omega\tau}$ and then subtracting the resulting expression from (1), and rearranging ensuing expression and using known geometric series expansion we have

$$f_\tau(\omega) = a_0 f_\Delta(\omega) \left[e^{-j2\omega\tau} \left(\frac{\sin(5\pi f\tau)}{\sin(\pi f\tau)} \right) \right] \quad (3)$$

Typical S-PCN frequencies of 1.376 and 1.80 GHz [6,7] are used to examine the antenna array's behaviour using (3). Resulting graphs are shown in **Figure 3**. The sidelobes performance has an important impact on interference received from adjacent satellites (and ground based signals operating on same bands), as well as in determining antenna noise temperature. To successfully eliminate, or reduce significantly, the effect of external interference, the sidelobes have to be attenuated, if not removed. The sidelobes are cancelled or removed in this paper by the adaptive array process.

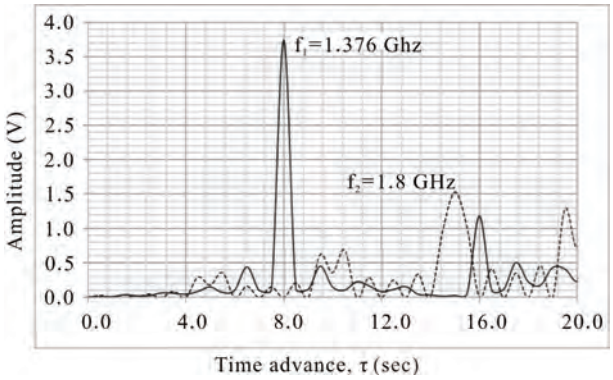

Figure 3. Antenna array's response at typical S-PCN frequencies.

3. Processing Unit: Modelling Interference with Adaptive Filter

Our approach models the effect of interferers on the S-PCN systems using interferences as recursive random processes, $N_i(t)$ with the array antenna. The input to the processor in **Figure 2** is the inverse Fourier $\Im^{-1}[f_\tau(\omega)]$ of the array output, which now becomes *X(t)* to the summer. The effect of noise from each antenna element is factored in at the output; that is, for *n* elements with equal average signal-to-noise (SNR), the average SNR of the array combiner is $10\log_{10}(n)$, which is higher in dB than the average SNR of any one of the elements [8].

Following **Figure 2**, the recursive-filtering algorithm can be represented as a linear, discrete-time (t) model of the form:

$$\hat{U}(t) = X(t) + N(t) - \hat{W}(t) \quad (4)$$

$$Y(t) = A\hat{U}(t) \quad (5)$$

where $A(t)$ is the system parameter; $\hat{W}(t)$ is optimum adaptive but weighted filter and $N(t)$ is additive, uncorrelated system interference, assumed white, zero-mean Gaussian and stochastic; and *Y*(*t*) filter (or measurement) output. The optimum interference $\hat{W}(t)$ is defined as

$$\hat{W}(t) = \sum_{i=0}^{k} \beta_i(t) N_{th}(t-i) \quad (6)$$

where N_{th} is the acceptable interference threshold, and *k* is the filter order. The proceeding coefficient of the filter

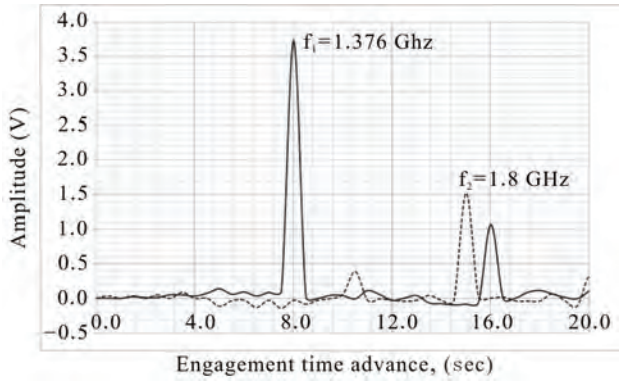

Figure 4. Simulated received response of mobile terminal at typical S-PCN frequencies.

can be estimated from the present coefficient and other thresholds:

$$\beta_i(t+1) = \beta_i(t) + 2\eta X(t) N_{th}(t-i) \tag{7}$$

where η is the convergence constant.

The adaptive filter adapts the filter coefficients to achieve desired signal ensuring convergence; that is, minimizing error $\varepsilon(t)$ at each time index:

$$\varepsilon(t) = Y(t) - A\hat{U}(t) \tag{8}$$

Ensuring fast convergence a local minimum is sought leading to establishing threshold value; *i.e.*,

$$\xi(t) = \sum_{j=0}^{k} \left| \beta_t(j) - \beta_{t-1}(j) \right| \le \alpha_{th} \tag{9}$$

where α_{th} local minimum threshold. The adaptation gain $g(m)$ is introduced for coefficient updating recursion for the period of the signal measurement:

$$g(m) = \left| \sum_{i=0}^{m} \frac{\hat{U}(i)}{X(i) + N(i)} \right| \tag{10}$$

where *m* is the period which the mobile terminal engages the network.

As shown in **Figure 4**, application of adaptive filter in conjunction with the antenna array processing shows encouraging responses in terms of interference reduction.

The implication of our method is that the variation of the filter's weights, as a result of movement of the mobile users, may affect the effectiveness of the system as the satellites move from orbit to another; low earth orbit (LEO) through to geostationary orbit (GEO), for example [9]. However, a mobile user of any of the systems might experience the same problem since the environment is changing too rapidly for the weights to converge. This is an area that is being investigated. Also, the relative motion between the user and the satellite reference may be another source of error resulting in Doppler shift. Recent work of [10] suggests that using frequency lock loop could compensate for this error. Whilst our technique has utilised uniform weight for the antenna array, this should not a problem if variable weights were to be utilised [11]. Moreover, since some of the satellite constellations utilize *code division multiple access* (CDMA) as the multiple access technique, pseudorandom noise codes can also be utilized to monitor the adaptive array weights.

4. Conclusions

We have presented an antenna-array plus adaptive filtering model as a way of eliminating the effect of interference in satellite personal communication systems. This technique has shown that it can eliminate an uncorrelated signals residing in the antenna sidelobes successfully. This technique is easily adaptable to S-PCN in LEO operational environment as a result of shorter time required by LEO satellites to move across the sky.

REFERENCES

[1] L. Ghedia, "Satellite Personal Communication Networks," In: B. G. Evans, Ed., *Satellite Communication Systems*, Institution of Electrical Engineers, 1999.

[2] R. Septiawan, "Multiservice Traffic Allocation in LEO Satellite Communications," Ph.D. Dissertation, Bond University, Gold Coast, 2004.

[3] R. Conte, "Satellite Rural Communications: Telephony and Narrowband Networks," *International Journal of Satellite Communications and Networking*, Vol. 23, No. 2, 2005, pp. 307-321.

[4] M. O. Kolawole, "A Course in Telecommunication Engineering," S Chand, New Delhi, 2009.

[5] M. I. Skolnik, "Introduction to Radar Systems," McGraw-Hill, Singapore, 1981.

[6] M. O. Kolawole, "Radar Systems, Peak Detection and Tracking," Elsevier, Oxford, 2003.

[7] E. Lutz, "Issues in Satellite Personal Communication Systems," *Wireless Networks*, Vol. 4, No. 2, 1998, pp. 109-124.

[8] M. A. Ingram, R. Romanofsky, R. Q. Lee, F. Miranda, Z. Popovic, J. Langley, W. C. Barott, M. U. Ahmed and D. Mandi, "Optimizing Satellite Communications with Adaptive and Phased Array Antennas," *Earth Science and Technology Conference*, Crowne Plaza, 2004, pp. 1-7.

[9] S. E. Iwasokun and M. O. Kolawole, "Using Hybrid Adaptive Techniques to Reduce Multipath Effects in S-PCN Mobile Terminals," *International Journals of Communications, Network and System Sciences*, 2010 (In press).

[10] M. Rao, L. L. Presti, M. Fantino and G. Garbo, "A Soft-

ware Receiver Adaptive Phase Lock Loop Method," *International Global Navigation Satellite Systems Society* (*IGNSS*) *Symposium*, Sydney, December 2009, pp. 1-13.

[11] S. E. Iwasokun, "Elimination of Interference and Multipath Signals in Satellite Personal Communication Systems Using Adaptive Antenna Array," M. Eng. Thesis, Federal University of Technology, Akure, 2010.

Wireless Engineering and Technology, **2010, 1, 92-95**
doi:10.4236/wet.2010.12014 Published Online October 2010 (http://www.scirp.org/journal/wet)

Rain Attenuation at Terahertz

S. Ishii[1], S. Sayama[1], K. Mizutani[2]

[1]Department of Communications Engineering, National Defense Academy, Yokosuka, Japan; [2]Department of Intelligent Interaction Technology, University of Tsukuba, Tsukuba, Japan.
Email:

Received July 30th, 2010; revised September 20th, 2010; accepted September 27th, 2010.

ABSTRACT

Rain attenuation values were calculated using empirical raindrop-size distributions, which were, Marshall-Palmer (*M-P*)*, Best, Polyakova-Shifrin* (*P-S*) *and Weibull raindrop-size distributions, and also calculated using a specific rain attenuation model for prediction methods recommended by ITU-R. Measurements of Terahertz wave taken at* 313 *GHz* (0.96 *mm*) *were compared with our calculations. Results showed that the propagation experiment was in very good agreement with a calculation from the specific attenuation model for use in prediction methods by ITU-R.*

Keywords**:** *Rain Attenuation, Raindrop-Size Distribution, Terahertz Waves, P-S Distribution, Weibull Distribution, ITU-R*

1. Introduction

Recent advances in electronic and electro-optical Terahertz devices, and improvements in system technology, have stimulated in imaging and sensing applications in the security and non-destructive testing field [1].

Rain attenuation is one of important obstacle to overcome for imaging and sensing system to detect the hazardous things using Terahertz waves above 300 GHz because of its masking action. Raindrop-size distribution has been found to play an important role in monitoring rainfall and in predicting the rain attenuation. The rain attenuation is particularly severe and greatly dependent on various models of raindrop-size distribution in a Millimeter and Terahertz wave system.

2. Raindrop-Size Distribution

Many raindrop-size distributions have been proposed. Marshall and Palmer [2] proposed the following well-known empirical expression by fitting their data and the Laws and Parsons data. Their data was taken in Ottawa, Canada in 1946 using the filter paper method. The fit of this distribution to the experimental points was not very good for drops less than D = 1 mm.

$$\begin{aligned} N(D) &= N_0 e^{-\Lambda D} \\ N_0 &= 8000\,\mathrm{m}^{-3}\,\mathrm{mm}^{-1} \\ \Lambda &= 4.1R^{-0.21}\,\mathrm{mm}^{-1} \end{aligned} \quad (1)$$

where D is the diameter in mm, and R is the precipitation rate in mm/hr.

Best [3] proposed a drop-size distribution model after analyzing a large amount of experimental data in 1950. This is written as

$$\begin{aligned} N(D) &= \frac{13.5W}{\pi a^4}\left(\frac{D}{a}\right)^{-1.75} e^{-\left(\frac{D}{a}\right)^{2.25}} \\ W &= 67R^{0.846}\,\mathrm{m}^{-3}\mathrm{mm}^3 \\ a &= 1.3R^{0.232}\,\mathrm{mm} \end{aligned} \quad (2)$$

Litovinov proposed a model [4] in 1957 and [5] in 1958 due to Polyakva and Shifrin (P-S) using the Russian data for all three types of rain. This model was also described by Krasyuk, Rozenberg and Chistyakov [6] in 1968 and by University of Tennessee [7] in 1975. It is one case of Gamma distribution proposed by Atlas and Ulbrich [8] in 1984:

$$N(D) = N_0 D^2 e^{-\Lambda D} \quad (3)$$

N_0 and Λ vary based on the rain types of thawing:

Type of Rain	N_0 m^{-3} mm^{-1}	Λ mm^{-1}
Thawing of Pellets (Hail)	64500 $R^{-0.5}$	6.95 $R^{-0.27}$
Thawing of Granular Snow (Sleet)	11750 $R^{-0.29}$	4.87 $R^{-0.2}$
Thawing of Non Granular Snow (Snow)	2820 $R^{-0.18}$	4.01 $R^{-0.19}$

Sekine and Lind [9] proposed a Weibull distribution in 1982 by using the FOA data (from the National Defence Research Institute) in Sweden:

$$N(D) = N_0 \frac{c}{b}\left(\frac{D}{b}\right)^{c-1} e^{-\left(\frac{D}{b}\right)^c}$$
$$N_0 = 1000\,\mathrm{m}^{-3}$$
$$b = 0.26R^{0.44}\,\mathrm{mm} \quad (4)$$
$$c = 0.95R^{0.14}$$

This distribution is retained for microwave applications for drizzle, widespread rain, and shower rain cases [10-22].

3. Rain Attenuation

3.1. Calculations

Rain attenuation was calculated by using three types of raindrop-size distributions and a specific attenuation model for use in prediction method recommended by ITU-R.

For calculations using by raindrop-size distributions, rain specific attenuation A in dB/km is calculated by integrating all of the drop sizes as

$$A = 4.343\int Q(D,\lambda,m)N(D)dD \quad (5)$$

where Q is the attenuation cross section that is a function of the drop diameter D, the wavelength of the radio wave λ, and the complex refractive index of the water drop m, which is a function of the frequency and the temperature, and $N(D)$ is the drop-size distribution. The attenuation cross section Q is found by applying the classical scattering theory of Mie for a plane wave radiation to an absorbing sphere particle. According to Hulst [23], the cross section Q is expanded as

$$Q(D,\lambda,m) = \frac{\lambda^2}{2\pi}\sum_{n=1}^{\infty}(2n+1)\,\mathrm{Re}\left[a_n + b_n\right] \quad (6)$$

where a_n and b_n are the Mie scattering coefficients, which are complex functions of m, D, and λ. The complex refractive index of liquid water m was taken from [24]. The "Mie scattering coefficients" a_n and b_n in Equation (6) represent a contribution to the scattered field from the multi poles induced in the sphere, such as raindrops [23].

For calculation by using the recommended prediction methods by ITU-R [24], rain specific attenuation γ_R dB/km is obtained from the rain rate R mm/hr using the power-law relationship:

$$\gamma_R = kR^{\alpha} \quad (7)$$

Values for the constants for the coefficients k and α are determined as functions of frequency, f GHz, in the range from 1 to 1000 GHz, from the equations which have been developed from curve-fitting to power-law coefficients derived from scattering calculations. It is shown in ITU-R P.838-3 [25].

3.2. Experiments and Computations

Figure 1 shows the results of 313 GHz under a rain fall rate of up to 12 mm/hr. This rain attenuation experiment was carried out by Babkin *et al.* [26] in the central part of the European part of the former Soviet Union during June and July 1969. The transmitter and receiver were spaced 1 km apart for the measurement.

For the calculations, rain drop-size distributions were used for M-P, Best, P-S and Weibull which were described in Equations (1), (2), (3) and (4) respectively, and specific attenuation model recommended by ITU-R was used for ITU-R which was described in Equation (7). M-P stands for Marshall and Palmer, P-S stands for Polyakva and Shifrin. Best, Weibull and ITU-R used the same name.

An experimental fit curve (shown by the broken line) derived from the raw data with triangular dots was described as $A = 1.53\,R^{0.638}$ [26].

The experimental data obtained from the rain attenuation was shown in **Figure 1**. It was compared with the calculations of rain attenuations. The departure of the empirical data and the calculated rain attenuations were estimated by calculating the root mean square error (rmse).

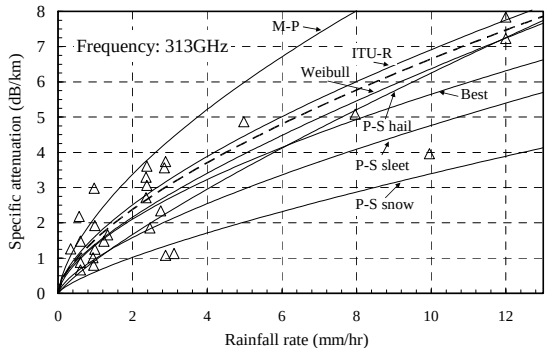

Figure 1. Comparison between calculations and measurements at 313 GHz.

Table 1. Values of rmse for various raindrop attenuations.

Calculations	TTU-T	Weibull	M-P	Best	P-S hail	P-S sleet	P-S snow
rmse	0.21	0.27	1.94	0.72	0.59	1.45	2.50

These were shown in **Table 1**. Result showed that the calculation from Weibull and ITU-R were very good agreement with the experimental data. And the best fit was the calculation from ITU-R with the smallest rmse.

4. Conclusions

Rain attenuation at 313 GHz was calculated by using four raindrop-size distributions and using ITU-R specific attenuation model. Calculated results were compared with propagation experiments under a rainfall intensity up to 12 mm/hr. Results showed that the propagation experiment was in very good agreement with the calculation from the specific attenuation model for use in prediction method by ITU-R provided the best fit for the experimental data. Finally, there is greater interest in the rain attenuation at Terahertz waves. An experiment on rain attenuation above 300 GHz at different rainfall rates with various raindrop-size distributions is desirable, especially at a higher rainfall intensity that may cause fatal damage to Terahertz applications.

REFERENCES

[1] R. M. Langdon, V. Handerek, P. Harrison, H. Eisele, M. Stringer, C. F. Rae and M. H. Dunn, "Military Applications of Terahertz Imaging," 1*st EMRS DTC Technical Conference*, Edinburgh, 2004.

[2] J. S. Marshall and W. M. K. Palmer, "The Distribution of Raindrops with Size," *Journal of Meteorology*, Vol. 5, No. 4, 1948, pp. 165-166.

[3] A. C. Best, "The Size Distribution of Raindrops," *Quarterly Journal of the Royal Meteorological Society*, Vol. 76, No. 327, 1950, pp. 16-36.

[4] I. V. Litovinov, "On the Distribution Function of Particles of Rainfall," *Izvestia AN SSSR, Geophysical Series*, No. 6, 1957, pp. 838-839.

[5] I. V. Litovinov, "Size Distribution of Raindrops from Melting Hail," *Izvestia, Geophysical Series*, No. 6, 1958, pp. 903-912.

[6] N. P. Krasyuk, V. I. Rozenberg and D. A. Chistyakov, "Attenuation and Scattering of Radar Signals by Radio with Shifrin and Marshall-Palmer Drop Size Distributions," *Radio Engineering and Electronic Physics*, Vol. 13, No. 10, 1968, pp. 1638-1640.

[7] "Investigation of Radar Rain Clutter Cancellation Using a Polarization Method," *RADC-TR*-75-126, *Final Technical Report*, University of Tennessee, Knoxville, August 1975.

[8] C. W. Ulbrich and D. Atlas, "Assessment of the Contribution of Differential Polarrization to Improve Rainfall Measurements," *Radio Science*, Vol. 19, No. 1, 1984, pp. 49-57.

[9] M. Sekine and G. Lind, "Rain Attenuation of Centimeter, Millimeter and Submillimeter Radio Waves," *Proceedings of* 12*th European Microwave Conference*, Helsinki, 1982, pp. 584-589.

[10] M. Sekine and C. D. Chen, "Rain Attenuation in Terrestrial and Satellite Communications Links," *Proceedings of the* 15*th European Microwave Conference*, Paris, 1985, pp. 985-990.

[11] C. D. Chen, Y. Okamoto and M. Sekine, "Cancellation of Radar Rain Clutter Using Circular Polarization," *Transactions on IECE of Japan* (*Section E*), Vol. E68, No. 9, 1985, pp. 620-624.

[12] M. Sekine, "The Relationship between Radar Reflectivity and Rainfall Rate," *Transactions on IECE of Japan* (*Section E*), Vol. E69, No. 5, 1986, pp. 581-582.

[13] M. Sekine, "Rain Attenuation from Various Raindrop-Size Distributions," *Transactions on IECE of Japan* (*Section E*), Vol. E69, No. 6, 1986, pp. 711-712.

[14] M. Sekine, C. D. Chen and T. Musha, "Rain Attenuation from Log-Normal and Weibull Rain-Drop Distributions," *IEEE Transactions on Antennas and Propagation*, Vol. AP-35, No. 3, 1987, pp. 358-359.

[15] M. Sekine, T. Musha and C. D. Chen, "Rain Attenuation from Weibull Raindrop-Size Distribution," *Proceedings of* 18*th European Microwave Conference*, Stockholm, 12-15 September 1988, pp. 423-428.

[16] M. Sekine and C. D. Chen, "Inversion Problem in Rain Attenuation Calculations," *Proceedings of the* 1989 *URSI International Symposium on Electromagnetic Theory*, Stockholm, 1989, pp. 23-25.

[17] H. Jiang, M. Sano and M. Sekine, "Radar Reflectivity and Rainfall Rate Relation from Weibull Rain Drop-Size Distribution," *IEICE Transactions on Communications*, Vol. E79-B, No. 6, 1996, pp. 797-800.

[18] H. Jiang, M. Sano and M. Sekine, "Weibull Raindrop-Size Distribution and its Application to Rain Attenuation," *IEE Proc-Microwaves Antennas Propagation*, Vol. 144, No. 3, 1997, pp. 197-200.

[19] S. Sayama and M. Sekine, "Influence of Raindrop-Size Distribution on the Differential Reflectivity up to Submillimeter Wavelength of 0.96 mm," *International Journal of Infrared and Millimeter Waves*, Vol. 23, No. 5, 2002, pp. 775-784.

[20] S. Ishii, "Rain Attenuation at Millimeter Wavelength of 1.33 mm," *International Journal of Infrared and Millimeter Waves*, Vol. 25, No. 10, 2004, pp. 1495-1501.

[21] T. Utsunomiya and M. Sekine, "Rain Attenuation at Millimeter and Submillimeter Wavelength," *International Journal of Infrared and Millimeter Waves*, Vol. 26, No. 6, 2005, pp. 905-920.

[22] T. Utsunomiya and M. Sekine, "Rain Attenuation at 103 GHz in Millimeter Wave Ranges," *International Journal of Infrared and Millimeter Waves*, Vol. 26, No. 11, 2005, pp. 1651-1660.

[23] H. C. Hulst, "Light Scattering by Small Particles," Wiley, New York, 1957.

[24] P. S. Ray, "Broad Complex Refractive Indices of Ice and Water," *Applied Optics*, Vol. 11, August 1972, pp. 1836-1844.

[25] Recommendation, ITU-R P. 838-3, International Telecommunication Union, "Specific Attenuation Model for Rain for Use in Prediction Methods," 2005.

[26] Y. S. Babkin, N. N. Zimin, A. O. Izyumov, I. A. Iskhakov, A. V. Sokolov, L. I. Stroganov, Y. V. Sukhonin and G. Y. Shabalin, "Measurement of Attenuation in Rain over 1 km Path at a Wavelength of 0.96 mm," *Radio Engineering and Electronic Physics*, Vol. 15, No. 12, 1970, pp. 2164-2166.

